EFFECT OF LOADING SPAN ON TENSILE MODE FRACTURE TOUGHNESS FOR THREE-POINT BEND SPECIMEN GEOMETRIES

A THESIS SUBMITTED TO
THE GRADUATE SCHOOL OF NATURAL AND APPLIED SCIENCES
OF
MIDDLE EAST TECHNICAL UNIVERSITY

BY

CEREN KARATAŞ BATAN

IN PARTIAL FULFILLMENT OF THE REQUIREMENTS
FOR
THE DEGREE OF MASTER OF SCIENCE
IN
MINING ENGINEERING

JANUARY 2020

Approval of the thesis:

EFFECT OF LOADING SPAN ON TENSILE MODE FRACTURE TOUGHNESS FOR THREE-POINT BEND SPECIMEN GEOMETRIES

submitted by **CEREN KARATAŞ BATAN** in partial fulfillment of the requirements for the degree of **Master of Science in Mining Engineering Department, Middle East Technical University** by,

Prof. Dr. Halil Kalıpçılar
Dean, Graduate School of **Natural and Applied Sciences**

Prof. Dr. Naci Emre Altun
Head of Department, **Mining Engineering**

Prof. Dr. Levend Tutluoğlu
Supervisor, **Mining Engineering, METU**

Examining Committee Members:

Prof. Dr. Celal Karpuz
Mining Engineering Department, METU

Prof. Dr. Levend Tutluoğlu
Mining Engineering, METU

Prof. Dr. Bahtiyar Ünver
Mining Engineering Department, HU

Date: 10.01.2020

I hereby declare that all information in this document has been obtained and presented in accordance with academic rules and ethical conduct. I also declare that, as required by these rules and conduct, I have fully cited and referenced all material and results that are not original to this work.

Name, Surname: Ceren Karataş Batan

Signature:

ABSTRACT

EFFECT OF LOADING SPAN ON TENSILE MODE FRACTURE TOUGHNESS FOR THREE-POINT BEND SPECIMEN GEOMETRIES

Karataş Batan, Ceren
Master of Science, Mining Engineering
Supervisor: Prof. Dr. Levend Tutluoğlu

January 2020, 143 pages

Straight notched disk bending specimen geometry has a potential to find size independent mode I fracture toughness, since the thickness of the disk loaded by three-point bending can be increased. Increasing the thickness and decreasing the loading span of bending reduces the severe bending action at the notch tip and a pure tensile mode stress state can be achieved at and ahead of the crack tip.

3D finite element program (ABAQUS) was used for computing the stress intensity factors by numerical modeling of circular disk geometry (SNDB). Modeling procedure and stress intensity computation work were verified by 3D modeling of square plate and semi-circular bend geometries under three-point bending loads and comparing the SIF results to the relevant analytical solutions of these two geometries.

Tensile mode fracture toughness tests were conducted on notched circular plate type disk and semi-circular disk andesite rock specimens. Tests were carried out under three-point bending loads. 0.5 mm wide notches providing a crack length/radius ratio of a/R=0.20 were machined to the specimens by a saw. Mode I fracture toughness tests were performed on straight notched disk bending (SNDB) disk specimens of thicknesses 50 mm and 60 mm. Loading spans were varied between 40 mm and 90 mm corresponding to span/radius ratios of S/R=0.40 to 0.90. Using the same a/R and

S/R configurations, three-point bend tests were conducted with the ISRM suggested semi-circular bending (SCB) core specimen geometry for comparison purposes. SCB tests were conducted with 50 mm thickness as suggested. Ankara Gölbaşı Andesite rock type was used in both test series.

Mode I fracture toughness values of Ankara Gölbaşı Andesite were found as K_{Ic}=1.39 $MPa\sqrt{m}$ and K_{Ic}=1.23 $MPa\sqrt{m}$ for 60 mm and 50 mm thickness SNDB test specimens, respectively. In comparison, mode I fracture toughness value was found as K_{Ic}=0.93 $MPa\sqrt{m}$ for the tests with SCB specimen.

The significant observation is K_{Ic} increases with decreasing span length for SNDB and SCB specimens. Another observation is the mode I fracture toughness value increases with increasing specimen thickness for SNDB. A tendency to the size independent fracture toughness value of 1.53 $MPa\sqrt{m}$ was observed as the result of the curve fitting process on the available test data.

Keywords: Mode I fracture toughness, Mode I stress intensity factor, Three-Point bending, SNDB, SCB, Circular disk geometry, Semi-Circular disk geometry

ÖZ

ÜÇ NOKTALI EĞME ÖRNEK GEOMETRİLERİ İÇİN ÇEKME MODU ÇATLAK TOKLUĞU ÜZERİNDE DESTEK ARALIK MESAFESİNİN ETKİSİ

Karataş Batan, Ceren
Yüksek Lisans, Maden Mühendisliği
Tez Danışmanı: Prof. Dr. Levend Tutluoğlu

Ocak 2020, 143 sayfa

Düz çentikli disk eğme örneği geometrisinin, boyuttan bağımsız mod I kırılma tokluğunu bulma potansiyeli vardır, çünkü üç noktalı eğilme ile yüklenen diskin kalınlığı arttırılabilir. Kalınlığın arttırılması ve bükülmenin yükleme aralığının azaltılması, çentik ucundaki şiddetli eğilme hareketini azaltır ve çatlak ucunda ve önünde saf çekme modu gerilme durumuna ulaşılabilir.

Dairesel disk geometrisinin (SNDB) sayısal modellenmesi ile stres yoğunluk faktörlerini hesaplamak için 3D sonlu eleman programı (ABAQUS) kullanılmıştır. Modelleme prosedürü ve stres yoğunluğu hesaplama çalışmaları, kare plakanın ve yarı dairesel eğim geometrilerinin üç nokta eğilme yükleri altında 3D modellenmesi ve SIF sonuçlarının bu iki geometrinin ilgili analitik çözümleriyle karşılaştırılmasıyla doğrulanmıştır.

Düz çentikli dairesel plaka tipi disk ve yarı dairesel disk andezit kaya örnekleri üzerinde çekme modu kırılma tokluğu testleri yapılmıştır. Testler üç noktalı eğilme yükleri altında gerçekleştirilmiştir. a/R = 0.20'lik bir çatlak uzunluğu / yarıçap oranı sağlayan 0.5 mm genişliğinde çentikler bir testere ile numunelere işlenmiştir. Mod I kırılma tokluğu testleri, 50 mm ve 60 mm kalınlıktaki düz çentikli disk eğme (SNDB) disk örneklerinde gerçekleştirilmiştir. Yükleme açıklıkları S/R = 0.40 ila 0.90 arasında açıklık / yarıçap oranlarına karşılık gelen 40 mm ila 90 mm arasında değişmiştir. Aynı a/R ve S/R konfigürasyonları kullanılarak, karşılaştırma amacıyla ISRM tarafından önerilen yarı dairesel eğme (SCB) çekirdek numune geometrisi ile üç noktalı eğme testleri yapılmıştır. SCB testleri önerildiği gibi 50 mm kalınlığında gerçekleştirilmiştir. Her iki test serisinde Ankara Gölbaşı Andezit kayaç tipi kullanılmıştır.

Ankara Gölbaşı Andezit Mod I kırılma tokluğu değerleri 60 mm ve 50 mm kalınlığında SNDB test numuneleri için sırasıyla K_{Ic}=1.39 $MPa\sqrt{m}$ and K_{Ic}=1.23 $MPa\sqrt{m}$ olarak bulunmuştur. Buna karşılık, SCB numunesi ile yapılan testlerde mod I kırılma tokluğu değeri K_{Ic}=0.93 $MPa\sqrt{m}$ olarak bulunmuştur.

SNDB ve SCB numuneleri için azalan açıklık uzunluğu ile K_{Ic} artışı önemli bir gözlemdir. Başka bir gözlem, SNDB için artan numune kalınlığı ile mod I kırılma tokluğu değerinin artmasıdır. Mevcut test verileri üzerindeki uyumlu eğri atama işleminin bir sonucu olarak, boyuttan bağımsız kırılma tokluğu değeri 1.53 $MPa\sqrt{m}$ olarak gözlenmiştir.

Anahtar Kelimeler: Mod I çatlak tokluğu, Mod I gerilme şiddeti faktörü, Üç-Noktalı eğme, Düz çentikli disk geometrisi, Yarı dairesel disk geometrisi

To My Family

ACKNOWLEDGEMENTS

First, I would like to express my sincere gratitude to my supervisor, Prof. Dr. Levend Tutluoğlu, for his invaluable guidance, encouragement, and endless support throughout my thesis.

Also, I have special thanks to the examining committee members Prof. Dr. Celal Karpuz, Prof. Dr. Bahtiyar Ünver for their participation. In addition, I want to thank Assist. Prof. Dr. Mustafa Erkayaoğlu and Dr. Selin Yoncacı for their help, distinctively. I would like to thank the METU Mining Engineering Department research assistants Doğukan Güner, Alper Kırmacı, Kutay Emre Karadeniz, and Cengiz Kaydım. I present my special thanks to Hakan Uysal for his help, extensive guidance and supports during laboratory studies.

I have to thank my mother Ayfer Karataş, my father Mehmet Karataş, my mother-in-law Güli Batan, my father-in-law Mehmet Emin Batan for their encouragement, patience, and support for my thesis. I want to thank my sister Beren Kök, my brother-in-law Şakir Oktay Kök, my lovely nephews and my grandmother Halise Karataş.

I would like to thank my sisters from another mother Özge Batır, Özge Meriç Demir, Aybüke Karakaş. I also want to thank my lovely friends Sena Sarılar, Merve Acar Temel, Sadık Temel, Erhan Ceylan, Hakan Yeter, Yiğit Altınsel and Enver Yılmaz for their supports.

Finally, I want to thank my dedicated husband Mehmet Ali Batan for not refrain to support and self-sacrifice throughout my thesis. I will never forget his support and help during my thesis work.

TABLE OF CONTENTS

CHAPTERS

APPENDICES

LIST OF TABLES

TABLES

LIST OF FIGURES

FIGURES

LIST OF ABBREVIATIONS

ABBREVIATIONS

LEFM: Linear elastic fracture mechanics

CTOD: Crack tip opening displacement

CCNBD: Cracked chevron notched Brazilian disk method

SR: Short rod method

CB: Chevron bend method

SCB: Semi-Circular bending method

SNDB: Straight notched disk bending method

ENBD: Edge notched disk bend

LVDT: Internal linear variable differential transformer

SIF: Stress intensity factor

UCS: Uniaxial compressive strength

ISRM: International Society for Rock Mechanics and Rock Engineering

FPZ: Fracture process zone

LIST OF SYMBOLS

SYMBOLS

a: Crack length

t: Specimen thickness

R: Specimen radius

D: Specimen diameter

S: Half-Span length

σ: Normal stress

P: Applied load

P_{cr}: Applied load at fracture

T_0: Tensile strength

Y_I: Dimensionless stress intensity factor

K: Stress intensity factor

K_I: Mode I stress intensity factor

K_{II}: Mode II stress intensity factor

K_{III}: Mode III stress intensity factor

K_c: Fracture toughness

K_{Ic}: Mode I fracture toughness

$\mathcal{G}$: Strain energy release rate

$\mathcal{G}_c$: Critical strain energy release rate

J: J integral

υ: Poisson's ratio

E: Young's modulus

r: Distance from crack tip

τ: Shear stress

θ: angle from x-direction

u: Displacement component near crack tip

μ: Shear modulus

ΔP: Differential pressure transducer

$r_{y/a}$: Extent of a possible plastic or yield zone around the crack tip

CHAPTER 1

INTRODUCTION

1.1. General Remarks

Structures and relevant materials have little and/or large flaws and defects as cracks, micro voids, etc., since they are not perfectly continuous and homogenous. Knowing their size and shape and whether they can propagate under a particular loading configuration is essential because these defects affect strength of the structural parts. The traditional design of structural parts is based on the ultimate strength or yield strength. However, small cracks and defects may propagate violently under a particular combination of crack length and loading configuration before a yield point is reached. The fracture mechanics assesses if these small defects will propagate in a stable or unstable manner. It is one of the branches in mechanics which is about the progressing of cracks under applied loads in materials. Fracture mechanics is an important tool to determine the driving force on a crack and to characterize the strength to fracture.

The strength of any structure or structural part decreases due to the existence of the cracks. The predictions about the rate of the crack growing and rate of the decreasing strength of the structure are aims of the fracture mechanics.

Fracture mechanics comprise different various fields such as applied mechanics, engineering, etc. Each field contains a process in itself. For instance, analyses of the load and crack tip stress is an issue of the applied mechanics. Stresses tend to infinity at the crack tip leading to a mathematical singularity in stress expressions. Depending on the loading configuration and the crack length, the size of the singularity-dominated zone at the crack tip changes. Output of stress analysis yields the stress intensity factor which controls the size of the crack tip singularity-dominated zone. Fracture toughness and critical energy release rate are essential material parameters controlling a particular material’s crack resistance under a specific loading condition. Cracks require more potential energy to propagate and form new surfaces. By knowing the fracture toughness or critical energy release rate, surface energy to form new surfaces can be estimated.

Science and engineering disciplines make use of fracture toughness. Measuring the toughness of cancellous bone is one of the examples of area related to the science of the materials and medical (Cook, 2005). In Civil Engineering, an example use is in characterizing the resistance to cracking of asphalt mixtures (Li et al., 2004). Aerospace Engineering uses to investigate crashes such as failing of the Aloha Airlines Boeing 737 due to the several crucial cracks (Banks, 2003).

In Geological and Mining Engineering, analyzing pre-failure rock mass behavior (Szwedzicki, 2003), rock cutting and breaking, hydro fracturing can be counted among the applications employing the fracture toughness and fracture mechanics. One of the applications of the rock fracture mechanics is planning structures of rock to prevent or minimize the existence of the fractures or growing of cracks.

1.2. Brief History About Fracture Mechanics

Since ancient times throughout humanity application fields of metals has been increases with the development skill of metalworking. Therefore, unforeseeable failures occurred sometimes due to the fact that the behavior of the structures which were built with these materials could not be predicted correctly. In the nineteenth century, lots of accidents and casualties occurred because of the increasing use of metals. Two hundred people died per year in Great Britain between the years 1860 and 1870 because of railway accidents (Broek, 2012). Fracturing of wheels, axles or rails had led to these accidents.

The shortcoming of structures which have pre-existing flaws could commence cracks and brittle fractures. These cracks, brittle fractures and insufficient fracture mechanics-based design of structures caused many disasters in the past.

During World War II, 2700 Liberty Ships were made to be used in the war. Ten of these ships sunk by splitting into two in Alaska. Serious fracturing was observed for around 400 ships. 90 of them were considered critical. (Anderson, 1991). Figure 1.1, shows one of the liberty ships which were broken into two pieces. Researches have shown that there are three main factors that caused these fracturing events. The first one is the welds containing cracks which were produced by low-labor force skills. Another important factor is that several of the cracks started on the sharp corners due to high local stress condensation. The last factor is that Liberty ships were built by using the steel which had safe enough yield strength but poor fracture toughness.

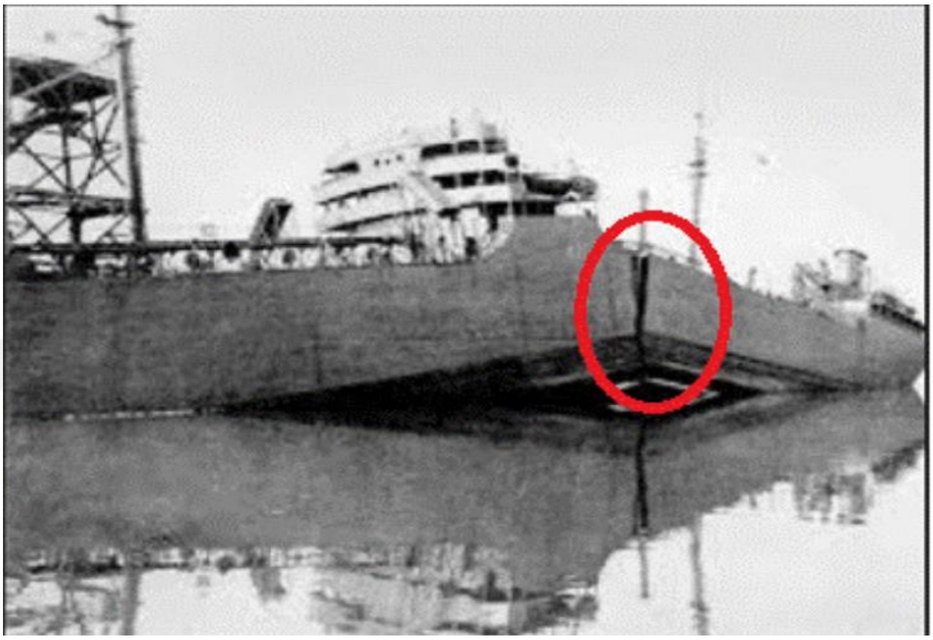

Figure 1.1.“Schenectady”- the ship that broke into two (Retrieved from metallurgyandmaterials.wordpress.com)

Analyzing and identifying the causes of fracturing events, the remaining Liberty ships were strengthened with some reinforcements in the hatch corners. Furthermore, extra steel plates which had high toughness were clinched to the decks at some strategic locations of the Liberty ships.

In 1950’s, Comet airplanes were popular in commercial aviation. Unfortunately, a Comet burst in minutes in the air after a few years of service. As a result of the explosion, it was broken into the number of pieces and all passengers and crew of the cabin died. Researchers found that square-shaped fuselage windows' corners caused excess stress accumulation (Figure 1.2). Corners have similar singular stress distributions like crack fronts due to the sharp curvatures. In addition, the material in which aircraft were made had defects and could not endure long flights. Over the years, Comet could not withstand the internal cabin pressure, so it exploded eventually.

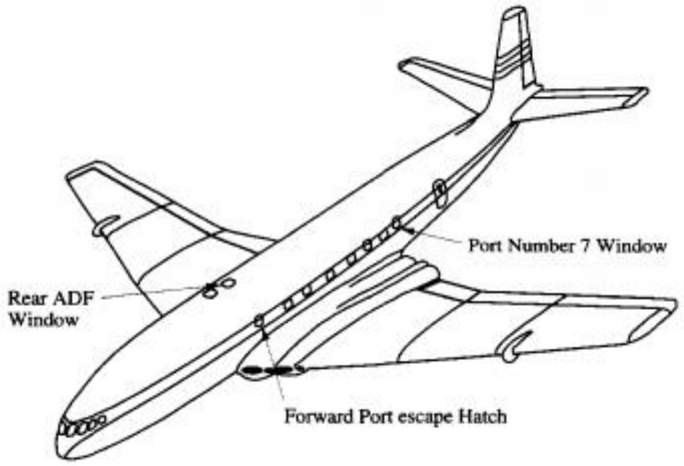

Figure 1.2. Main failure origin on Comets (Withey, 1997)

The Aloha Airlines Boeing 737 airplane failed because of the fatal cracks (Figure 1.3). In 1988, Boeing 737 of the Aloha Airlines Flight 243 was making the flight from Hilo Island, Hawaii to Honolulu. The upper part of the plane was scratched out from the center part of the cabin because of the pressure of the cabin and this led to the belly-landing. 59 passengers were injured and one person in the crew died in this disaster (Jones, R., Molent, L., & Pitt, S., 1999).

Figure 1.3. Aloha Airlines flight 243 fuselage failure (Retrieved from aerotime.aero)

The investigations which were made after the disaster showed there were major cracks on the support beams under the floor and the panels of the cabin area. Multiple interacting cracks had caused failing of the Aloha Airlines Boeing 737 airplane.

Fracture mechanics is a crucial tool for mining engineers in order to handle problems which are rock slope stability analysis, design of the underground opening, dust control of the coal mine, fragmentation of the rock by blasting and cutting. (Singh, R. N., & Sun, G., 1990). The rock materials and some combinations of the rock materials have generally flaws and fractures. Rock mass surrounding some structures of the mining which are shafts, transportation galleries, production chambers, etc. possess such flaws and fractures. Rock masses have discontinuities. The rock strength and redistributions of the stress when the rocks are fractured are controlled by these discontinuities. This is one of the vital problem for rock mechanics. Considering all this, these problems can be handled by applying properly fracture mechanics with rock mechanics.

1.3. Statement of the Problem

ISRM suggests some methods to assign rock fracture toughness for mode I (K_{Ic}). The method of the short rod (Ouchterlony, 1988), chevron bend (Ouchterlony, 1988), cracked chevron notched Brazilian disc (Shetty et al., 1985) and semi-circular bending (Chong and Kuruppu, 1984) are some of them. Unfortunately, performing fracture tests with some of these methods is very difficult due to the difficulties in sample preparation and testing procedures.

Mode I fracture toughness of the rocks can be measured in a simpler way by using core specimens, since these are available from borehole investigations. Two simple core specimen geometries and testing methods are adapted here.

Pure tensile mode fracture toughness tests will be conducted with straight notched disk bending (SNDB) specimen and semi-circular disk bend (SCB) specimen to assign K_{Ic} of the rocks. Loading will be generated by three-point bending of the disks. Main specimen geometry used in this work is circular plate type core disk named as SNDB. Results of mode I fracture toughness tests with SNDB geometry will be compared to the results of the tests with ISRM suggested semi-circular bending (SCB) specimen geometry.

In the related previous work, the loading span length was kept limited to measure mode I fracture toughness with three-point bend specimen geometries. Relatively narrower spans are planned to be used in this work in addition to a wide range of various spans used before. Applicability of core disk test specimens and their performance on assigning K_{Ic} of rocks are challenging areas in rock fracture mechanics because specimen size is restricted with specimen thickness and core diameter. The effect of the varying loading span and the effect of the changing specimen thickness with core-based specimens on the mode I fracture toughness under a three-point bend loading condition should be investigated.

1.4. Objective of the Study

The main objective of this thesis is to assign mode I fracture toughness of an andesite rock specimen geometry under three point bending load. Two specimen geometries and methods are adopted for this purpose. These are straight notched disk bending (SNDB) test method and semi-circular bending (SCB) test method on circular disk shaped rock and semi-circular disk shaped rock specimens.

The aim of the study covers the investigation of the effect of varying loading span on K_{Ic} with two core specimens and this investigation is planned to be carried out here with the SNDB and SCB geometries under three-point bending. Another investigation is to observe the effect of changing thickness on K_{Ic} for the SNDB geometry. The purpose is to try to reach a size independent tensile mode fracture toughness, suffering minimum from the plastic zone ahead of the crack tip.

1.5. Methodology of the Study

Numerical and experimental work for three-point bending test specimens compose the methodology of this study. The numerical computation of SIF in the models was done by ABAQUS 2019, which is a licensed software package of the METU computer center in this study. Circular disk geometry (SNDB) and semi-circular disk geometry (SCB) were modeled in three dimensional (3D) with ABAQUS. The stress intensity factors of SNDB model geometry having different crack length were compared results to the previous work of Keleş&Tutluoğlu (2011) to estimate optimum crack length. 10 mm crack length was selected to be inserted to all SNDB model geometries.

Numerical computation was done in two-stage as before and after the experimental study. The first stage of the numerical computation was done to define loading configuration at the crack tip. To reach this aim, the unit load was applied to the model geometry. The loading condition was formed by three different points. The second stage was done later study of the experimental. In this stage, fracture loads acquired from experimental work were applied to the numerical models created before.

The mode I fracture toughness was computed for grey Ankara andesite rock specimens. Preparation of the andesite specimens and testing work compose the experimental study. In testing process, rock testing machine (MTS) was used. In experimental study, 81 fracture toughness tests were conducted. The number of SNDB tests were 54. The remaining tests were performed with SCB specimen geometries. Experiments were carried out with displacement control by the software which is named as MTS™ Series 793 Control Software.

Mode I fracture toughness of the andesite rock computed by straight notched disc bending (SNDB) tests were compared with results of the K_{Ic} from semi-circular bending (SCB) tests. The analysis of the size effect on K_{Ic} was done with SNDB specimen geometry. The effect of the varying span length on K_{Ic} was investigated with two core-based specimen geometries. Finally, stress analysis was performed along the paths ahead of the crack tip for SNDB and SCB test specimens compared to the extent of the possible plastic zone under three-point bend loading condition.

1.6. Sign Convention

In mechanic studies, if the direction of the stresses, displacements, and forces is compressive, the sign is taken negatively. On the other hand, if the direction of the stresses, displacements, and forces is tensile, the sign is taken positively. However, the rules are vice versa in the study of rock mechanics. It means that the sign of compressive of the stresses, displacements, and forces are taken positively while the sign of tensile of the stresses, displacements, and forces are taken negatively. The sign convention of the ABAQUS is the same with general rules used in the study of the mechanics. As we know, general Cartesian coordinate system is shown by x, y and z. ABAQUS points out them as 1, 2 and 3. Moreover, the sign of the stress intensity factor in mode I (K_I) is taken positively when tending of the crack is in opening direction otherwise it is taken negatively (Figure 1.4).

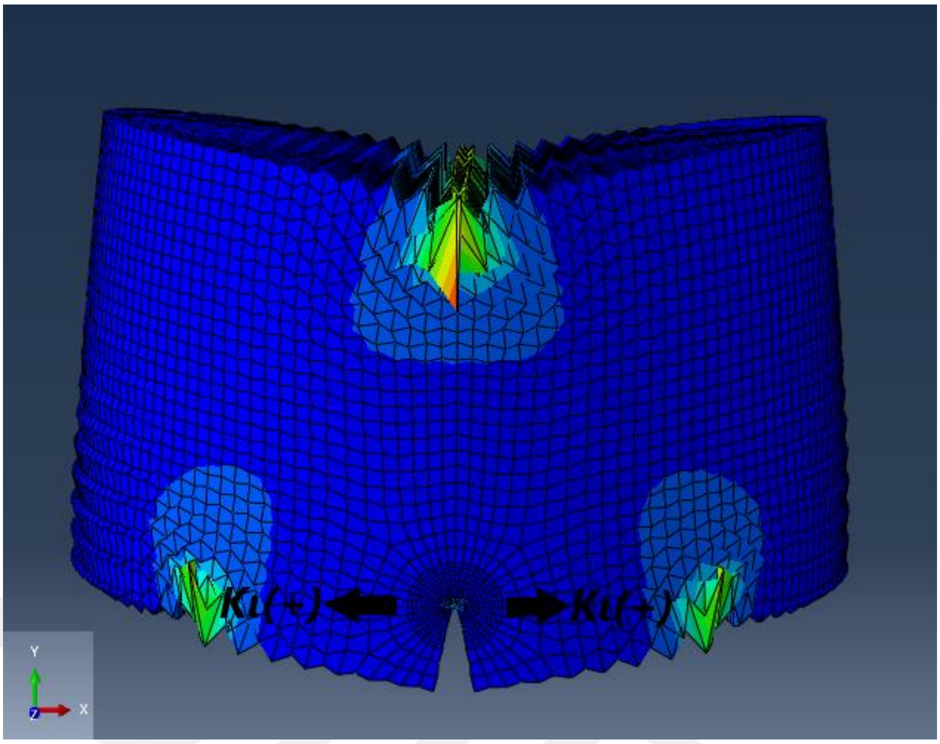

Figure 1.4. Sign of the stress intensity factor (K_I) for model geometry of the SNDB and crack opening direction

1.7. Outline of the Thesis

In Chapter 1, history of the fracture mechanics is given shortly. Also, some general remarks related to fracture mechanics are given. Furthermore, statement of the problem, objective and methodology of the study and sign convention of finite element package program are given in this chapter.

In Chapter 2, information about the fundamentals of the fracture mechanics for brittle materials are given. Meaning and scope of the linear elastic fracture mechanics are discussed. It includes fracture modes, stresses and displacements around the crack tip for mode I. This chapter contains definition of the stress intensity factor, J-integral and fracture toughness. In addition to this, fracture mechanics application areas are given. Hydraulic fracturing, rock blasting and drilling, rock excavation, crushing and grinding processes in mineral processing are discussed in this section.

In Chapter 3, ISRM suggested methods and beam testing method for mode I fracture testing are given. Specimen geometries for these tests and analytical expressions for calculation of stress intensity factor of them are given.

In Chapter 4, information about software program of ABAQUS is given. Verification examples with three-point bending plate and SCB geometry are given. Numerical modelling of the SNDB specimen are presented. Results from numerical study performed on mode I SIF are given.

In Chapter 5, experimental works and results to determine mechanical properties of andesite are given. Testing machine and using other equipment are given. Procedures of testes are discussed.

In Chapter 6, fracture tests performed with SNDB and SCB specimen are presented. Results of the mode I fracture toughness obtained from fracture tests are given.

In Chapter 7, the analyses of the effect of the size and effect of the loading span on K_{Ic} given. K_{Ic} obtained from SNDB tests and SCB tests are compared. The stress analyzes of SNDB and SCB geometries are presented.

In Chapter 8, conclusions of thesis are given. Some recommendations are given for future work.

CHAPTER 2

FRACTURE MECHANICS

2.1. Fundamentals of the Fracture Mechanics for Brittle Materials

Griffith is the one of the most important people in the fields of fracture mechanics. He was the pioneer of the studies of fracture in glass around 1920s. He used Inglis' work which is about calculating the stress concentrations around elliptical holes to estimate fracture strengths (Roylance, 2001). Inglis (1913) previously studied on the stress concentration around elliptical holes. Inglis (1913) tried to develop one approach to foresee the strength of the fracture. Unfortunately, his solutions had some difficulties by mathematically because the stresses go infinity at the tip of the crack in the boundary of the sharp crack (Roylance, 2001). By Griffith's Theory, stress values reached the theoretical maximum in which the overall stress average was lower. Furthermore, Griffith studied about the energy balance approach. In this work, he obtained a new relation between surface energy, crack length and applied stress. The applied stress is inversely proportional to $\sqrt{a}$ and proportional to $\sqrt{2\gamma E}$. γ refers the energy required to constitute new area of the material surface. Energies are consumed to form new surfaces due to surfaces contain more energy than a body. Whether a stretched cracked body remains stationary or unstable depends on whether the cracked body contains sufficient energy to form an additional surface in still maintaining stability (Wang, 1996). If the crack grows, the free surfaces are unloaded and finally, the strain energy is released. Even though Griffith has become one of the most famous developments in materials science, his theory was limited to the only elastic and brittle materials.

In 1957, Griffith Theory of brittle fracture was modified by Irwin (Yarema, 1996). Irwin introduced the concept of effective surface energy and used this concept to reformulate the Griffith Theory with regard to singularity at the crack front (Yarema, 1996). He defined the term of the stress intensity factor which is denoted as K. The stress intensity factor is proportional to $\sigma \times \sqrt{a}$. It is called a critical stress intensity factor which is demonstrated by K_c when it attains to critical value. Critical stress intensity factor is used as a replacement term for fracture toughness. Irwin (1957) described strain energy release rate with a different name as crack driving force which is denoted by $\mathcal{G}$. The crack driving force is named as critical strain energy release rate which is shown as $\mathcal{G}_c$ when it reaches critical limit.

By Wells (1955), fracture mechanics analyses were used to show that fuselage in several Comet jet aircraft the result of fatal cracks reaching a critical size. During 1960s, several works were done by different researchers such as Dugdale (1960) and Barenblatt (1962). They improved models in detail based on a narrow tape of yielded material at the crack tip while the plastic zone correction of the Irwin was a simpler enlargement of the LEFM (Anderson, 2017). Wells (1961) studied about opening displacement at the crack tip.

A new toughness measure which is plastic deformation as nonlinear elastic behavior was developed by the James Robert Rice (1968). According to researches of the James Robert Rice (1968), the energy release rate may be expressed as a path-independent line integral which is named as J integral (Anderson, 2017). Rice (1968) led the research of fracture mechanics in the new age by thanks to this approach.

2.2. Linear Elastic Fracture Mechanics

The stress field of at and ahead of the crack and energy criterion are main criteria on which Linear Elastic Fracture Mechanics (LEFM) is based. The relation between the energy which is required to form new surface and release of the strain energy is defined by the Energy Balance Criterion. The approximation of the stress intensity factor which is based on displacement fields and near tip stress was made by Irwin (1957). Energy balance criterion and stress field approaches can be regarded equivalent for linear elastic materials (Sun & Jin, 2012).

LEFM considered materials as elastic, homogenous and isotropic (Wang & Duong, 2015) Properties of these materials are independent of time and direction.

2.2.1. Fracture Modes

Normal stress analysis is insufficient to measure the strength of the fractured geometry due to stress concentrations formed by cracks. The stress intensity factor helps to make this calculation. It varies according to the loading modes.

There are three failure modes in fracture mechanics. These are called as mode I, mode II and mode III (Figure 2.1). The classifications are mainly based on applying a force to permit a crack to propagate.

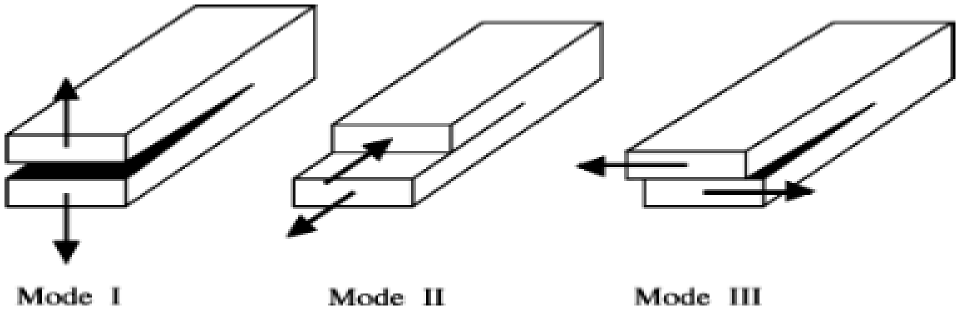

Figure 2.1. Fracture modes (Chang, Lee & Jeon, 2002)

Mode I is named as the tensile opening mode. In this mode, the direction of the crack plane shows crack development. The crack has no shear force so, there is no obvious data for shear displacement (Backers, 2004). In-plane sliding or shear mode is defined as mode II. Crack driving direction is normal to the front of the crack for mode II. Crack plane extension parallel to the direction of the shear traction. The third mode is named as out of plane mode. Shear displacement is acting parallel to the front in the crack plane (Backers, 2004). Furthermore, these crack deformations may take place in any combinations. Mixed-mode refers to a combination of the different fracture modes.

2.2.2. The Stresses and Displacements near the Crack Tip for Mode I

For a linear elastic homogeneous isotropic part, the analytical solutions for the opening-mode stresses and displacements at a crack tip were developed by Westergaard (1934) with semi-inverse method. The relevant stress components for stress field of the crack tip are shown in Figure 2.2. The distance between the polar element and the crack tip is shown by distance *r* which is measured from the tip. Stress field near the crack tip is proportional to polar angle θ and $1/\sqrt{r}$. Stresses have a singularity $1/\sqrt{r}$ at the crack tip. The coefficient of stress expressions is defined as stress intensity factor which is shown by *K*. Three different modes as K_I, K_{II}, K_{III} refer to the modes of the fracture which are defined above.

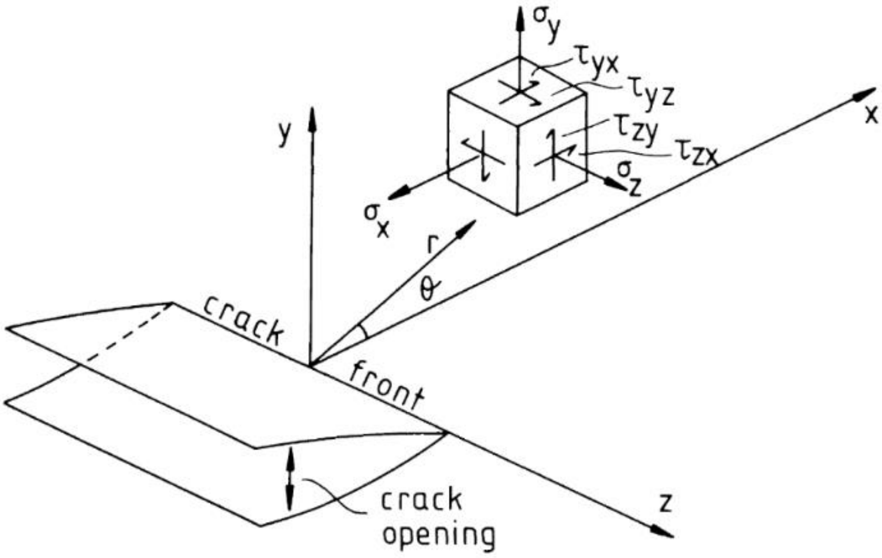

Figure 2.2. Stress components of the linear elastic crack tip stress field (Atkinson, 2015)

The equations to calculate the stresses near the crack tip for mode I are given by

$$\sigma_x = \frac{K_I}{\sqrt{2\pi r}} \cos\left(\frac{\theta}{2}\right)\left[1 + sin\left(\frac{\theta}{2}\right) sin\left(\frac{3\theta}{2}\right)\right] \qquad (2.1)$$

$$\sigma_y = \frac{K_I}{\sqrt{2\pi r}} \cos\left(\frac{\theta}{2}\right)\left[1 - sin\left(\frac{\theta}{2}\right) sin\left(\frac{3\theta}{2}\right)\right] \qquad (2.2)$$

$$\tau_{xy} = \frac{K_I}{\sqrt{2\pi r}} \cos\left(\frac{\theta}{2}\right) sin\left(\frac{\theta}{2}\right) cos\left(\frac{3\theta}{2}\right) \qquad (2.3)$$

$$\sigma_z = \begin{cases} 0 \quad \text{(plane stress)} \\ \upsilon(\sigma_x + \sigma_y)\text{(plane strain)} \end{cases} \qquad (2.4)$$

$$\tau_{yz} = 0 \qquad (2.5)$$

$$\tau_{xz} = 0 \qquad (2.6)$$

where;

K_I = stress intensity factor for mode I

σ = normal stress

τ = shear stress

r = distance from crack tip

θ = angle from x-direction

The equations to calculate the displacements near the crack tip for mode I are given by

$$u_x = \frac{K_I}{2\mu}\sqrt{\frac{r}{2\pi}}\, cos\left(\frac{\theta}{2}\right)\left[\kappa - 1 + 2sin^2\left(\frac{\theta}{2}\right)\right] \qquad (2.7)$$

$$u_y = \frac{K_I}{2\mu}\sqrt{\frac{r}{2\pi}}\, sin\left(\frac{\theta}{2}\right)\left[\kappa + 1 - 2cos^2\left(\frac{\theta}{2}\right)\right] \qquad (2.8)$$

$$u_z = 0 \qquad (2.9)$$

$$\kappa = \begin{cases} \frac{3-\upsilon}{1+\upsilon} \quad (plane\ stress) \\ 3 - 4\upsilon \quad (plane\ strain) \end{cases} \qquad (2.10)$$

where;

K_I = stress intensity factor for mode I

u = displacement component near crack tip

μ = shear modulus

r = distance from crack tip

θ = angle from x-direction

2.3. Stress Intensity Factor

Stress intensity factor is used in fracture mechanics to foresee the magnitude of local stresses near the crack tip. It defines the amplitude of the singularity at the crack tip (Wang, 1996). Stress intensity factor is expressed by K.

Stress intensity factor is a stress-based measure and it is calculated from the expression below:

$$K = \sigma\sqrt{\pi a} \times f\left(\frac{a}{w}\right) \tag{2.11}$$

where;

σ = applied stress

a = crack length

$f\left(\frac{a}{w}\right)$ = correction factor that depends on specimen and crack geometry

w = specimen width

Stress intensity factor may be varied in terms of loading configuration, crack size, crack shape, and specimen geometries. Some types of stress intensity factor formulas are given in Figure 2.3.

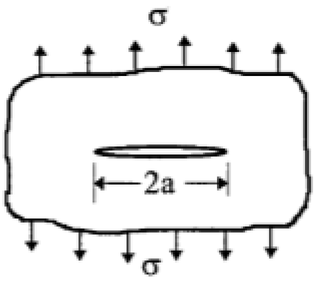 $K_I = \sigma\sqrt{\pi a}$ The crack in an infinite body (Wang, 1996)	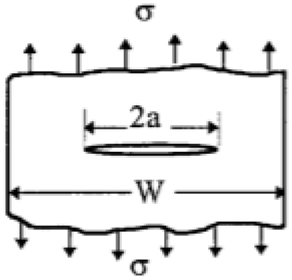 $K_I = \sigma\sqrt{\pi a}\sqrt{sec\frac{\pi a}{W}}$ Centre crack in a strip of finite width (Wang, 1996)
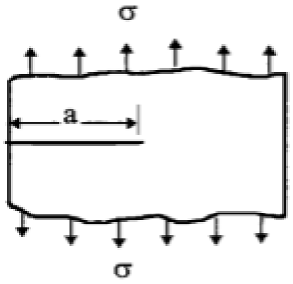 $K_I = 1.12\ \sigma\sqrt{\pi a}$ Edge crack in semi-infinite body (Wang, 1996)	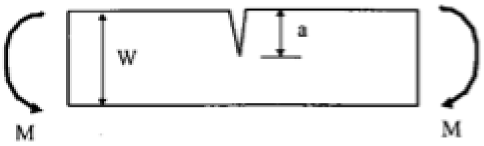 $K_I = \sigma\sqrt{\pi a} \times f\left(\frac{a}{w}\right)$ a/W $f\left(\frac{a}{w}\right)$ 0.1 1.044 0.2 1.055 0.3 1.125 0.4 1.257 0.5 1.500 0.6 1.915 Edge crack in a beam type specimen under bending

Figure 2.3. Stress intensity factor for different crack type and specimen geometries (Wang, 1996)

To illustrate the concept of stress intensity factor, mode I stress intensity factors are computed for a stress σ =100 Pa and a=0.10 m. r/a is changed and crack tip stress fields are plotted for varying r/a in Figure 2.4.

To show the strong beam effect a/W=0.5 case is chosen for the SIF of the beam in Figure 2.4.

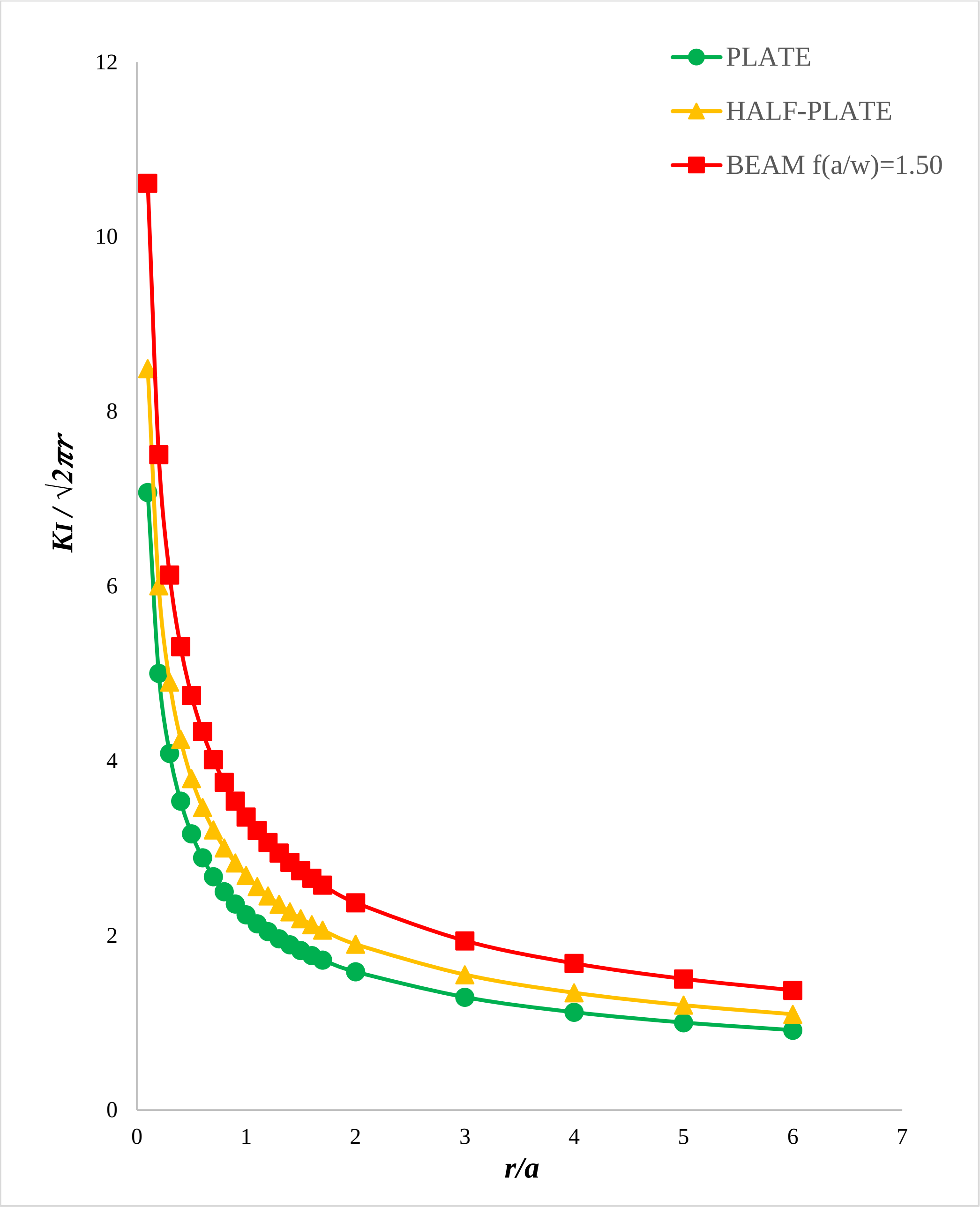

Figure 2.4. Crack tip stress fields versus *r/a*

Figure 2.4 explains the meaning of changing amplitude of crack tip stress field singularity. The mode I stress intensity factor of the beam type specimens is higher than the plate type specimen. The bending action causes a higher K_I than the tensile loading of infinite plate.

2.3.1. The J- Integral

J- integral is more general technique which is used to calculate stress intensity factor. It means contour integral which is path independent around the crack tip (Figure 2.5). ABAQUS software package uses the J- integral method to analyze the near the crack tip. It was defined by the Rice (1968) firstly and used like a fracture parameter. The contour J- integral was obtained from the potential energy resulting of crack extension.

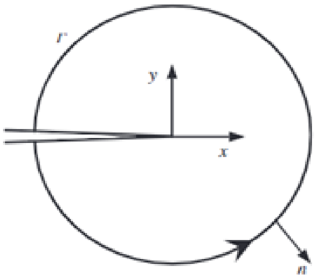

Figure 2.5. The path independent contour around the crack tip (Chang, 2013)

The J-integral theory is valid for both materials of the linear elastic and nonlinear elastic. The concept of the J-integral has been used on elastic-plastic materials complying with deformation plasticity. The formula J-integral is given by

$$J = \int \left[W dy - T_i \frac{\partial}{\partial x} ds \right] = \int \left[W \delta_{1j} - \sigma_{ij} \frac{\partial z_i}{\partial x} \right] n_j d\Gamma \qquad (2.12)$$

where;

σ_{ij} = Cauchy stress tensor

$n =$ outward vector components to an arbitrary contour near the crack tip

$z_i =$ ith displacement component

Γ = an arbitrary contour beginning at the lower crack surface and ending on the upper crack surface

W = strain energy

2.4. Fracture Toughness

Fracture toughness is an important material parameter referring level of critical condition needed for the starting of fracture (Smith, Ayatollahi& Pavier, 2006). It is valid for classification of the rocks, design of the rock structures and analysis of the rock related problems. Fracture toughness is denoted as K_c.

Fracture toughness is termed as critical value of stress intensity factor. It shows the resistance of the materials to fracture and to propagate of pre-existing cracks. Fracture toughness is directly related to mechanical properties and geometry of the materials.

2.5. Fracture Mechanics Applications

Rock mass commonly involves discontinuities and fractures. Prediction of the behavior of the cracks and flaws is useful for applications relevant to rocks. The fracture mechanics approach can provide mechanisms in planning rock breaking processes and prediction of rock mass behavior with discontinuities. One objective is to avoid the material from fracturing in disciplines relevant to rock fracture mechanics. However, hydraulic fracturing, rock blasting and drilling, rock excavation, crushing and grinding processes in mineral processing are some of the applications of the rock fracture mechanics which aims crack production.

2.5.1. Hydraulic Fracturing

In rock fracture mechanics, fluid injection operations in sealed-off borehole intervals requires the term of the hydraulic fracturing to induce and develop tensile fractures (Rummel, 1987). Furthermore, deep gas or impulse of the water well have been required to approach hydraulic fracture mechanics. The process of hydraulic fracturing is based on Kirsch's solution for the stress distribution near a circular hole in an elastic, homogeneous and isotropic material depending on the external compression. Studies of the rock fracture mechanics are used to get rock fracturing resistance. The new crack surfaces require energy which is calculated and adequate pressure. The adequate pressure is obtained by pumps. Lastly, required liquid is estimated. These processes are applied to provide successful fracturing. They are related to hydraulic fracturing.

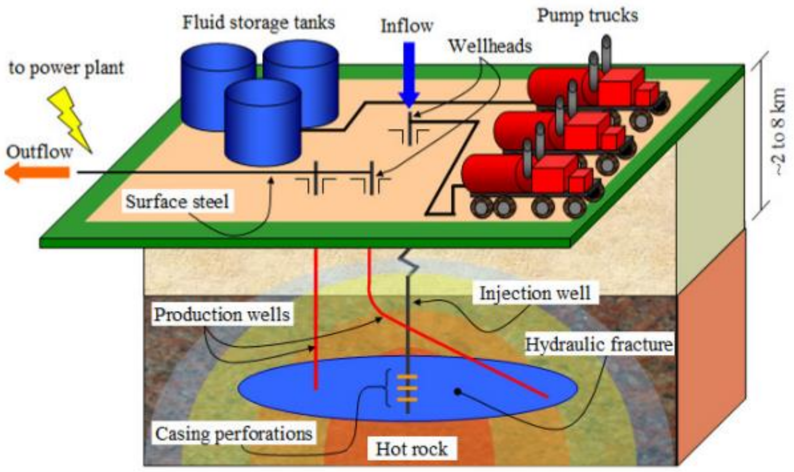

Figure 2.6. Hydraulic fracturing (Frash, 2014)

2.5.2. Rock Blasting and Drilling

The damage of mechanics and developing stress waves to the field of drilling and blasting is one of the main focus of rock fracture mechanics. Fragmentation mechanism is an important process to break rock efficiently by explosive loading and for controlling to reduce the limit the damage inflicted to the around rock mass (Rossmanith, 1997). Furthermore, there is a relationship between rock blasting and energy release rate on fracture propagation. This term is defined by strain energy-based fragmentation of rock. The rocks which is in deep from the surface tend to release stored energy. The strains occur in rock due to this stress. The term damage refers unwanted destruction in rocks and surfaces in mining engineering. In mining, this damage can be different forms like damage of the stope and pillar because of rock bursts or excessive cracking relevant to mining advance.

The mechanical breakage to excavate the rocks can be applied by diggers, drag bits, hydraulic top hammer and cutters with loads which can be compressive or shear. The force with indenter is applied perpendicularly to rock and force with drag bit is applied parallel to rock. The tensile fractures (mode I) emerge from both of applied forces (Figure 2.7).

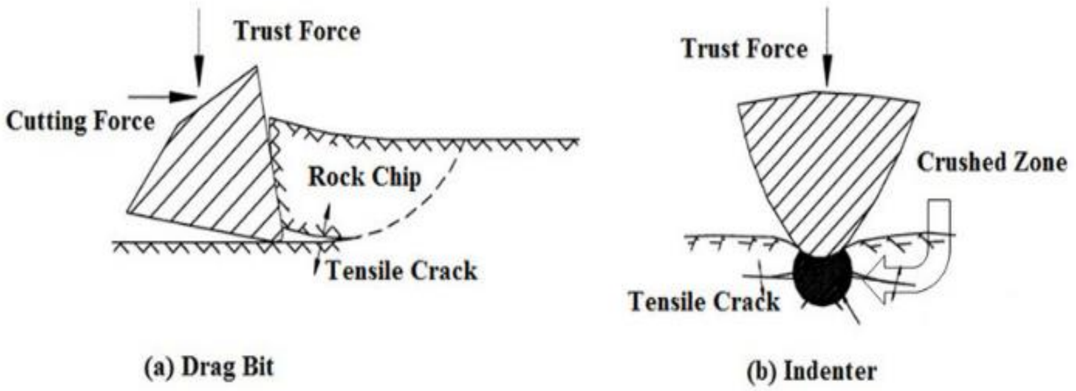

(a) Drag Bit

(b) Indenter

Figure 2.7. Rock cutting with drag bit and indenter (Ghamgosar & Erarslan, 2015)

Furthermore, Bernardino Chiaia studied relation between the penetration rate, cutting strength and specific energy (Chiaia, 2001). In this study, the relation was estabilished between tangential force and normal force (Figure 2.8).

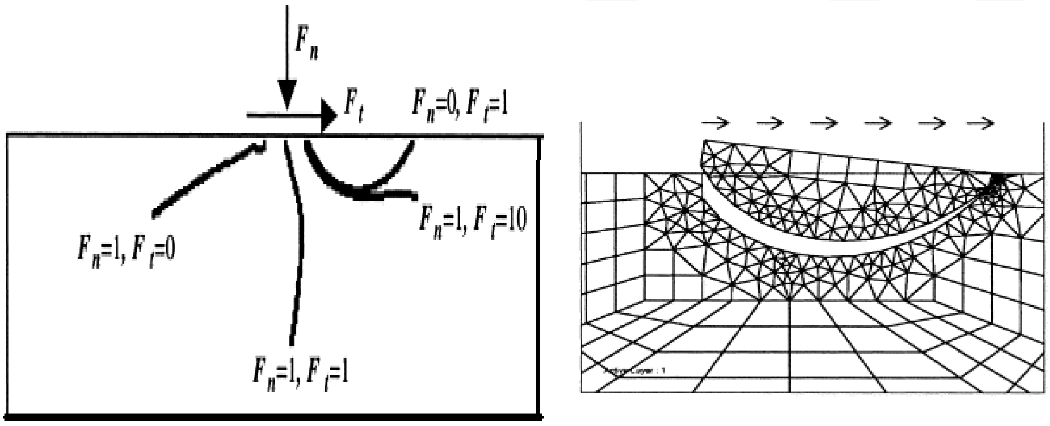

Figure 2.8. Finite element simulations of brittle cracking under a sliding indenter (Chiaia,2001)

The first figure shows the direction of these forces. The another relation is between the normal force tangential force and fracture toughness. Chip formation is preferred rather than crushing under indenter. The right figure shows the brittle cracking under a sliding indenter and chip formation.

$$\left.\begin{aligned} F_N &= kw \\ F_t &= S\gamma w^2 \end{aligned}\right\} \quad F_t = S\gamma(F_N^2/k^2) \tag{2.13}$$

$$F_t = K_{Ic}\gamma w^{3/2} \Big\} \quad F_t = K_{Ic}\gamma(F_N/k)^{3/2} \tag{2.14}$$

where;

k= stiffness(N/m)

γ = non - dimensional factor

S= specific energy(J/m^3) or cutting strength(N/m^2)

w= linear penetration (m)

2.5.3. Rock Slope Stability

The discontinuity surfaces or cracks cause slope failures. Generally, a movement starts from the crack tips. This crack tips contain stress concentration. It can lead to failure which cannot be determined by methods of the limit equilibrium. Kinematics and discontinuities tendency of the rock bodies are considered by this method. Failures of the rock slope are frequently checked by a combination of discontinuities complexly which facilitate the kinematic release (Brideau et al., 2009). The pre-existing rock mass cracks, discontinuities, fractures, and damages employ a vital role in slope stability. The knowing the fracture mechanic process provides an understanding of the failure mode of the potential and suitable methods of both analysis and corrective treatment.

2.5.4. Crushing and Grinding Processes in Mineral Processing

The fracture mechanics related to comminution behavior in mineral processing. The main purpose of the comminution is to break rocks to the required sizes. It leads the relation between the surface area and applied energy. Initiatives to reinforce rock mechanics and comminution approaches and relate them to fracturing have evolved over the last decade (Bearman et al., 1997). The studies of the Bearman (1997) contain relationship between strength parameters of the rocks and consumption of power and size of the product in crushing. According to these studies, there is important relation strength parameter with tensile and performance of the crusher.

The optimum design of jaw crusher was considered by using the fundamentals of the rock fracture mechanics (Donovan, 2003). There is a high correlation between the value of the fracture toughness of rocks particle and comminution energy according to studies of Donavan. Furthermore, fine-grained rocks have higher fracture toughness value than coarse-grained rocks according to studies of Wills and Napier-Munn (2006).

CHAPTER 3

MODE I FRACTURE TOUGHNESS TESTING METHODS

There are different methods to compute the values of the fracture toughness under mode I (tensile mode) loading condition. Loading can be applied to propagate the crack in the rock specimens by compressive loading, three or four-point bending, direct tensile loading. To assess the fracture toughness in tensile mode (mode I), four methods are suggested by International Society for Rock Mechanics and Rock Engineering (ISRM). These are cracked chevron notched Brazilian disk method (CCNBD), short rod (SR), chevron bend (CB) and semi-circular bending method (SCB). ISRM suggested methods are described first. Finally, straight notched disk bending method (SNDB) chosen as the major geometry for this study is described.

3.1. Cracked Chevron Notched Brazilian Disk Method

The cracked chevron notched Brazilian disk method was applied firstly by Shetty et al (1985). CCNBD method is one of the proposed methods by ISRM among fracture toughness test methods for rock specimens (Fowell et al., 1995). The chevron notch is prepared with two cuts from the sides of the disc throughout axis of the disc-rotating on the identical diametrical cutting plane (Chang et al., 2002). CCNBD specimens are loaded under compression along the diametric plane in this method (Figure 3.1).

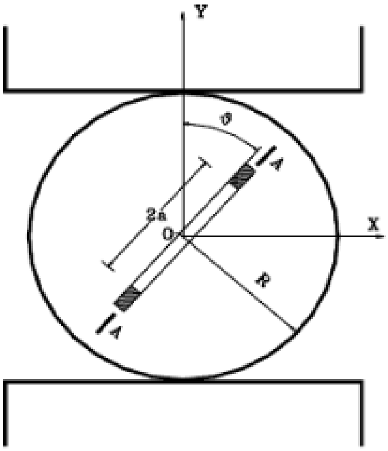

Figure 3.1. The cracked chevron notched Brazilian disk specimen (Chang et al., 2002)

In Figure 3.1, R and $2a$ refers to the radius of the specimen and crack length, respectively. The K_{Ic} is computed by equation below;

$$K_{Ic} = \frac{P_{max}}{B\sqrt{D}} Y^{*}_{min} \tag{3.1}$$

where;

P_{max} = failure load

D = diameter of the specimen

B = thickness of the specimen

Y^{*}_{min} = critical dimensionless stress intensity value

3.2. Short Rod Method

The application of the tensile load for specimens has not been preferred because of some difficulties practically. The specimen preparation sharp notch and data process are examples of the difficulties. The short rod method was found by Barker (1977). International Society for Rock Mechanics (ISRM) suggested this method to evaluate fracture toughness (Ouchterlony, 1988). The tensile load is applied to the core rock specimen in this method. The axis of the core specimen should be oriented parallel or perpendicular to any anisotropy characteristic properties. The rock core specimen has a chevron notch or V-shaped notch in the short rod method (Figure 3.2).

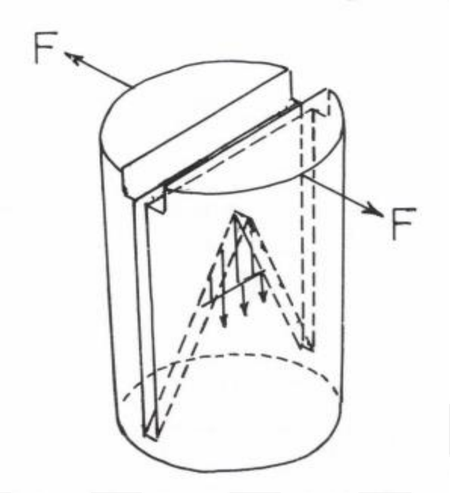

Figure 3.2. The sort rod specimen (Mueller, 1991)

In Figure 3.2, F refers to the applied tensile load. The K_{Ic} is computed by expression below;

$$K_{\mathrm{SR}} = C_{\mathrm{K}} 24 F_{max}/D^{1.5} \qquad (3.2)$$

where;

F_{max} = failure load

$C_{\mathrm{K}} = 1 - \frac{0.6\Delta W}{D} + \frac{1.4\Delta a_0}{D} - 0.01\Delta\theta$ (correction factor)

D = diameter of the specimen

ΔW = variation in specimen height

Δa_0 = initial position of chevron notch apex

$\Delta\theta$ = chevron notch angle

3.3. Chevron Bend Method

The chevron bend specimen was proposed by the ISRM (Ouchterlony, 1988). This method can be only used for Mode I fracture toughness determination. In this method, there is two notches. They are sawed with opposite angles to the rock core specimen. The specimen is under three-point bending. The chevron bend specimen is shown in Figure 3.3.

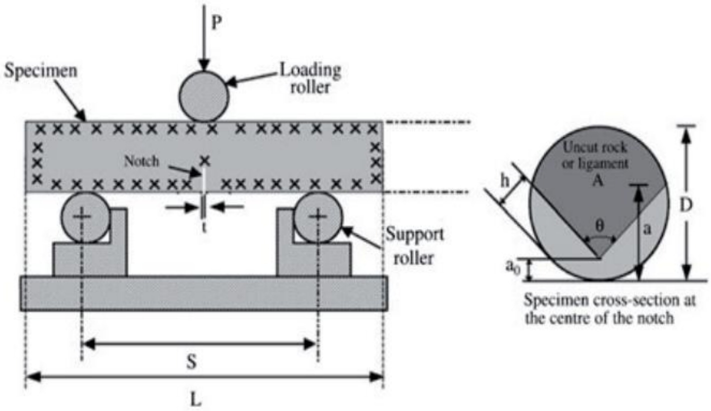

Figure 3.3. The chevron bend specimen (Hadei et al., 2017)

In Figure 3.3, *P, S, D, a, L* refers to the applied load, span length, diameter, notch length and length of the specimen, respectively. The fracture toughness value is computed by Equation 3.2 which is the same equation used in calculation of the fracture toughness in short rod method.

3.4. Semi Circular Bending Method

The SCB specimen was proposed by Chong and Kuruppu (1984), and many of the initial developments were done at the University of Wyoming (Kuszmau et al., 1987). A number tests for determination of the Mode I fracture toughness were applied with semi-circular specimens and the results from these tests were used for comparable to other techniques (Lim et al., 1994, June). In this method, three-point bending load is applied on a semi-circular disk specimen. On the upper side of this specimen a roller is put along the middle of the curvature to be applied load. The other two rollers are put under the specimen which are parallel to the upper one. A straight edge notch is sawed perpendicularly to the bottom surface along to the thickness which is parallel to the rollers. Two rollers are positioned to the notch with equal distances. The semi-circular bending specimen is shown in Figure 3.4.

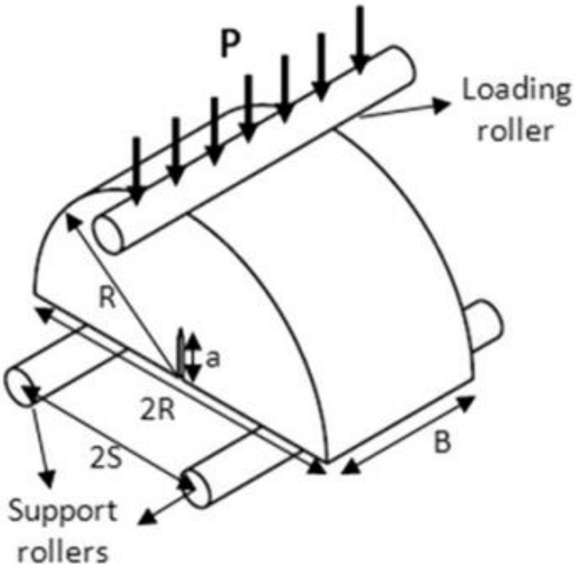

Figure 3.4. The semi-circular bending specimen (Elghazel et al., 2016)

In Figure 3.4, P, $2S$, B, a, $2R$, R refers to the applied load, span length, thickness, notch length, length and radius of the specimen, respectively. The K_{Ic} is computed by expression below;

$$K_{Ic} = Y_I \sigma_{cr} \sqrt{\pi a} \qquad (3.3)$$

where;

P = applied load

$Y_I = \frac{K_I}{\sigma_{cr}\sqrt{\pi a}}$ = (dimensionless stress intensity factor)

B = thickness of the specimen

R = radius of the specimen

$\sigma_{cr} = (P_{cr}/2RB)$

P_{cr} = load at fracture

Fracture toughness values of some rocks obtained from SCB method are given in Table 3.1.

Table 3.1. *Fracture toughness values for some rocks*

Rock name	K_{Ic}	**Span length (*2S*)**	***S/R***	**Reference**
	$MPa\sqrt{m}$	**mm**		
Oil shale	0.85	61, 18	0.80	Chong et al., 1987
Welsh Limestone	1.02	80, 120, 160	0.80	Singh & Sun, 1990 (b)
Jhonstone	0.06	47.5, 76	0.50, 0.80	Lim et al., 1994
Limestone	0.68	80	0.82	Khan & Al-Shayea, 2000
Granite	0.68	60, 80	0.80	Chang et al., 2002
Marble	0.87	60, 80	0.80	Chang et al., 2002
Marble	0.56	45, 60	0.60	Tutluoğlu & Keles, 2011
Kowloon Granite	1.24	50	0.62	Wong et al., 2019

3.5. Straight Notched Disk Bending Method

The straight notched disk bending specimen was first developed by Tutluoğlu & Keles (2011). This method is named as edge notched disk bend (ENBD) by Aliha (2017). The suggested three-dimensional specimen geometry with circular plate type is inherently stiffer than normal specimen geometries with beam type (Tutluoğlu & Keles, 2011). In this method, three-point bending load is applied on a cylindrical disk specimen. On the upper side of this specimen a roller is put along the central line to be applied load. The other two rollers are put under the specimen which are parallel to the upper central line to support the specimen. A straight edge notch is sawed perpendicularly to the bottom surface along to the path which is parallel to the rollers. Two rollers are positioned to the notch with equal distances for the supporting purpose. The specimen geometry is demonstrated in Figure 3.5.

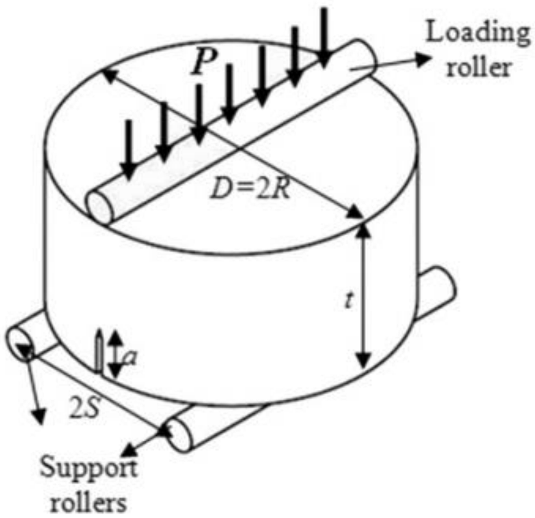

Figure 3.5. Straight notched disk bending specimen (Tutluoğlu & Keles, 2011)

In Figure 3.5, P, $2S$, t, a, D refers to the applied load, span length, thickness, notch length and diameter of the specimen, respectively. The K_{Ic} is computed by expression below;

$$K_{Ic} = Y_I \sigma_{cr} \sqrt{\pi a} \qquad (3.4)$$

where;

$P =$ applied load

$Y_I = \frac{K_I}{\sigma_{cr}\sqrt{\pi a}} =$ (dimensionless stress intensity factor)

$t =$ thickness of the specimen

$R =$ radius of the specimen

$\sigma_{cr} = (P_{cr}/2Dt)$

P_{cr} = load at fracture

CHAPTER 4

NUMERICAL MODELING OF THREE-POINT BEND SPECIMEN GEOMETRIES

The analytical solutions of the many engineering problems are based on partial differential equations. However, finding the exact solution of these problems for complex-shaped domains is very difficult. Therefore, the numerical computations of the stress intensity factors for the different beam geometries under three-point bending load are accomplished by the finite element method in this study.

The finite element method which is a numerical method is used for solving many difficult partial differential equations. In this method, the large system is divided into the smaller parts in order to solve the problem. The smaller parts are named as finite elements. The simple equations are obtained from these finite elements that are modeled. Connection of these elements are obtained by nodes. Later, these simple equations are added to a larger system of equations that model the whole problem. Some package programs have been developed for users to make numerical computations. ABAQUS, ANSYS, NASTRAN, LS-DYNA, FRANC2D/L and FRANC3D are some of them.

4.1. ABAQUS

The numerical computation of SIF in the models was done by ABAQUS 2019, which is a licensed software package of the METU computer center in this study. ABAQUS is user-friendly, considering the ease in learning and running tools compared with other programs.

4.1.1. ABAQUS Notation

ABAQUS package program employs six degrees of freedom for the nodes and the finite elements. These may vary independently. Three of them are referred as displacements in x, y, and z directions (u_1, u_2, u_3). The rest of them are referred as rotations which are (u_{r1}, u_{r2}, u_{r3}) about x, y, z axes (Figure 4.1).

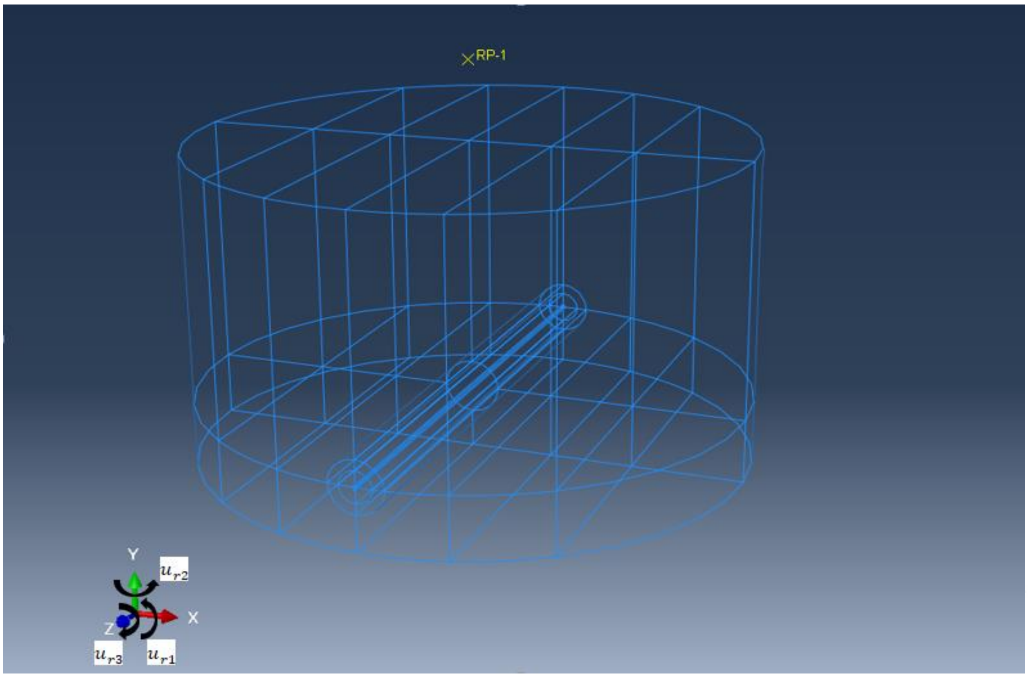

Figure 4.1. The degree of freedom for SNDB geometry in ABAQUS

The stress and strain components in ABAQUS are listed below.

- σ_{11} normal stress in the x- direction; which is S_{11}
- σ_{22} normal stress in the y- direction; which is S_{22}
- σ_{33} normal stress in the z- direction; which is S_{33}
- σ_{12} shear stress in the $x-y$ plane; which is S_{12}
- σ_{23} shear stress in the $y-z$ plane; which is S_{23}
- σ_{13} shear stress in the $x-z$ plane; which is S_{13}

Stresses are given in tensor notation as;

$[\sigma_{ij}]= \begin{bmatrix} \sigma_{11} & \sigma_{12} & \sigma_{13} \\ \sigma_{21} & \sigma_{22} & \sigma_{23} \\ \sigma_{31} & \sigma_{32} & \sigma_{33} \end{bmatrix}$ and in ABAQUS as: $\begin{bmatrix} s_{11} & s_{12} & s_{13} \\ s_{21} & s_{22} & s_{23} \\ s_{31} & s_{32} & s_{33} \end{bmatrix}$

- ε_{11} normal strain in the x-direction
- ε_{22} normal strain in the y -direction
- ε_{33} normal strain in the z -direction
- ε_{12} half of the shear strain in the $x - y$ plane
- ε_{13} half of the shear strain in the $x - z$ plane
- ε_{23} half of the shear strain in the $y - z$ plane

Strains are given in tensor notation as;

$[\varepsilon_{ij}]= \begin{bmatrix} \varepsilon_{11} & \varepsilon_{12} & \varepsilon_{13} \\ \varepsilon_{21} & \varepsilon_{22} & \varepsilon_{23} \\ \varepsilon_{31} & \varepsilon_{32} & \varepsilon_{33} \end{bmatrix}$ and in ABAQUS as: $\begin{bmatrix} E_{11} & E_{12} & E_{13} \\ E_{21} & E_{22} & E_{23} \\ E_{31} & E_{32} & E_{33} \end{bmatrix}$

The stress intensity factors in ABAQUS are denoted as K_I: Mode I stress intensity factor, K_{II}: Mode II stress intensity factor, K_{III}: Mode III stress intensity factor.

4.1.2. Useful Terms and Definitions in ABAQUS Modulus

There are lots of user friendly modules in ABAQUS. The first module is the part module. Models are created, edited and conducted in this module. Dividing of the whole bodies into the small parts is named as partition operation. This is used to create predefined parts and assigning mesh elements in the main geometry to these parts. The successful operation of the partitioning helps to form perfect meshes particularly for around the cracks. Furthermore, partitioning operation is used to identify queries for readings stress data and displacement in required areas. The face and cell are important terms for partition operation. The face term defines closed surfaces in two dimensional which are partitioned. The cell term defines closed volumes in three dimensional which are partitioned. These are used with labeling for several purposes such as assigning load, boundary conditions and mesh types, generating seam and crack, etc.

The second module is the property module. The characteristics of the material are entered into the property module. Assembly module is another useful tool. Part instances are generated in assembly module. It leads to position instances properly within a coordinate system in global. The next module is named as step. It is used for constituting a series for defining steps of the analysis process.

The other module is interaction module. It is used to create interaction, constraints and assign interaction property. Furthermore, the seam and crack are created in this module. The seam crack is an important term in this module to calculate the stress intensity factor. A seam refers to a face or a virtual edge that is closed in normally however it opens when analysis of the model is done. The seam has zero thickness. A seam cannot prolong throughout the boundaries of a model part a body. It should be embedded into in to a cell of a solid part of a three-dimensional model. The crack properties are determined by using an analysis of the contour integral after seam is created. Another term is a crack front which is defined within the interaction module. For the analyses of the contour integral, the crack front is defined firstly. The area from crack tip to first contour integral is named as the crack front. The crack front is used to analyze the first contour integral about singular stresses. The number of contour integral changes the accuracy of the analysis. This analysis is done with calculation of the J-integral of each contour. The contour integrals are computed on each node throughout the crack line. The crack line is defined by the connected edges in a series throughout crack front. This is defined with the crack extension direction which is expressed by q. Furthermore, singularity of the crack tip is another important definition. The cracks are modeled in this program with assumption of the small strain. This creates singularity at the crack tip. The singularity of the crack tip strain changes with used material in the model. It develops of the accuracy for the computation of the J-integral. The singularity of the strain is related by the $\varepsilon \propto r^{-1/2}$ for linear elasticity. In addition to these, the request of the history output is assigned in the module step to get data of the stress intensity factor near the crack tip.

The load module is used to assign load and define the boundary conditions to the model. The reference points can be used for applying load and defining boundary conditions. It refers an element which is unbounded. The reference point is not belonging to the main part of the model. Any applied mechanical effect is delivered to the desired area by using the reference point.

Mesh is generated in mesh module. Seeding property is used for the construction of the mesh. The term seeding is used to adjust the number of nodes per edge or instance. It helps controlling mesh density. The another module is job module. It is used for the submission for analysis. Progress of the analysis process can be followed in job module. The final module is visualization module. The outcomes of the analysis which can be like deformed shapes, plot contours, symbols and material orientations on deformed shape, animation are shown in this module.

4.2. Verification Work for the Modeling Procedure

To assess the accuracy of the stress intensity factor computation of the ABAQUS 3D modeling work for SNDB specimen geometry, two problems for which analytical solutions are available are chosen. The three-point bending plate problem is the first problem. In this verification problem, plate is under three-point bending condition which is very similar to the SNDB method. Another verification example is the modeling of well-known and ISRM suggested SCB specimen geometry under three-point bending. The results from the analytical solutions and numerical solutions were compared between them.

In the verification work, seam crack length of 10 mm is used for all models. The reason for this is to keep the crack length as small as possible so that effect of outer and loaded boundaries is minimized regarding the crack tip stress field.

4.2.1. Three-Point Bending Plate Problem

The numerical model of the three-point bending plate is constructed with three steel rollers and one plate loaded by three-point bending action of the rollers, (Figure 4.2).

Dimensions used for the plate are given in Table 4.1. *a/W* and *S/a* ratios are taken to be equal to 0.5 and 8, respectively. The material properties of the plate assigned to ABAQUS such as elastic modulus (*E*) and Poisson's ratio (ν) do not affect the stress intensity factor results of the crack in the plate. The roller diameter is assigned as 10 mm. The material properties of the steel rollers are elastic modulus (*E*) of 200 GPa and Poisson's ratio (ν) 0.30 for steel rollers.

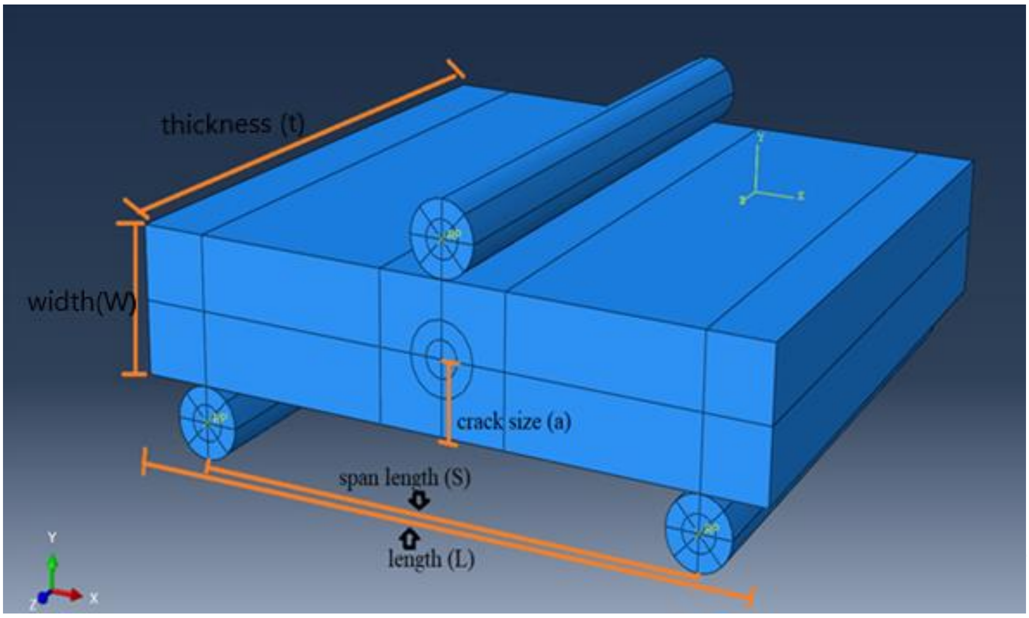

Figure 4.2. Geometry of the three-point bending plate model

Table 4.1. *Dimensions for square plate*

Dimension	Value
Thickness (*t*)	100
Width (*W*)	20
Length (*L*)	100
Span length (*S*)	80
Crack size (*a*)	10

Two support rollers at the bottom are in contact with the plate. The third roller at the top is placed along the central path. A reference point is assigned above the upper steel roller. The load is transferred to the plate via reference point. 1 N vertical load is distributed throughout the upper central path of the plate (Figure 4.3).

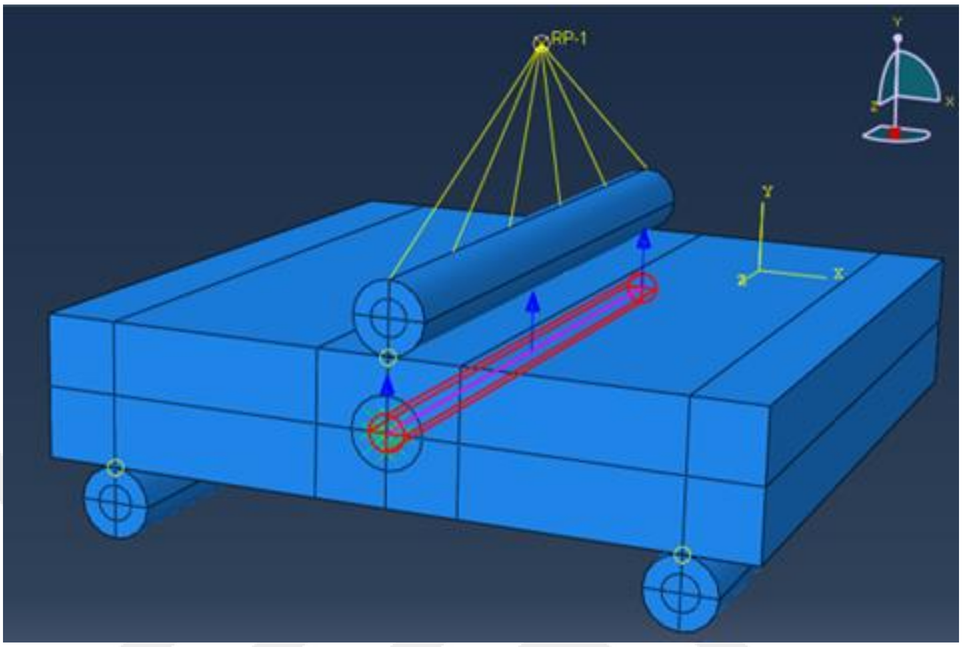

Figure 4.3. The loading of the three-point bending plate geometry with rollers

The seam crack is assigned along the bottom central path of the plate. Special contour integral paths and partitions are used at the immediate crack front. The reason for forming a circular pattern around the crack tip is to increase the accuracy of SIF computations. The contour integrals are used in J-Integral method to compute SIF. The crack line and crack extension direction of the three-point bending plate can be seen in Figure 4.3.

Bottom support rollers are assigned fixed displacements in y and z direction. The reference point and steel roller which are at the top of the plate are fixed in x and z direction.

The fine mesh was applied around the contour integrals. The mesh and the undeformed and the deformed states of the model can be seen in Figure 4.4.

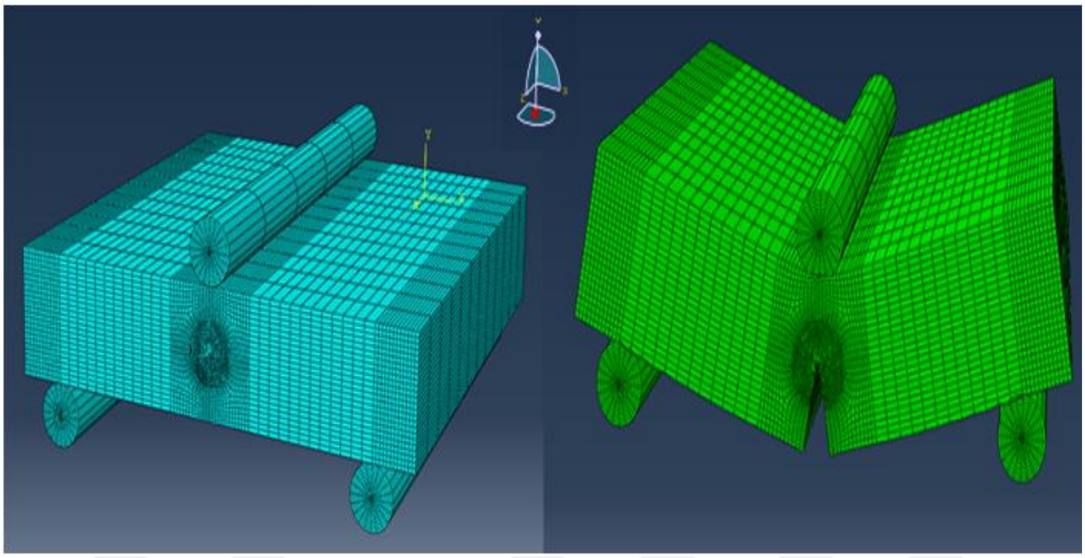

Figure 4.4. The mesh geometry of the three-point bending plate model with steel rollers

According to the numerical modelling of the three-point bending problem, mode I stress intensity factor (K_I) was computed as 738.49 $Pa\sqrt{m}$.

A polynomial expression was developed by Srawley (1976) to calculate the stress intensity factor for a square plate under plane strain condition. The ratio of the and stress intensity factor formulas were expressed as a function f(a/W) in Equations 4.1 and 4.2.

$$f\left(\frac{a}{W}\right)=3\left(\frac{a}{W}\right)^{1/2}\left[\frac{1.99-\left(\frac{a}{W}\right)\left(1-\frac{a}{W}\right)\left(2.15-\frac{3.93a}{W}+\frac{2.7a^2}{W^2}\right)}{2\left(1+\frac{2a}{W}\right)\left(1-\frac{a}{W}\right)^{\frac{3}{2}}}\right] \tag{4.1}$$

$$K_I=\frac{P*S*f\left(\frac{a}{W}\right)}{BW^{\frac{3}{2}}} \tag{4.2}$$

For $0 \leq \alpha = a/W \leq 1$ and where;

K_I= Stress intensity factor

B= Thickness

W= Width

a= Crack length

S= Span length

The mode I stress intensity factor (K_I) is calculated as 752.36 $Pa\sqrt{m}$ analytically. The difference between the numerical and analytical solution is 1.88%. It should be noted that the numerical solution is 3D-based while the analytical solution is 2D-based under plane strain.

4.2.2. Modeling of the SCB Specimen

SCB specimen geometry is modeled in 3D. Loading span lengths are varied between S/R=0.40-0.90. The crack length is fixed as 10 mm resulting in a/R=0.20. 100 mm diameter SCB geometries with 50 mm thicknesses (t/R=1) are modeled. The span length is set as $2S$= 40, 45, 50, 55, 60, 70, 80, 85 and 90 mm. Nine different geometries are modeled in 3D to compute the SIF of SCB. Figure 4.5 shows a typical SCB model illustrating the geometric details. Model dimensions are given in Table 4.2.

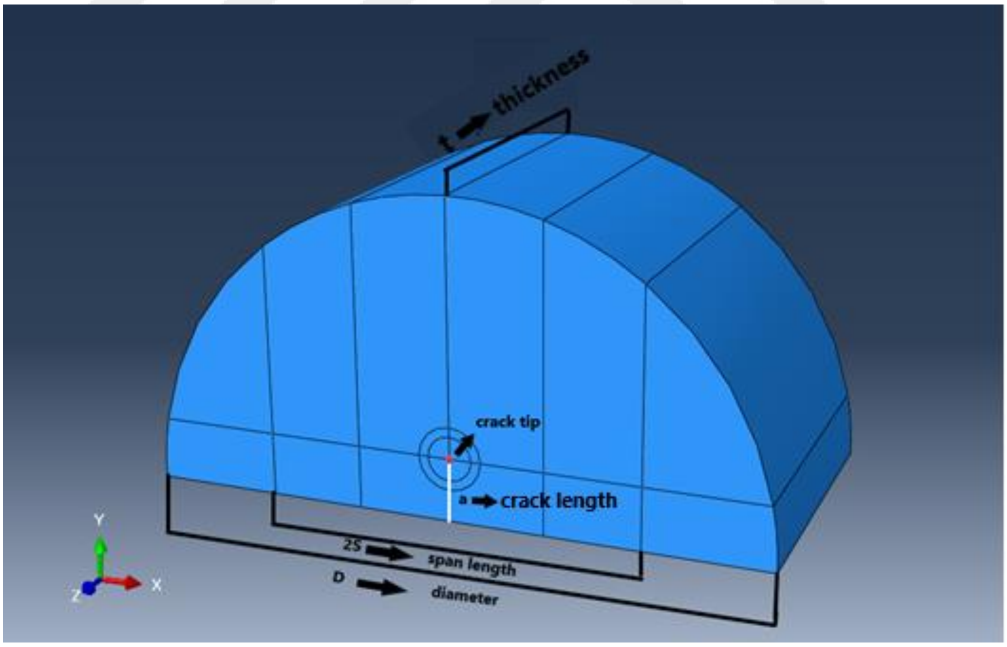

Figure 4.5. SCB model geometry

Table 4.2. *Dimensions of the SCB models*

Number of the model	*t*	*2S*	*a/S*	*S/R*
	mm	mm		
1	50	40	0.50	0.40
2	50	45	0.44	0.45
3	50	50	0.40	0.50
4	50	55	0.36	0.55
5	50	60	0.33	0.60
6	50	70	0.29	0.70
7	50	80	0.27	0.80
8	50	85	0.24	0.85
9	50	90	0.22	0.90

The crack extension direction and the crack front are assigned as in Figure 4.6. Three different partition circles are used to define the contour integral region. The outermost radius of the contour integral region is set as 5 mm. The intermediate and the innermost radius of the contour integral region are set as 3.5 mm, 0.25 mm, respectively. For the reference point generating the load at top, displacements are fixed in x-direction (u_1) and z- direction (u_3). For the upper loading path, which is perpendicular the crack extension direction, displacement is fixed in x-direction (u_1). For the corner points under the specimen, displacements are fixed in z-direction (u_3). Displacements of the lines applying the bottom supports are fixed in y-direction (u_2).

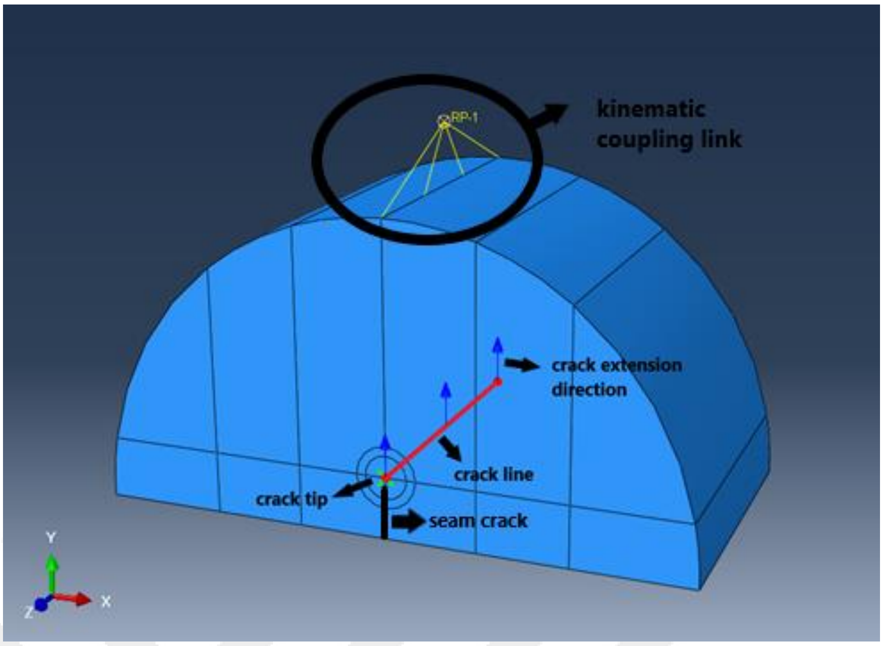

Figure 4.6. Crack tip, crack line and crack extension direction of the SCB model geometry

A vertical line load of -1 N is applied to the upper boundary from a reference point above the boundary. The reference point RP-1 convert the concentrated load to a distributed load. The area occupied by the innermost radius of the contour integral region is meshed by the hex-dominated element type with sweep technique. A finer mesh is constructed around the crack tip (Figure 4.7).

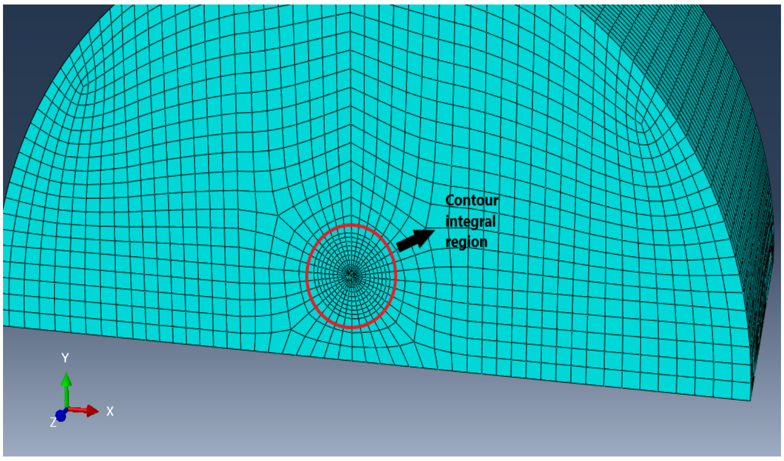

Figure 4.7. Contour integral region and the crack tip mesh

The deformed shape and undeformed shape geometries are shown in Figure 4.8.

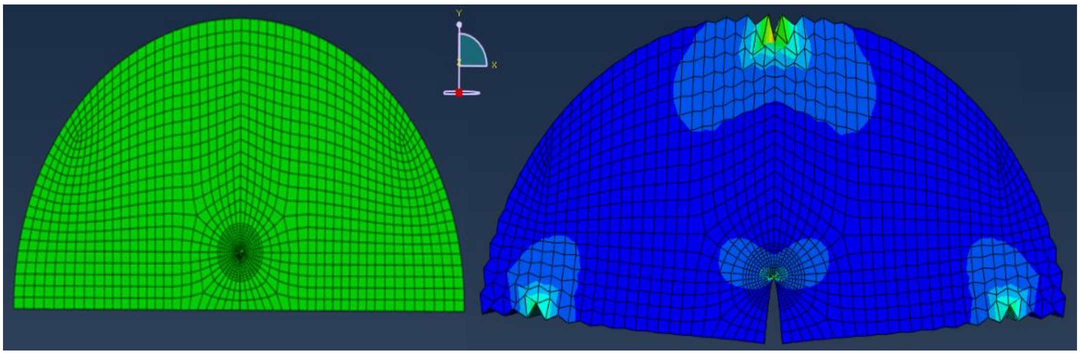

Figure 4.8. Undeformed and deformed shape of the SCB model geometry

The dimensionless stress intensity factor (Y_I) of SCB model geometry for mode I is formulated by the following equations;

$$Y_I = \frac{K_I}{\sigma_0 \sqrt{\pi a}} \qquad (4.3)$$

$$\sigma_0 = \frac{P}{2\mathrm{Rt}} \qquad (4.4)$$

Sample calculation procedure for SCB model with *S/R*=0.40 as follows;

where;

P = applied load (1 N)

R = radius (0.05 m)

t = thickness (0.05 m)

a = crack length (0.01 m)

$K_I = 64.48\ \mathrm{Pa}\sqrt{\mathrm{m}}$

$$\sigma_0 = (1/(2 \times 0.05 \times 0.05)$$

$$\sigma_0 = 200\ \mathrm{Pa}$$

$$Y_I = \frac{64.48}{200\sqrt{\pi 0.01}} = 1.82$$

K_I results and dimensionless mode I stress intensity factors (Y_I) of nine SCB model geometries are listed in Table 4.3.

Table 4.3. *K_I and Y_I of the SCB models*

Beam thickness (*t*)	**S/R**	**K_I**	**Y_I**
m		**$\mathrm{Pa}\sqrt{\mathrm{m}}$**	
50	0.40	64.48	1.82
	0.45	77.35	2.18
	0.50	89.72	2.53
	0.55	101.81	2.87
	0.60	113.90	3.21
	0.70	138.33	3.90
	0.80	163.63	4.62
	0.85	176.61	4.98
	0.90	189.96	5.36

The analytical solution for computing Y_I of SCB geometry is given in Lim (1993). The solution is based on plane strain assumption. Lim (1993) tabulated the dimensionless stress intensity factors for varying *a/R* and *S/R*. Tables are referred for the entries here that are a crack length/radius ratio of *a/R*=0.20 and span length/radius ratios of 0.50 and 0.80.

Y_I results of the SCB geometry computed from Lim's tables are 2.51 and 4.59 for S/R=0.50 and 0.80, respectively. Modeling work here yields 2.53 and 4.62 for the relevant loading spans. Results are close to differences around 1%.

Graphical illustration of the Y_I versus span length *S/R* of the SCB from numerical models and Lim's equations are shown in Figure 4.9.

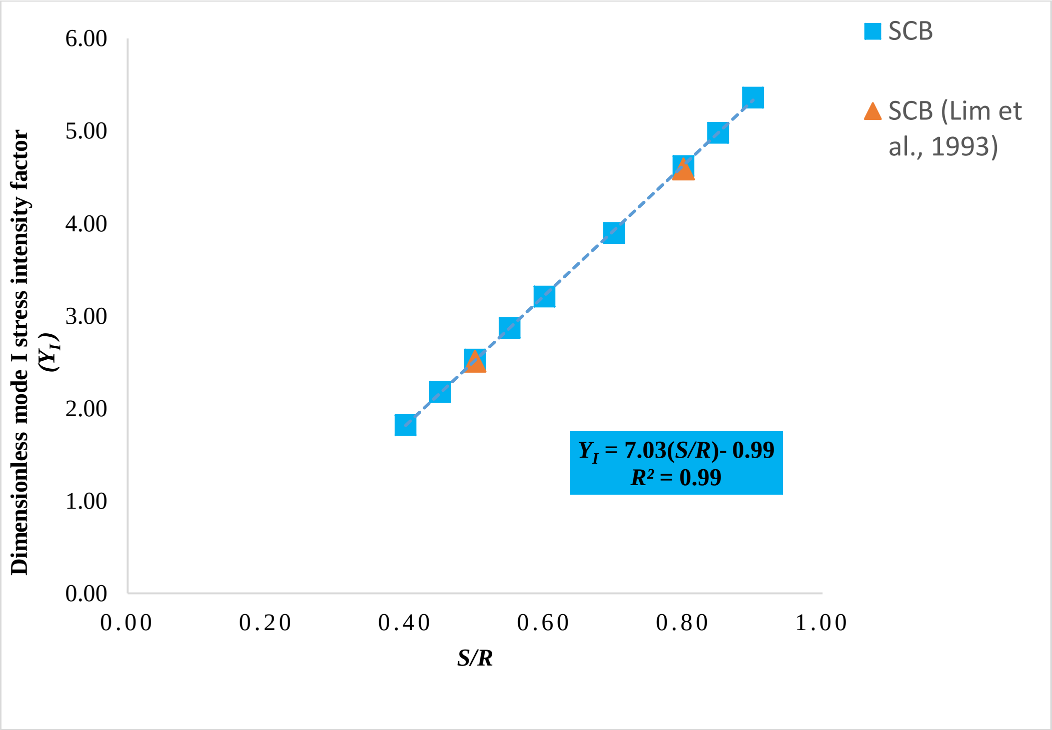

Figure 4.9. Dimensionless mode I SIF vs *S/R* results

Following the curve fitting process, a linear relation expresses the variation of Y_I with *S/R* as in Srawley equation in the previous verification effort. For estimating the dimensionless mode I stress intensity factor of SCB model geometries for different loading spans, following equation is proposed;

$$Y_{I(1.0)} = 7.032\left(\frac{S}{R}\right) - 0.996 \quad \text{for } \frac{t}{R} = 1.0 \qquad (4.5)$$

4.3. For Deciding the Optimum Crack Length and Comparison Purposes 3D of the SNDB Geometries and Comparison SIF

The stress intensity factors of the SNDB circular plate geometry was to be computed by using the ABAQUS finite element program. SNDB specimen geometry was modeled with two different thicknesses. 100 mm diameter SNDB geometries with 50 mm and 60 mm thicknesses were modeled. Two span lengths were varied by 60 mm and 80 mm, corresponding to *S/R*= 0.60 and *S/R* =0.80. The preliminary crack lengths of 10, 12 mm and 24 mm were inserted to the models. Totally, twelve different geometries were modeled in 3D to compute the Y_I of SNDB geometry in ABAQUS (Table 4.4).

Table 4.4. *Dimensions of the SNDB specimen geometry for computation of* Y_I

Number of the model	***a***	***t***	***2S***	***S/R***
	mm	**mm**	**mm**	
1	10	50	60	0.60
2	12	50		
3	24	50		
4	10	60		
5	12	60		
6	24	60		
7	10	50	80	0.80
8	12	50		
9	24	50		
10	10	60		
11	12	60		
12	24	60		

For comparison, computation of Y_I can be done by using the formulas in Tutluoğlu & Keles (2011). A linear relationship including the variable *S/R* is suggested. Slope m and the intercept are presented in terms of geometrical entities *a/t* and *t/R* Tutluoğlu & Keles (2011). Dimensionless stress intensity factor $Y_{I(SNDB)}$ by is expressed as

$$Y_{I(SNDB)} = m\left(\frac{S}{R}\right) + n \qquad (4.6)$$

To compute the $Y_{I(SNDB)}$ variation with thickness of the circular plate another expression is suggested in Tutluoğlu & Keles (2011). Dimensionless stress intensity factor $Y_{I(SNDB)}$ is expressed as

$$Y_{I(SNDB)} = C_1(\frac{t}{R})^5 + C_2(\frac{t}{R})^4 + C_3(\frac{t}{R})^3 + C_4(\frac{t}{R})^2 + C_5\left(\frac{t}{R}\right) + C_6 \qquad (4.7)$$

Coefficients in Equation 4.7 are given in terms of *a/t* and *S/R* in Tutluoğlu & Keles (2011).

All results of the dimensionless stress intensity factor (Y_I) for 2S=60 mm are given in Table 4.5.

Table 4.5. *Comparison of the Y_I of the SNDB for 2S=60 mm*

Thickness (mm)	**Notch length (mm)**	**Y_I ABAQUS**	**Y_I Linear Relation (Eq. 4.6)**	**Difference (%)**	**Y_I Variation (Eq. 4.7)**	**Difference (%)**
50	10	3.16	3.11	1.61	3.11	1.61
50	12	3.30	3.14	5.10	3.14	5.10
50	24	4.26	4.15	2.65	4.15	2.65
60	10	2.74	2.80	2.19	2.70	1.48
60	12	2.80	2.72	2.94	2.58	8.53
60	24	2.97	3.04	2.36	2.85	4.21
Average±STD				2.80±1.21		3.93±2.67

All results of the dimensionless stress intensity factor (Y_I) for *2S*=80 mm are given in Table 4.6.

Table 4.6. *Comparison of the Y_I of the SNDB for 2S=80 mm*

Thickness (mm)	**Notch length (mm)**	**Y_I ABAQUS**	**Y_I Linear Relation (Eq. 4.6)**	**Difference (%)**	**Y_I Variation (Eq. 4.7)**	**Difference (%)**
50	10	4.41	4.29	2.79	4.29	2.79
50	12	4.51	4.38	2.97	4.38	2.97
50	24	5.56	5.86	5.40	5.56	5.40
60	10	3.79	3.91	3.16	3.69	2.71
60	12	4.05	3.87	4.65	3.65	10.96
60	24	4.56	4.40	3.63	4.16	9.61
Average±STD				3.77±1.04		5.74±3.69

The difference of Y_I between numerical models and the formulas is around 5% and less all cases above.

The minimum differences between the Y_I of the SNDB obtained from numerical models and formulas are observed for the models with 10 mm crack length. Hence, a crack length of 10 mm is selected to be inserted to all SNDB model geometries

4.4. Convergence Study for Contour Integral Region

The number of contours around the crack tip is so important in mesh intensity studies. To find the accurate number of contours for stress intensity factor, different number of contours (4, 6, 10, 14, 16 and 20) were used (Figure 4.10).

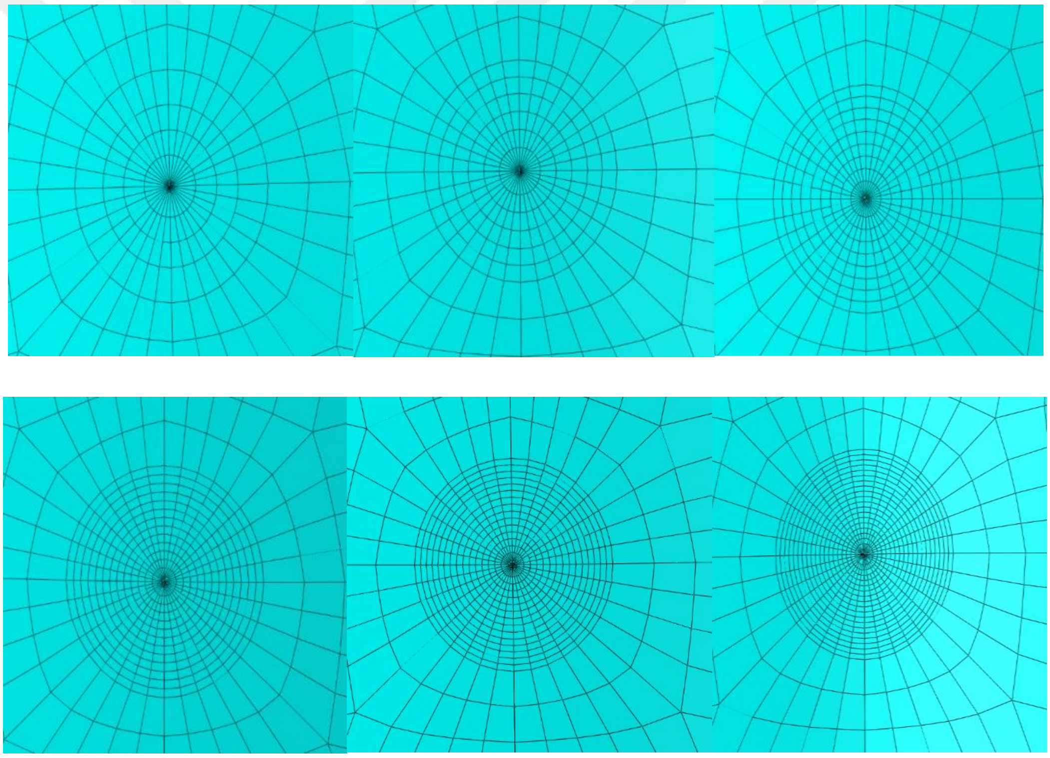

Figure 4.10. Different number of contours near the crack tip

The K_I results from the models were plotted against the number of contours around the crack tip in Figure 4.11.

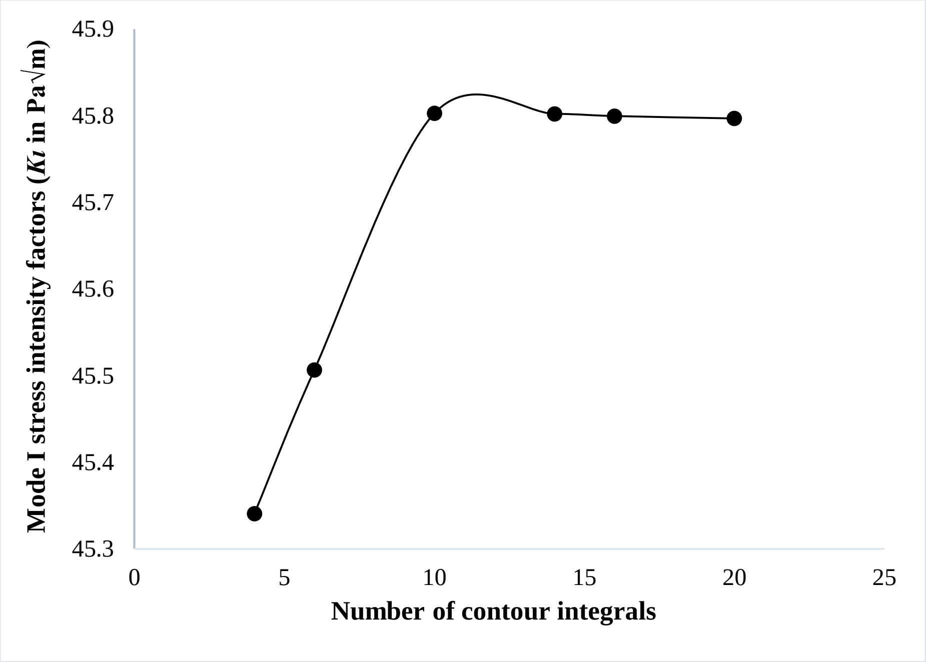

Figure 4.11. K_I versus number of contours near the crack tip

K_I approaches the specific value with increasing the number of contours around the crack tip as seen in Figure 4.11. It can be concluded that 10 contours in the contour integral region are sufficient to analyze the stress intensity factor.

4.5. Modeling of the SNDB Specimen

SNDB (straight notched disk bending) specimen geometry is modeled in 3D. Loading span lengths are varied between *S/R*=0.40-0.90. The crack length is fixed as 10 mm resulting in *a/R*=0.20. 100 mm diameter SNDB geometries with 50 mm and 60 mm thicknesses (*t/R*=1 and *t/R*=1.2) are modeled. The span length is set as *2S*= 40, 45, 50, 55, 60, 70, 80, 85 and 90 mm. Eighteen different geometries are modeled in 3D to compute the SIF of SNDB. Figure 4.12 shows a typical SCB model illustrating the geometric details. Model dimensions are given in Table 4.7.

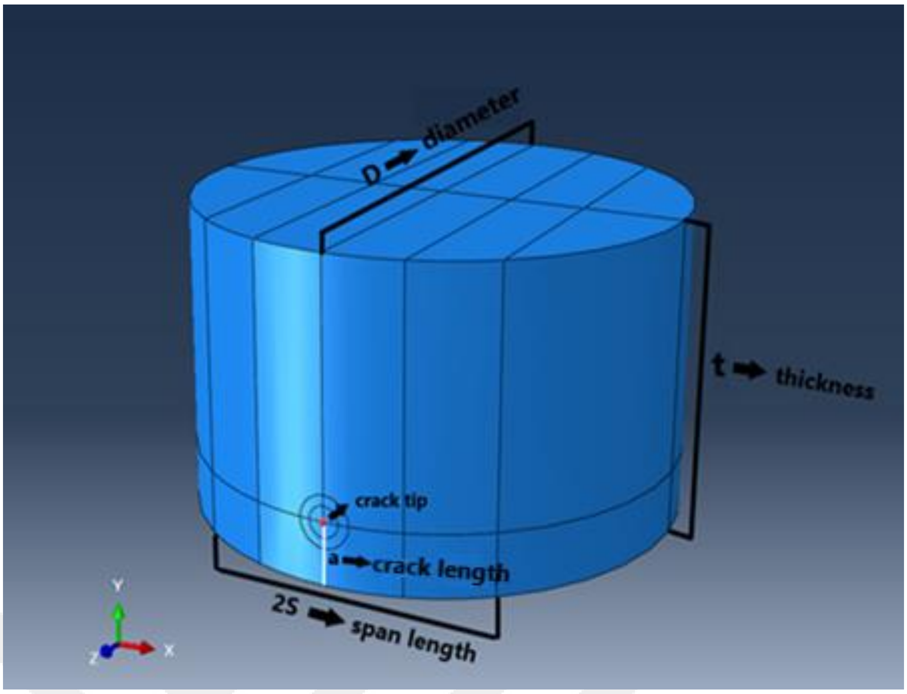

Figure 4.12. Model Geometry of the SNDB specimen

Table 4.7. Dimensions of the SNDB models

Number of the model	*t*	*2S*	*a/S*	*S/R*
	mm	mm		
1	50	40	0.50	0.40
2	50	45	0.44	0.45
3	50	50	0.40	0.50
4	50	55	0.36	0.55
5	50	60	0.33	0.60
6	50	70	0.29	0.70
7	50	80	0.27	0.80
8	50	85	0.24	0.85
9	50	90	0.22	0.90
10	60	40	0.50	0.40
11	60	45	0.44	0.45
12	60	50	0.40	0.50
13	60	55	0.36	0.55
14	60	60	0.33	0.60
15	60	70	0.29	0.70
16	60	80	0.27	0.80
17	60	85	0.24	0.85
18	60	90	0.22	0.90

The crack extension direction and the crack front are assigned as in Figure 4.13. The ratio between the contour integral region radius and model radius is set to 0.1 for SNDB geometries (Tutluoğlu & Keles, 2011). Three different partition circles are used to define the contour integral region. The outermost radius of the contour integral region is set as 5 mm. The intermediate and the innermost radius of the contour integral region are set as 3.5 mm, 0.25 mm, respectively. For the reference point generating the load at top, displacements are fixed in x-direction (u_1) and z- direction (u_3). For the upper loading path, which is perpendicular the crack extension direction, displacement is fixed in x-direction (u_1). For the lines upper and bottom of the specimen, perpendicular to the crack line direction, displacements are fixed in the z-direction (u_3). Displacements of the lines applying the bottom supports are fixed in y-direction (u_2).

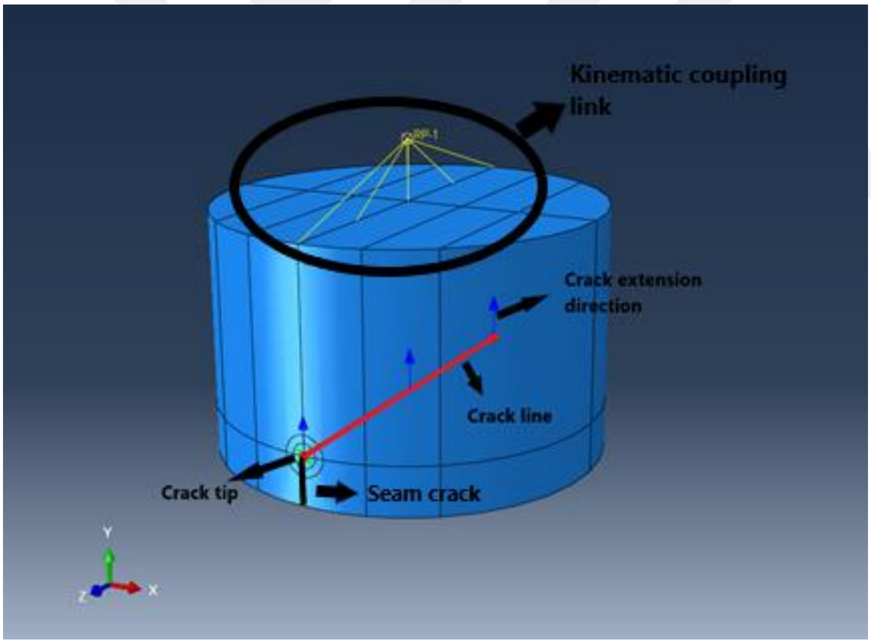

Figure 4.13. Crack tip, crack line and crack extension direction of the SNDB specimen

A vertical line load of -1 N is applied to the upper boundary from a reference point above the boundary. The reference point RP-1 convert the concentrated load to a distributed load.

The area occupied by the innermost radius of the contour integral region is meshed by the hex-dominated element type with sweep technique. A finer mesh is constructed around the crack tip (Figure 4.14).

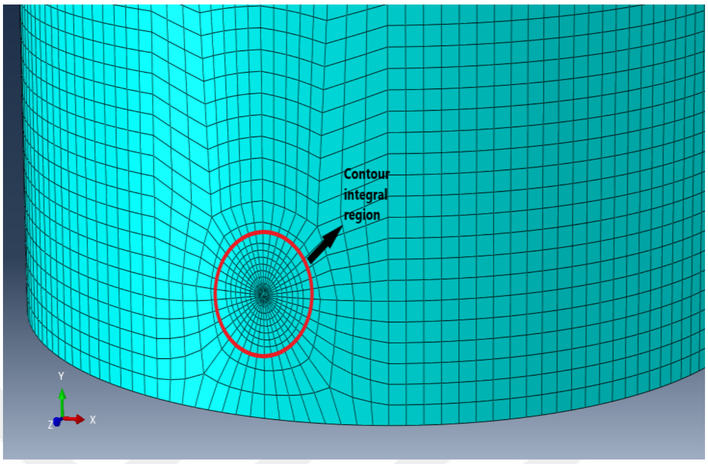

Figure 4.14. Contour integral region and the crack tip mesh

The deformed shape and undeformed shape geometries are shown in Figure 4.15.

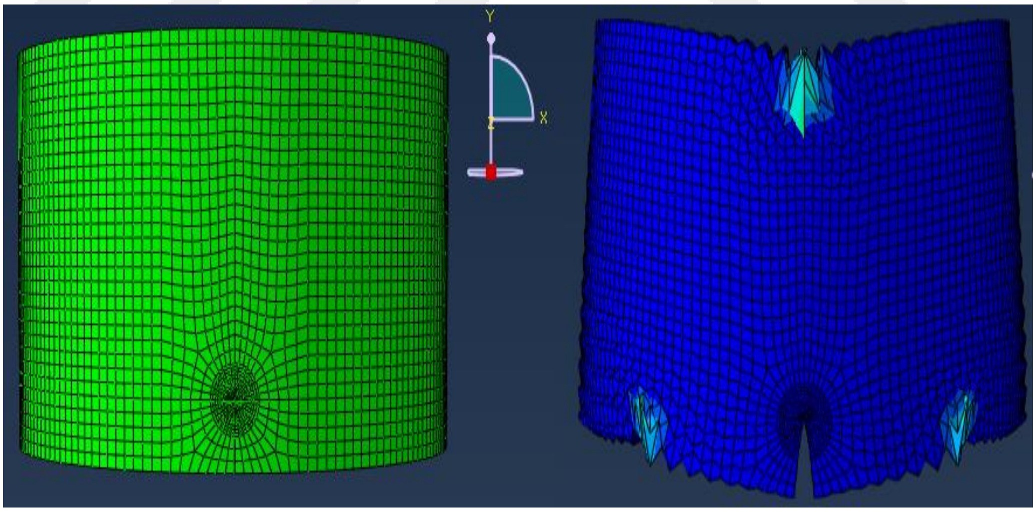

Figure 4.15. Undeformed and deformed shape of the SNDB model geometry

The dimensionless stress intensity factor (Y_I) of SNDB model geometry for mode I is formulated by the following equations.

$$Y_I = \frac{K_I}{\sigma_0\sqrt{\pi a}} \qquad (4.8)$$

$$\sigma_0 = \frac{P}{2\mathrm{Dt}} \qquad (4.9)$$

Sample calculation procedure for 60 mm thick model with *S/R*=0.40 as follows;

where;

P= applied load (1N)

D= diameter (0.1 m)

t= thickness (0.06 m)

a= crack length (0.01 m)

K_I =22.76 Pa$\sqrt{\mathrm{m}}$

$$\sigma_0 = (1/(2 \times 0.1 \times 0.06)$$

$$\sigma_0 = 83.33 \text{ Pa}$$

$$Y_I = \frac{22.76}{83.33\sqrt{\pi 0.01}} = 1.54$$

K_I results and dimensionless mode I stress intensity factors (Y_I) of eighteen SNDB model geometries are listed in Table 4.8.

Table 4.8. *Dimensionless mode I stress intensity factors (Y_I) for SNDB models*

Beam thickness (*t*)	***S/R***	K_I	Y_I
m		$\mathbf{Pa\sqrt{m}}$	
50	0.40	33.87	1.91
	0.45	40.02	2.26
	0.50	45.80	2.58
	0.55	51.34	2.90
	0.60	55.95	3.16
	0.70	67.41	3.80
	0.80	78.09	4.41
	0.85	83.48	4.71
	0.90	88.91	5.02
60	0.40	22.76	1.54
	0.45	27.71	1.87
	0.50	32.23	2.18
	0.55	36.46	2.47
	0.60	40.51	2.74
	0.70	48.31	3.27
	0.80	56.04	3.79
	0.85	59.94	4.06
	0.90	63.85	4.32

Graphical illustration of the Y_I versus span length *S/R* for *t*=60 mm and *t*= 50 mm are shown in Figure 4.16.

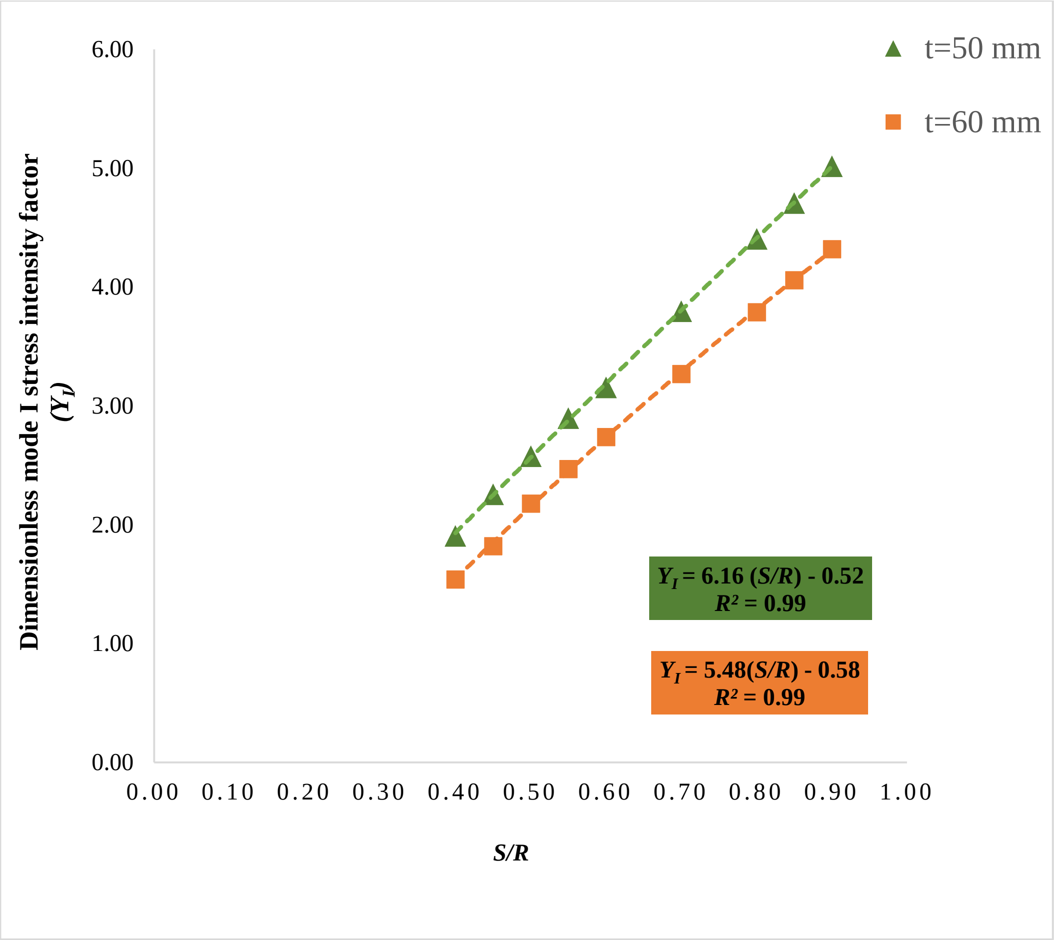

Figure 4.16. Y_I versus *S/R* two different beam thicknesses of the SNDB model geometry

Following the curve fitting process, a linear relation expresses the variation of Y_I with *S/R* as in Srawley equation. For estimating the dimensionless mode I stress intensity factor of SNDB model geometries for different loading spans, following equations are proposed;

$$Y_{I(1.0)} = 6.1604\left(\frac{S}{R}\right) - 0.5192 \quad \text{for } \frac{t}{R} = 1.0 \qquad (4.10)$$

$$Y_{I(1.2)} = 5.4779\left(\frac{S}{R}\right) - 0.5842 \quad \text{for } \frac{t}{R} = 1.2 \qquad (4.11)$$

CHAPTER 5

TESTING WORK FOR CONVENTIONAL MECHANICAL PROPERTIES

The grey colored Ankara Gölbaşı Andesite rock blocks were used for experimental study. Static deformability and indirect tensile (Brazilian) tests were done to examine the mechanical properties of the Ankara Gölbaşı Andesite. The values of the uniaxial compressive strength (UCS), Young's modulus (E) and Poisson's ratio (υ) were acquired from the deformability tests. Tensile strength was obtained from the indirect tensile (Brazilian) test. Tests for mechanical and physical properties were performed following ISRM suggested procedures. Servo-controlled MTS Rock Testing Machine was used for loading the specimens.

For specimen preparation, large blocks were drilled by the boring machine to extract cores. Specimen grinding and polishing finishes the preparation work and specimens of targeted diameter and thickness are ready for testing.

5.1. Texture of Grey Ankara Gölbaşı Andesite

The type of Ankara Gölbaşı andesite has grey color. Previous experimental work results were available for grey Ankara Gölbaşı andesite in the Mining Engineering Department of the Middle East Technical University. Mechanical and physical properties of this rock were compared with results of tests by different studies and persons (Table 5.1).

Table 5.1. *Material properties of andesite from different studies*

Reference	***E*** **(GPa)**	***υ***	**UCS (MPa)**	***T_o*** **(MPa)**
Tutluoğlu & Keleş (2011)	12.3±0.1	0.15±0.01	82.8±4.1	7.0±0.67
Özdoğan (2017)	21.9±1.3	0.15±0.01	84.7±7.1	9.6±1.8
Present work	28.3±1.1	0.16±0.01	100.8±4.9	8.6±1.1

Significant differences were observed between the values of the material properties. In order to investigate what caused the wide variation in the properties, thin section analysis in Geological Engineering Department was carried out from a sample taken from the indirect tensile strength test. Analysis results show that there are some flowing tendencies of oriented flaws in these samples. These flowing trends were less frequent in some samples (Figure 5.1) and highly dominant in some others (Figure 5.2). The loading applied to the sample can be parallel or perpendicular to these flowing trends; and this effects the test results for Ankara andesite even rock blocks are picked from neighboring locations (T. Topal, personal communication, November 8, 2019).

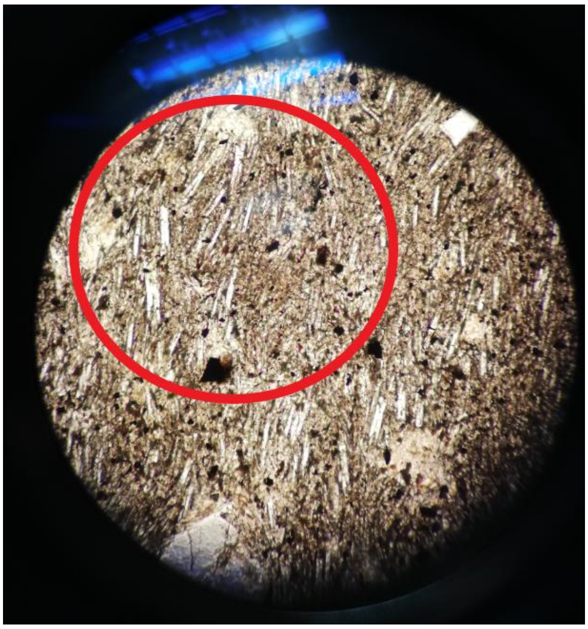

Figure 5.1. Brazilian test specimen thin section with less frequent flaw population

Figure 5.2. Brazilian test specimen thin section with high frequent flaw population

5.2. Static Deformability Test

Static deformability tests were performed on core specimens of Ankara Gölbaşı Andesite. Modulus of elasticity and Poisson’s ratio were measured. Specimens were loaded to failure to obtain the uniaxial compressive strengths (UCS). Four NX size andesite core specimens were used. The MTS 815 Material Testing System with displacement-controlled way with a rate of 0.0005 mm/s was used in the tests. The specimens had approximately 54 mm diameter and 130 mm length maintaining a $L/D \geq 2$. For the measurement of elastic constants, clip-on gage extensometers were attached longitudinally and laterally to detect axial and circumferential deformations (Figure 5.3).

Figure 5.3. Static deformability test configuration

Static deformability test specimens before and after the testing are shown in Figure 5.4.

Figure 5.4. Static deformability test specimens before and after testing

MTS Flextest40 controller box for data acquisition was used to obtain data from static deformability tests. Results of failure loads, elastic modulus, Poisson's ratio and uniaxial compressive strength values are given in Table 5.2.

Table 5.2: *Results of static deformability tests*

Specimen	**Diameter (mm)**	**Length (mm)**	**Failure Load (kN)**	**Elastic Modulus (GPa)**	**Poisson's Ratio**	**Uniaxial Compressive Strength (MPa)**
SD-1	54.7	129.8	240.2	28.1	0.16	102.1
SD-2	54.6	129.6	226.6	27.6	0.17	96.7
SD-3	54.7	129.3	226.1	27.6	0.14	97.3
SD-4	54.6	129.9	251.5	30.0	0.15	107.2
Average	54.7±0.1	129.7±0.3	236.1±12.2	28.3±1.1	0.16±0.01	100.8±4.9

From the data, stress-strain curves were drawn. Figure 5.5 shows a typical stress and strain curve for first specimen of static deformability tests. Figure 5.6 shows a typical lateral strain and axial strain curve for first specimen of static deformability tests. All static deformability test curves can be seen in Appendix A.

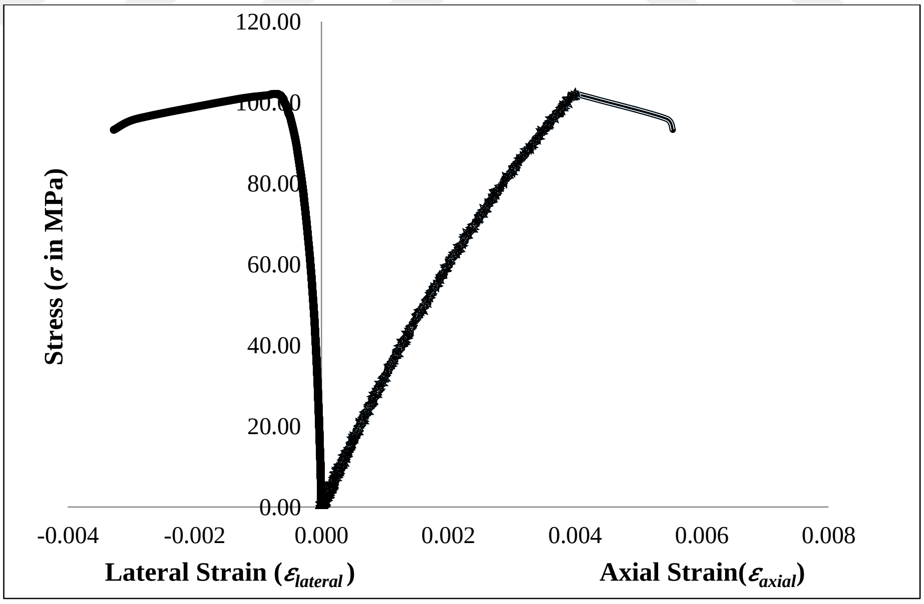

Figure 5.5. Stress versus strain curves for SD-1 specimen

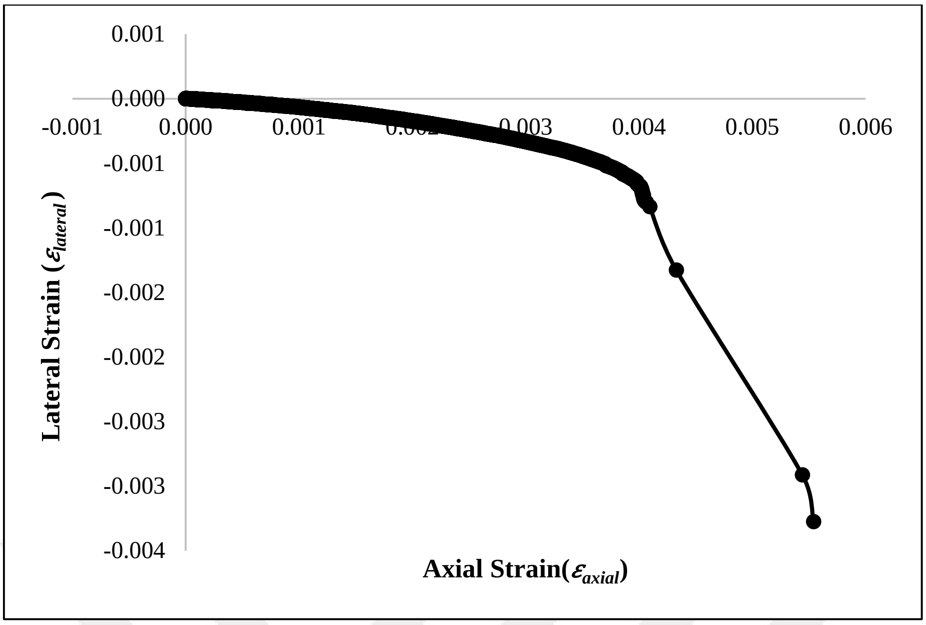

Figure 5.6. Lateral strain versus axial strain curve for SD-1 specimen

The tangent modulus was drawn at around 50% stress level and strain level to find the elastic modulus (E) and Poisson's ratio (υ).

5.3. Indirect (Brazilian) Test

The tensile strength was measured by indirect tensile strength tests. Nine Ankara Gölbaşı Andesite specimens were used. Five of them had approximately 54 mm diameter and thicknesses around 33 mm. Five disk specimens were compressed by using the two opposing curved jaws (Figure 5.7). Two disk specimens which had approximately 54 mm diameter and thicknesses around 27 mm were compressed without jaws. Additional two disk specimens which had approximately 100 mm diameter and thicknesses around 50 mm were compressed without jaws (Figure 5.8). Disk specimens were loaded by using the MTS 815 Material Testing System with displacement-controlled fashion with a rate of 0.001 mm/s.

Figure 5.7. The indirect tensile strength test configuration for 54 mm diameter with jaws

Figure 5.8. The indirect tensile strength test configuration for 100 mm diameter without jaws

The indirect tensile strength test specimens before and after testing are shown in Figure 5.9.

Figure 5.9. The indirect tensile strength test specimens before and after testing

Results of peak loads and calculated tensile strength values are given in Table 5.3.

Table 5.3. *Results of indirect tensile strength tests*

Specimen	**Diameter (mm)**	**Thickness (mm)**	**Peak Load (kN)**	**Tensile Strength (MPa)**
BT-1	54.7	34.8	27.3	9.1
BT-2	54.6	36.3	29.3	9.8
BT-3	54.7	35.3	32.5	10.4
BT-4	54.6	34.2	23.8	8.1
BT-5	54.6	35.8	29.4	9.5
BT-6	52.70	27.3	15.5	6.9
BT-7	52.74	27.8	17.9	7.8
BT-8	100.75	50.2	63.7	8.0
BT-9	101.03	50.1	63.4	8.0
Average				8.6±1.1

From the data of indirect tensile strength tests, load-displacement curves are drawn. Figure 5.10 shows a typical load-displacement curve for Brazilian tests. All indirect tensile test curves can be seen in Appendix B.

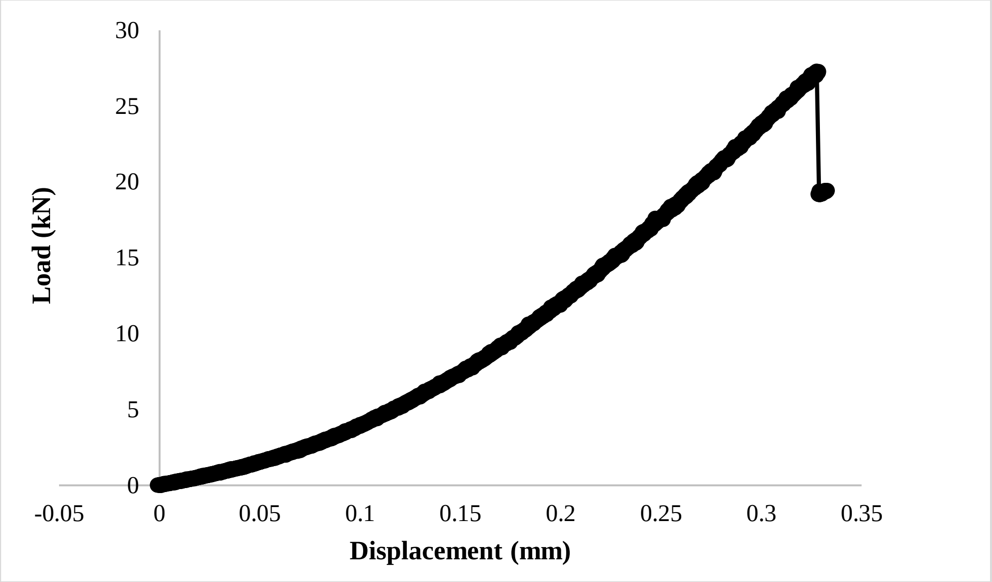

Figure 5.10. Load versus displacement curve for BT-1 specimen

CHAPTER 6

MODE I FRACTURE TOUGHNESS TESTING WITH SNDB AND SCB GEOMETRIES

Circular plate type disk specimen (SNDB) and semi-circular core disk specimen (SCB) were used to assign mode I fracture toughness K_{Ic} of the grey colored Ankara Gölbaşı andesite. After recording the failure loads, fracture toughness of the SNDB and SCB test specimens were calculated for mode I loading state. Totally, 81 fracture toughness tests were performed with SNDB and SCB specimens. Fracture tests were done by servo-hydraulic MTS 815 testing machine. In the tests, the loading was applied on SNDB and SCB specimens by a displacement-controlled way.

6.1. Specimen Preparation for Mode I Fracture Toughness Test

Specimen preparation is important process of the rock fracture tests. Attention to the sample preparation process prevents unwanted irregularities and poor results. Some equipment use for the process of the specimen preparation. Boring machine, milling machine, diamond circular saw, MTS, caliper gage, goniometer and water gage are some of them.

The boring machine was used to core from the large blocks (Figure 6.1). The only 100 mm diameter cores were used in this experimental works.

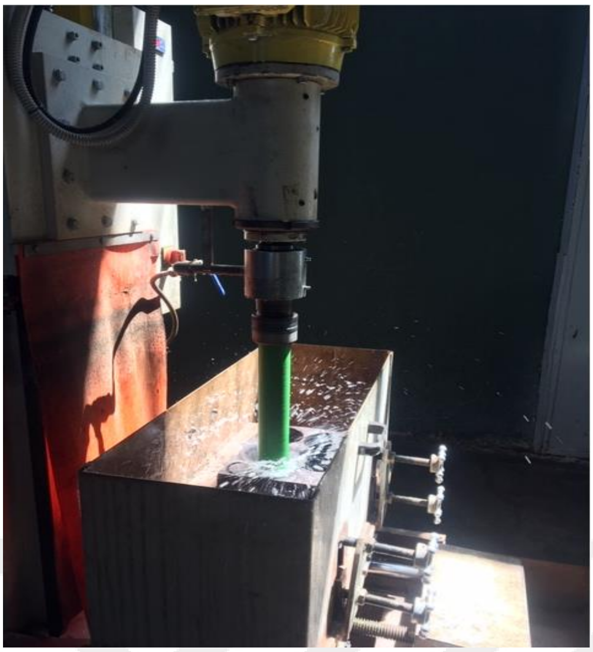

Figure 6.1. Boring machine

Cored specimens were cut discs into different thicknesses which were about 55 mm and 65 mm for SNDB and SCB specimens by using a rotary saw machine (Figure 6.2). Furthermore, the rotary saw machine was used to divide disk specimens to semi-circular disk specimens for the preparation of the SCB specimens.

Figure 6.2. Rotary saw machine

Generally, deflection occurred during the cutting processes with rotary saw machine because the diameter of the rotary saw machine is so large. Milling machine was used to remove this deviation (Figure 6.3). It was used to create more flat surfaces of SNDB and SCB specimens. Diamond impregnated milling cutter were used to reach this aim. Any irregularities of the test specimens cause incorrect results of the fracture toughness tests. So, the process in the milling machine is important for the preparation of the SNDB and SCB test specimens.

Figure 6.3. Milling machine

The diamond circular saw machine was used to open the notch. Notch length was adjusted by a digital caliper. The diamond impregnated circular saw was utilized for notching processes on both SNDB and SCB specimens. The thickness of the diamond impregnated circular saw has 0.5 mm. Figure 6.4 shows the diamond circular saw machine and digital caliper. The notch length was kept fixed as 10 mm for the SNDB and SCB specimens. Unfortunately, there is a deviation value of the diamond circular saw machine. This value is about ±0.2 mm. Thus, the notch value was set the digital caliper 9.9 mm or 10.01 mm to obtain a 10 mm notch length.

The center line was marked on the upper flat surface of the SNDB specimen. SNDB test specimen was put as parallel to the floor of the diamond circular saw machine

(Figure 6.4). SNDB test specimens were fixed with the holding fixture equipment during opening the notching processes.

Figure 6.4. Diamond circular saw machine with SNDB test specimen

The centerline was marked on SCB test specimens. The semi-circular disk was located in a special bowl to keep it fix during the notching process (Figure 6.5).

Figure 6.5. Diamond circular saw machine with SCB test specimen

6.2. Fracture Tests

The fracture toughness tests were conducted by stiff servo-controlled MTS 815 Rock Testing System. SNDB and SCB specimens were located between loading platens. The upper platen has 500kN ± 0.25 load-cell. Disk and semi-circular disk specimens were loaded with displacement-controlled fashion with a two-stage. The controller unit of the FlexTest 40 provides the actuator to act with controlling of displacement. Inıtially, loading was applied to the test specimens with high rate as 0.0005 mm/s This load rate continue till the load limit detector. In second loading stage, loading was applied to the test specimens with low rate as 0.0003 mm/s At the end of the test time, the maximum load was recorded to calculate the fracture toughness.

SNDB and SCB specimens were tested under three-point bending to find the fracture toughness value for mode I. Bending condition was provided by rollers that have 8 mm diameter. One of them was located at the upper surface of the specimen for loading purposes. The other two of them were located at the bottom surface of the specimen for supporting purposes.

6.2.1. Testing Work with SNDB Specimen

In the fracture toughness tests, each core specimen diameter was kept as 100 mm. With SNDB geometry, specimens with two different circular disk thicknesses t= 50 and 60 mm were prepared to be tested. The notch length was kept fixed as 10 mm for all SNDB specimens. Specimens with thicknesses of t/R=1 and t/R=1.2 mm were prepared. Three-point bending loads were applied to the disks with nine different span lengths: S/R= 0.40, 0.45, 0.50, 0.55, 0.60, 0.70, 0.80, 0.85 and 0.90. Totally, 54 fracture tests were done with SNDB specimen geometry. The detail dimensions of the SNDB specimens are given in Appendix C. Figure 6.6 shows the SNDB specimen during fracture toughness testing under three-point bending. The randomly chosen SNDB specimen photos during the test and all specimens after the test can be seen in Appendix D.

Figure 6.6. SNDB specimen configuration

The specimens were labeled to organize the samples and the results of the fracture toughness tests. Specimens were coded in terms of the disk thickness, span length (*S/R*) and specimen number for SNDB testing work.

$$\underbrace{\textbf{SNDB}}_{\text{Straight Notched Disk Bending}} \textbf{–} \underbrace{\textbf{60}}_{\text{Thickness}} \textbf{–} \underbrace{\textbf{040}}_{\text{S/R}} \underbrace{\textbf{-1}}_{\text{Specimen number}}$$

SNDB specimens with 50 mm and 60 mm thickness are shown in Figure 6.7.

Figure 6.7. SNDB specimens with 60 and 50 mm thickness

An example of the mode I fracture toughness (K_{Ic}) calculation was presented for SNDB specimen. To calculate K_{Ic} of the SNDB specimen, stress intensity factor K_I was computed by ABAQUS initially. 100 mm diameter, 60 mm thickness, 40 mm span length and 10 mm crack length was assigned in ABAQUS for SNDB model geometry in this example. After the model was run, computed K_I was found 22.7618 $\mathrm{Pa}\sqrt{\mathrm{m}}$. The dimensionless stress intensity factor Y_I was calculated with Equation 6.1 and 6.2.

$$Y_I = \frac{K_I}{\sigma_0 \sqrt{\pi a}} \qquad (6.1)$$

$$\sigma_0 = (P/2Dt) \qquad (6.2)$$

where;

P= applied load (1N)

D= diameter (0.1 m)

t= thickness (0.06 m)

a= notch length (0.01 m)

$$\sigma_0 = (1/(2 \times 0.1 \times 0.06)$$

$$\sigma_0 = 83.33 \text{ Pa}$$

$$Y_I = \frac{22.76}{83.33\ \sqrt{\pi 0.01}} = 1.54$$

The mode I fracture toughness (K_{Ic}) was calculated with Equation 6.3 and 6.4.

$K_{Ic} = Y_I \sigma_{cr} \sqrt{\pi a}$ (6.3)

$\sigma_{cr} = (P_{cr}/2Dt)$ (6.4)

where;

P_{cr} = load at fracture (64500 N)

D = diameter (100.25 mm)

t = thickness of the specimen (60.30 mm)

a = notch length (0.01 m)

$$\sigma_{cr} = (64500/2 \times 100.25 \times 60.30)$$

$$\sigma_{cr} = 5.33 \text{ MPa}$$

$$K_{Ic} = 1.54 \times 5.33 \times \sqrt{\pi 0.01} = 1.46 \text{ MPa}\sqrt{\text{m}}$$

All fracture test results for SNDB specimens with 50 mm and 60 mm thickness are given in Table 6.1 and 6.2.

Table 6.1. *SNDB fracture test results for t=50 mm*

Specimen Code	**Fracture Load**	**Mode I Fracture Toughness (K_{Ic})**	**Avg. Mode I Fracture Toughness (K_{Ic})**
	kN	$\mathbf{MPa\sqrt{m}}$	$\mathbf{MPa\sqrt{m}}$
SNDB-50-040-1	35.65	1.20	1.29
SNDB-50-040-2	35.90	1.21	
SNDB-50-040-3	43.63	1.47	
SNDB-50-045-1	30.28	1.20	1.27
SNDB-50-045-2	26.48	1.06	
SNDB-50-045-3	35.42	1.41	
SNDB-50-045-4	36.20	1.44	
SNDB-50-050-1	27.86	1.26	1.25
SNDB-50-050-2	28.93	1.31	
SNDB-50-050-3	26.27	1.19	
SNDB-50-055-1	20.32	1.04	1.23
SNDB-50-055-2	23.57	1.21	
SNDB-50-055-3	27.80	1.43	
SNDB-50-060-1	20.54	1.14	1.22
SNDB-50-060-2	20.93	1.16	
SNDB-50-060-3	24.28	1.35	
SNDB-50-070-1	19.23	1.30	1.21
SNDB-50-070-2	17.50	1.18	
SNDB-50-070-3	16.86	1.14	
SNDB-50-080-1	15.34	1.19	1.20
SNDB-50-080-2	14.32	1.12	
SNDB-50-080-3	16.58	1.28	
SNDB-50-085-1	14.80	1.23	1.19
SNDB-50-085-2	15.33	1.27	
SNDB-50-085-3	12.95	1.08	
SNDB-50-090-1	14.20	1.25	1.18
SNDB-50-090-2	13.69	1.21	
SNDB-50-090-3	12.17	1.08	
Average ± STD	23.11±8.66	1.23±0.11	

According to Table 6.1, average mode I fracture toughness (K_{Ic}) of SNDB specimen with 50 mm thickness was found as 1.23±0.11 $\mathrm{MPa\sqrt{m}}$.

Table 6.2. *SNDB fracture test results for t=60 mm*

Specimen Code	**Fracture Load**	**Mode I Fracture Toughness (K_{Ic})**	**Avg. Mode I Fracture Toughness (K_{Ic})**
	kN	$\mathbf{MPa\sqrt{m}}$	$\mathbf{MPa\sqrt{m}}$
SNDB-60-040-1	64.50	1.46	1.52
SNDB-60-040-2	63.89	1.45	
SNDB-60-040-3	73.46	1.66	
SNDB-60-045-1	62.35	1.72	1.50
SNDB-60-045-2	59.46	1.64	
SNDB-60-045-3	41.19	1.14	
SNDB-60-050-1	47.64	1.53	1.48
SNDB-60-050-2	45.05	1.45	
SNDB-60-050-3	45.93	1.47	
SNDB-60-055-1	41.91	1.52	1.45
SNDB-60-055-2	38.01	1.37	
SNDB-60-055-3	40.49	1.47	
SNDB-60-060-1	29.63	1.20	1.41
SNDB-60-060-2	39.83	1.60	
SNDB-60-060-3	35.69	1.44	
SNDB-60-070-1	24.16	1.16	1.32
SNDB-60-070-2	30.89	1.49	
SNDB-60-070-3	27.39	1.32	
SNDB-60-080-1	18.54	1.04	1.27
SNDB-60-080-2	28.06	1.56	
SNDB-60-080-3	26.94	1.50	
SNDB-60-080-4	17.50	0.98	
SNDB-60-085-1	21.56	1.28	1.25
SNDB-60-085-2	20.72	1.24	
SNDB-60-085-3	20.62	1.22	
SNDB-60-090-1	19.02	1.21	1.21
Average ± STD	37.86±16.25	1.39±0.19	

According to Table 6.2, average mode I fracture toughness (K_{Ic}) of SNDB specimen with 60 mm thickness was found as 1.39±0.19 $\mathrm{MPa\sqrt{m}}$.

6.2.2. Testing Work with SCB Specimen

The fracture tests with SCB geometry which has 50 mm thickness were performed to be tested. The notch length was kept fixed as 10 mm for all SCB specimens. Specimens thickness of *t/R*=1 were prepared with nine different span lengths *S/R*= 0.40, 0.45, 0.50, 0.55, 0.60, 0.70, 0.80, 0.85 and 0.90. Totally, 27 fracture tests were done with SNDB specimen geometry. The detail dimensions of the SNDB specimens are given in Appendix C. Figure 6.8 shows the SCB specimen during fracture toughness testing under three-point bending. The randomly chosen SCB specimen photos during the test and all specimens after the test can be seen in Appendix D.

Figure 6.8. SCB specimen configuration

The specimens were labeled to organize the samples and results of the fracture tests. The specimens were coded in terms of the thickness, span length (S/R) and specimen number for SCB.

$$\underbrace{\textbf{SCB}}_{\text{Semi-Circular Bend}} - \underbrace{\textbf{50}}_{\text{Thickness}} - \underbrace{\textbf{040}}_{\text{S/R}} \textbf{-}\underbrace{\textbf{1}}_{\text{Specimen number}}$$

One example of the SCB specimen after the testing work is shown in Figure 6.9.

Figure 6.9. SCB specimen

An example of the mode I fracture toughness (K_{Ic}) calculation was presented for SCB specimen. To calculate K_{Ic} of the SCB specimen, stress intensity factor (K_I) was computed by ABAQUS initially. 100 mm diameter, 50 mm thickness, 40 mm span length and 10 mm crack length was assigned in ABAQUS for SCB model geometry in this example. After the model was run, computed K_I was found 64.4761 Pa$\sqrt{\mathrm{m}}$. The dimensionless stress intensity factor (Y_I) was calculated with Equation 6.5 and 6.6.

$$Y_I = \frac{K_I}{\sigma_0 \sqrt{\pi a}} \qquad (6.5)$$

$$\sigma_0 = (P/2Rt) \qquad (6.6)$$

where;

P = applied load (1 N)

R = radius (0.05 m)

t = thickness (0.05 m)

a = notch length (0.01 m)

$$\sigma_0 = (1/(2 \times 0.05 \times 0.05)$$

$$\sigma_0 = 200 \text{ Pa}$$

$$Y_I = \frac{64.48}{200\sqrt{\pi 0.01}} = 1.82$$

The mode I fracture toughness (K_{Ic}) was calculated with Equation 6.7 and 6.8.

$K_{Ic} = Y_I \sigma_{cr} \sqrt{\pi a}$ (6.7)

$\sigma_{cr} = (P_{cr}/2Dt)$ (6.8)

where;

P_{cr} = load at fracture (18530 N)

R= radius (50.33 mm)

t= thickness of the specimen (50.30 mm)

a= notch length (0.01 m)

$$\sigma_{cr} = (18530/2 \times 50.33 \times 50.30)$$

$$\sigma_{cr} = 3.66 \text{ MPa}$$

$$K_{Ic} = 1.82 \times 3.66 \times \sqrt{\pi 0.01} = 1.18 \text{ MPa}\sqrt{\text{m}}$$

All fracture test results for specimens with 50 mm thickness are given in Table 6.3.

Table 6.3. *SCB fracture test results for t=50 mm*

Specimen Code	**Fracture Load**	**Mode I Fracture Toughness** (K_{Ic})	**Avg. Mode I Fracture Toughness** (K_{Ic})
	kN	$\mathbf{MPa\sqrt{m}}$	$\mathbf{MPa\sqrt{m}}$
SCB-50-040-1	19.34	1.24	1.20
SCB-50-040-2	18.53	1.18	
SCB-50-040-3	18.31	1.17	
SCB-50-045-1	13.34	1.03	1.04
SCB-50-045-2	13.20	1.02	
SCB-50-045-3	13.90	1.07	
SCB-50-050-1	11.19	1.00	1.03
SCB-50-050-2	11.01	0.98	
SCB-50-050-3	12.54	1.12	
SCB-50-055-1	12.24	1.24	0.96
SCB-50-055-2	6.52	0.66	
SCB-50-055-3	9.73	0.99	
SCB-50-060-1	6.86	0.78	0.90
SCB-50-060-2	7.10	0.81	
SCB-50-060-3	9.65	1.10	
SCB-50-070-1	5.09	0.70	0.88
SCB-50-070-2	6.84	0.94	
SCB-50-070-3	7.18	0.99	
SCB-50-080-1	4.29	0.70	0.80
SCB-50-080-2	4.57	0.74	
SCB-50-080-3	5.98	0.97	
SCB-50-085-1	4.90	0.86	0.79
SCB-50-085-2	3.92	0.69	
SCB-50-085-3	4.64	0.81	
SCB-50-090-1	2.91	0.55	0.73
SCB-50-090-2	4.14	0.78	
SCB-50-090-3	4.62	0.87	
Average ± STD	8.98±4.83	0.93±0.19	

According to Table 6.3, average mode I fracture toughness (K_{Ic}) of SCB specimen was found as 0.93±0.19 $\mathrm{MPa\sqrt{m}}$.

CHAPTER 7

RESULTS AND DISCUSSION

The effect of the size and loading span on K_{Ic} was observed for the tests using SNDB specimen geometry under three-point bending loads. Effect of span length on K_{Ic} for the tests using well-recognized SCB geometry under three-point bending was clearly identified in the laboratory work effort. The aim is to see that the span length effect for another similar geometry and compare the results. Varying span lengths had an important effect on the mode I fracture toughness. Increasing the specimen thickness had an effect on K_{Ic} which was the specimen size effect on mode I fracture toughness. The results of the tests with the two specimen geometries yielded different mode I fracture toughness. To explain this phenomenon, stress analyses were conducted on numerical models of SNDB and SCB test geometries. Average loads from the experiments were applied to the SNDB and SCB model geometries to comparatively analyze the extent of the plastic region under mode I loading condition. Stress analysis was performed along the paths ahead of the crack tip in the models.

7.1. Analysis of the Fracture Toughness Tests Results

Average K_{Ic} results from all of the fracture test results are plotted against span in Figure 7.1. Spans vary from S/R= 0.40 to 0.90 in the Figure 7.1. Each average data point there corresponds to the average of three tests with the particular geometry. Fitted curves are attached to the data points in Figure 7.1.

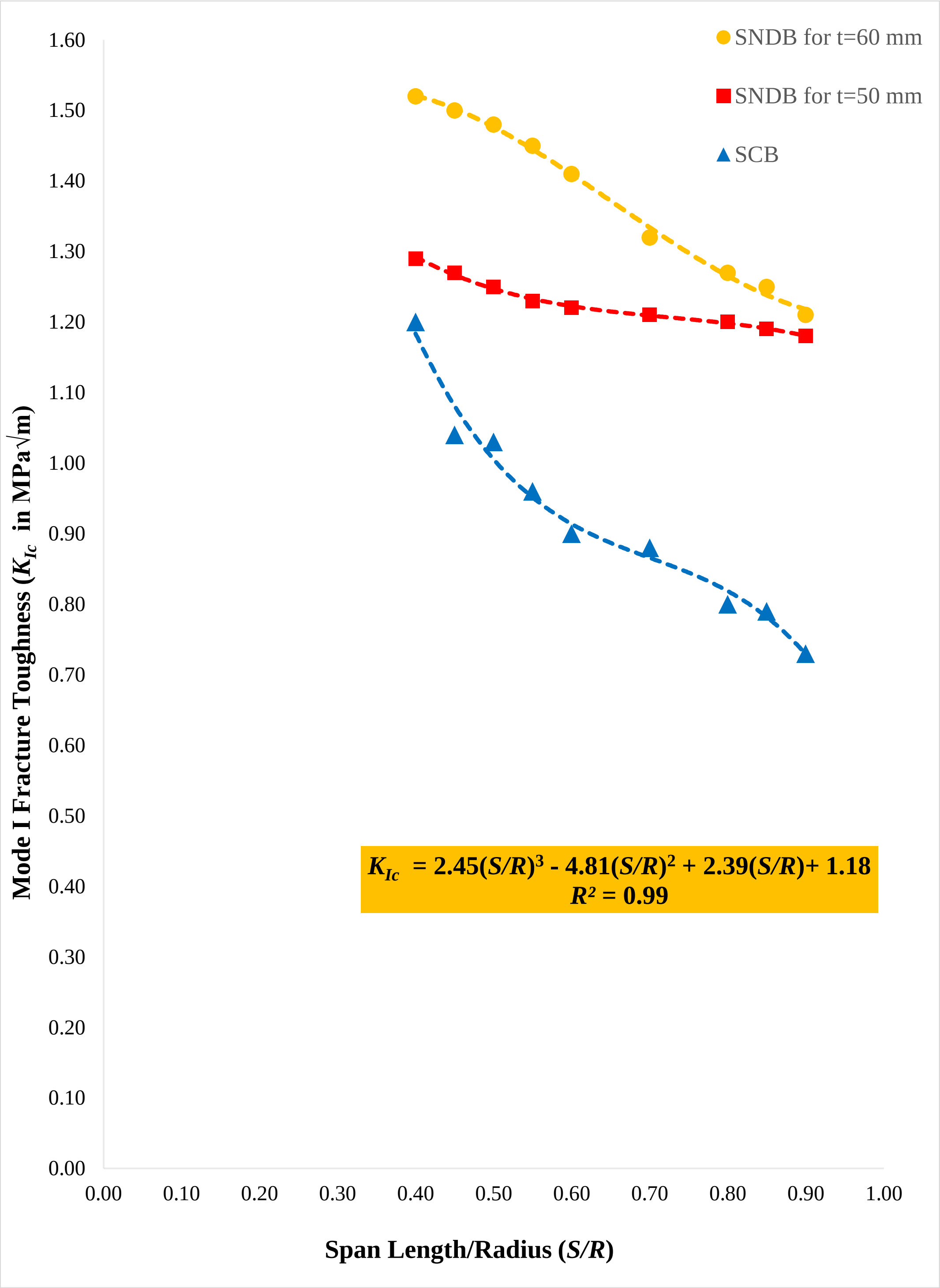

Figure 7.1. Average facture toughness versus *S/R* for SNDB and SCB specimen geometries

Fitted cubic polynomial for SNDB data of t=60 mm disk geometry has a good fitting quality with R^2=0.99 as seen in the Figure 7.1. For SNDB data with thickness 50 mm and for SCB data, cubic polynomial curves are the best fits with correlation coefficients around 0.99.

The measured fracture toughness changes with the thickness of the SNDB specimen. Average mode I fracture toughness of all SNDB tests with thicknesses of 60 and 50 mm were 1.39±0.19 $MPa\sqrt{m}$ and 1.23±0.11 $MPa\sqrt{m}$, respectively. K_{Ic} of the SNDB specimen for t=60 mm is about 13% higher than K_{Ic} of the SNDB specimen for t=50 mm. The fracture tests could not be conducted with disks having larger thickness than 60 mm, since crushing was observed underneath the rollers contacting and loading the specimens. The high stress concentration under line load caused crushing. Another observation in Figure 7.1 is that K_{Ic} difference for 60 mm and 50 mm disk tests gets larger for smaller spans such as S/R=0.40.

Effect of the loading span on K_{Ic} for tests with both SNDB and SCB geometries is clearly observed in overall results. Among all tests, the highest average K_{Ic} is 1.52 $MPa\sqrt{m}$ for 60 mm thick SNDB specimen geometry with the smallest span of S/R=0.40. For this thickness group, the lowest value is 1.21 $MPa\sqrt{m}$ for tests with span of S/R=0.90. For t=50 mm group, the highest average K_{Ic} is 1.29 $MPa\sqrt{m}$ again for the smallest span represented by S/R=0.40. With span of S/R=0.90, the lowest value is 1.18 $MPa\sqrt{m}$ for 50 mm thickness group,

K_{Ic} of the SNDB specimen with t=60 mm decreases by about 26% when span is increased from S/R=0.40 to 0.90. The K_{Ic} of the SNDB specimen for t=50 mm decreases by about 10% when span is increased from S/R=0.40 to 0.90.

Average mode I fracture toughness value for all SCB specimens is obtained as 0.93±0.19 $MPa\sqrt{m}$, regardless of span. The average K_{Ic} measured by the SCB tests is about 50% lower than the average of all SNDB tests with 60 mm thickness, regardless of span. The average K_{Ic} measured by the SCB tests is about 32% lower than the average of all SNDB tests with 50 mm thickness.

Regarding the variation of K_{Ic} with span, a similar but stronger effect is observed for the tests with well-known SCB geometry. Among all SCB tests, the highest average K_{Ic} is 1.20 $MPa\sqrt{m}$. For SCB tests, the lowest average value is 0.73 $MPa\sqrt{m}$. According to this, K_{Ic} of the SCB decreases by around 64% when span length is increased from S/R=0.40 to 0.90.

In summary, increasing the thickness of the SNDB disk specimen geometry is clearly identified; K_{Ic} increases with disk thickness. This increase is much higher for the tests with lower S/R of three-point bending load configuration. For larger S/R, the beam effect gets more dominant resulting in more bending action and lower K_{Ic} values. For SCB results, the same trend exists in a stronger fashion. Another important finding that SCB results are definitely lower than the results of SNDB tests. This can be due to the fact that SCB geometry is more susceptible to beam-like action compared to SNDB geometry under three-point bending with a low span.

According to Figure 7.1, the data points around the trend curve of SCB tests show larger variations. The deviation of data points is higher than those of SNDB tests. Hence, the curve and the trend line fits better in the results of SNDB tests.

Polynomial function of third degree results as the best fit between mode I fracture toughness (K_{Ic}) and span length (S/R) for 60 mm thick SNDB specimens in Figure 7.1. The average maximum and minimum K_{Ic} can be obtained by using first derivative test. A second degree polynomial function is obtained after taking the first derivative of the polynomial function of degree three. The two different critical points are acquired from the first derivative operation. These critical points are at S/R=0.33 and 0.98.

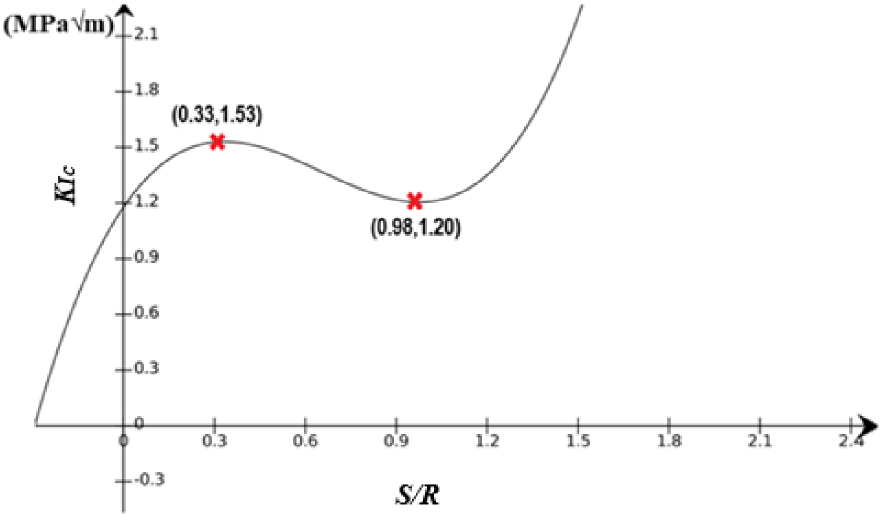

Figure 7.2. Graph of the fitted function

The polynomial of degree three for the test results of 60 mm thick SNDB specimen test has a maximum value 1.53 $MPa\sqrt{m}$ at the point *S/R*=0.33 and has a minimum value 1.20 $MPa\sqrt{m}$ at the point *S/R*=0.98 (Figure 7.2). The average maximum and minimum K_{Ic} obtained from both SNDB tests and polynomial of degree three are quite similar. It is interesting to note that average minimum value of K_{Ic} =1.20 $MPa\sqrt{m}$ is exactly equal to the SCB test data point for the lowest span of *S/R*=0.40.

Considering the high quality of the tests, the results, and the fitted trend curves, it can be claimed that the mode I fracture toughness from a three-point bend test approaches to the identified maximum which is K_{Ic} =1.53. As reported in the literature section, SCB testing method is commonly preferred by the researchers due to the its simplicity in specimen preparation and easiness of testing procedure. However, as found here, it suffers too much from beam-like bending action. It is suggested that to find a K_{Ic} which is effected minimum from bending action SCB testing should be carried out with a loading configuration having *S/R*=0.40 or less, and the result must be corrected with the factor found as for SNDB geometry with *t*=60 mm.

In literature, span over radius (*S/R*) changed between 0.50 and 0.80 SCB method. ISRM suggested a range for SCB test as $0.50 \leq S/R \leq 0.80$ (ISRM, 2007). As a contribution here, successful results for both SNDB and SCB tests are provided for specimens under three-point bending load with $S/R=0.40$. For a span of $S/R=0.40$:

$$K_{Ic\,(SNDB)}=1.27\,K_{Ic\,(SCB)} \qquad (7.1)$$

7.2. Stress Analyses of the SNDB and SCB Specimen

To investigate the plastic zone or so-called fracture process zone (FPZ), stress analyses are conducted along the paths at the notches of SNDB (straight notched disk bending) and SCB (semi-circular bending) geometries. Paths covering sufficient number of finite elements ahead of the seam crack are assigned to some ABAQUS models. The selected SNDB and SCB models have the same loading configuration with $S/R=0.90$. For SNDB geometry, two models with $t/R=1.0$ and $t/R=1.2$ are chosen for the analysis.

The reason for choosing a large span represented as $S/R=0.90$ is to proceed with a geometry which exaggerates the beam bending action.

Average loads from the experiments are 19.02 kN for 60 mm thickness SNDB specimen, 13.35 kN for 50 mm thickness SNDB specimen and 3.89 kN for SCB specimen, all having span of S/R=0.90. These average loads are applied to the SNDB and SCB models to simulate and generate the real stress fields of the particular tests. Purpose is estimate and compare the extent of the plastic region for the three cases in consideration.

The stress path covering the contour integral region ahead of the crack tip is shown in Figure 7.3.

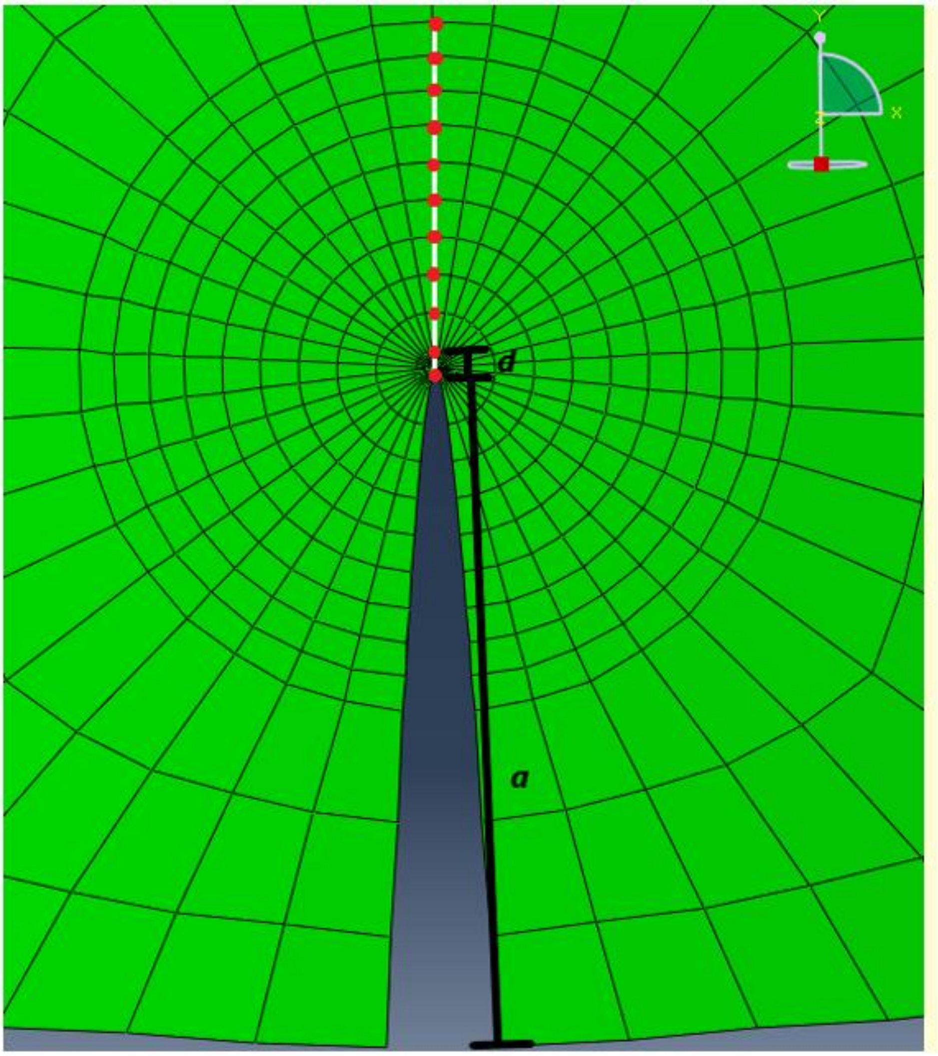

Figure 7.3. Stress path for mode I loading

σ_{xx} stress is the main stress component leading to the crack opening and propagation. Stress contours perpendicular to the front of the seam crack (σ_{xx}) are plotted for SNDB and SCB model geometries, (Figure 7.4). Stress concentration at the crack tip is more intense for SCB model geometry. The least intense stress concentration is observed for SNDB geometry of 60 mm thickness.

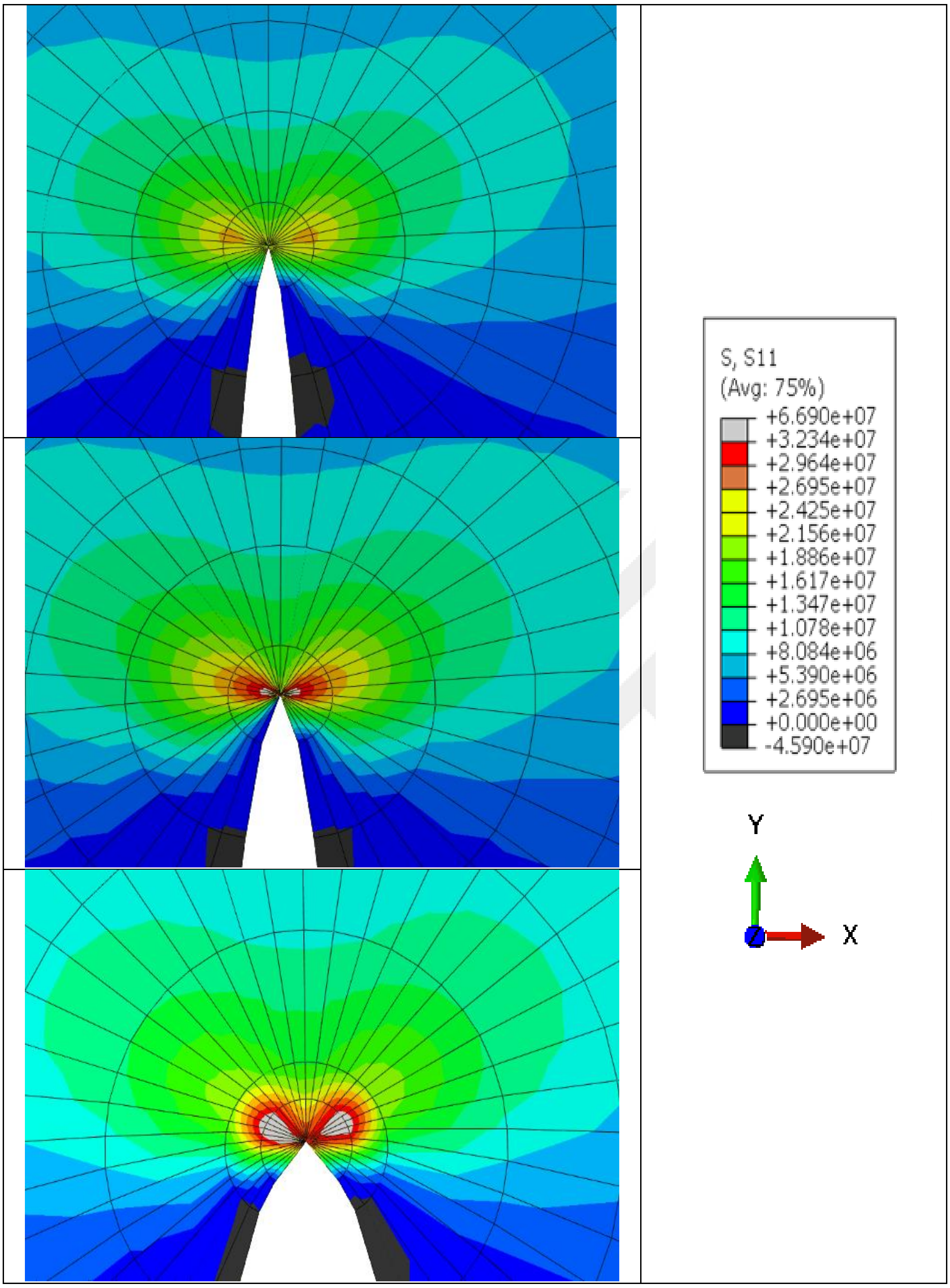

Figure 7.4. σ_{xx} stress contours for *t*=60 mm SNDB, *t*=50 mm SNDB and SCB near the crack tip

Values of σ_{xx} for SNDB and SCB model geometries are given in Table 7.1. First column is the ratio of the true distance along the path and crack length which is represented as *d/a*. σ_{xx} of the SCB model geometries are higher than the σ_{xx} of the SNDB model geometries. σ_{xx} decreases with increasing thickness of SNDB model geometries.

Table 7.1. σ_{xx} *for SNDB model with 60 mm and 50 mm thickness and SCB model*

(*d/a*)	**σ_{xx} of the SNDB *t*=60 mm**	**σ_{xx} of the SNDB *t*=50 mm**	**σ_{xx} of the SCB**
	MPa	**MPa**	**MPa**
0.00	23.52	24.75	30.63
0.03	15.31	16.16	16.69
0.08	9.56	10.10	10.94
0.13	6.82	7.23	7.42
0.19	5.37	5.72	6.09
0.24	4.44	4.73	5.22
0.30	3.76	4.03	4.62
0.35	3.25	3.48	3.78
0.40	2.85	3.11	3.35
0.45	2.56	2.73	3.38
0.50	2.17	2.30	2.95

σ_{xx} versus *d/a* is plotted for all three specimen geometries in Figure 7.5. In the figure, individually fitted curves for SCB and two SNDB cases are marked and the related equations are given. Tensile strength threshold is marked as T_0 and used to calculate the extent of possible tensile yield zone or so-called process zone. The extent of the yielded zone is traditionally symbolized as r_y.

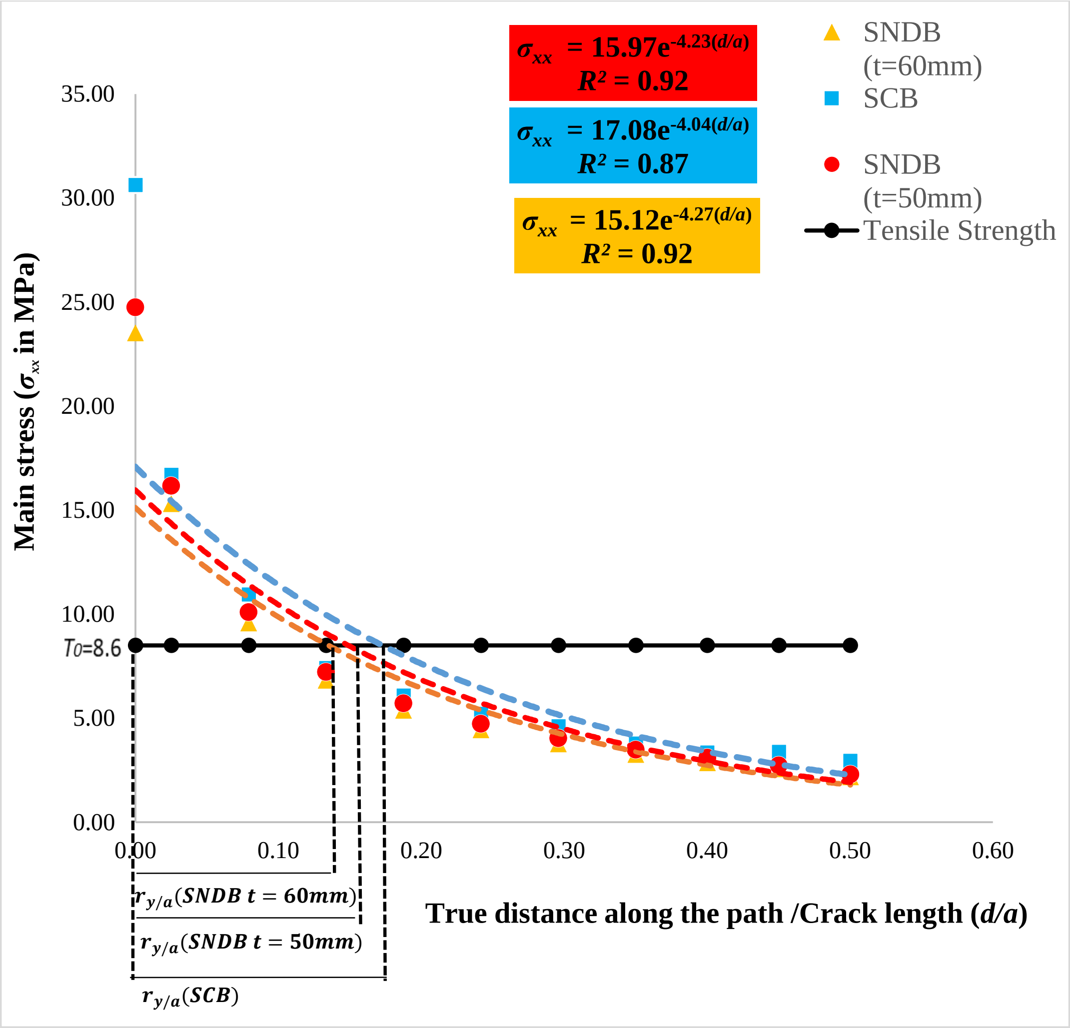

Figure 7.5. σ_{xx} stress along SNDB and SCB models stress path

As can be seen in Figure 7.5, the horizontal stress curves go to infinity at the crack tip. These curves are intersected by the value of the tensile strength (T_0) which is 8.6±1.1 MPa found from indirect tensile strength tests. To estimate the size of a possible plastic or yield zone ahead of the crack tip, the following calculation steps are presented as an example:

$$\sigma_{xx} = T_0 = 15.12e^{-4.27(d/a)}$$

where;

d/a = yield parts

r_y = yielded zone size or extent

$$8.6 = 15.12e^{-4.27(d/a)}$$

$$r_{y/a} = d/a = 0.132$$

The extent for SNDB specimens which has 60 mm thickness and 50 mm thickness are found as $r_{y/a}$ =0.132 and $r_{y/a}$ =0.146 respectively. The calculated extent for SCB model was $r_{y/a}$ =0.170. Extent of the possible plastic zone for 60 mm thickness SNDB specimen is around 11% lower than SNDB specimen with 50 mm thickness. The extent of the yield zone at the crack tip become narrow with increasing specimen thickness of SNDB specimens.

The extent of the possible plastic zone of the SCB specimen is around 29% higher than SNDB specimen of 60 mm thickness under tensile mode I loading. The extent of the plastic region of the SCB specimen is around 17% higher than the extent of the plastic zone for 50 mm thick SNDB specimen geometry.

CHAPTER 8

CONCLUSIONS AND RECOMMENDATIONS

Straight notched disk bending (SNDB) mode I fracture toughness testing method was preferred due to simplicity of core-based specimen preparation and flexibility to adjust disk specimen thickness for analyzing size effect on the toughness. Span lengths of three-point loading configuration could be varied and optimum span could be found to reach consistent results for mode I fracture toughness. Another three-point bend test, so called semi- circular bending (SCB) test was the choice for comparison purposes.

A verification problem of the three-point bending plate was modeled in ABAQUS. Results were compared to the analytical solution. Accuracy of the results from the modeling work was around 2% in this verification problem.

Another verification example was the modeling of well-known SCB specimen geometry under three-point bending. The modeling procedure and work were verified by modeling SCB geometries and comparing the SIF results available the previous work. The results were compatible within differences around 1%.

In results of the numerical modeling, one observation is that the dimensionless mode I SIF (Y_I) of the SNDB decreases with increasing thickness. Y_I of the SNDB and SCB geometries increases with increasing span length (from S/R=0.40 to S/R=0.90). A linear relation between Y_I and S/R for both SNDB and SCB geometries is found to be the best fit.

One significant finding is that overall average K_{Ic} of the SNDB decreases around 13% (from 1.39 MPa$\sqrt{\text{m}}$ to 1.23 MPa$\sqrt{\text{m}}$) as the specimen thickness decreases.

K_{Ic} of the SNDB specimen for t=60 mm decreases by around 26% (from 1.52 MPa$\sqrt{\mathrm{m}}$ to 1.21 MPa$\sqrt{\mathrm{m}}$) with increasing span (from S/R=0.40 to 0.90). The K_{Ic} of the SNDB specimen for t=50 mm decreases by around 10% (from 1.29 MPa$\sqrt{\mathrm{m}}$ to 1.18 MPa$\sqrt{\mathrm{m}}$) with increasing span (from S/R=0.40 to 0.90).

The effect of the model geometry on K_{Ic} is obvious. The average K_{Ic} of the SCB tests (0.93 MPa$\sqrt{\mathrm{m}}$) is about 50% lower than the average of all SNDB tests with t=60 mm (1.39 MPa$\sqrt{\mathrm{m}}$). The average K_{Ic} of the SCB tests is about 32% lower than the average of all SNDB tests with t=50 mm (1.23 MPa$\sqrt{\mathrm{m}}$).

The effect of the changing span length is observed on well-known SCB geometry strongly. K_{Ic} of the SCB decreases by around 64% (from 1.20 MPa$\sqrt{\mathrm{m}}$ to 0.73 MPa$\sqrt{\mathrm{m}}$) with increasing span length (from S/R=0.40 to 0.90). The K_{Ic} decreasing trend of the SCB geometry with span length is seen to be stronger than SNDB geometry.

One original contribution is that in addition to the S/R ratios commonly used in the previous works, the fracture toughness tests were performed with S/R=0.40 for the first time. Successful results were obtained without crushing the beam samples under the loading and support rollers.

It was concluded that the beam effect increases with the increasing S/R due to the more bending action. Hence, the value of the mode I fracture toughness decreased. The beam effect on the SCB geometry under the three-point bending loading condition was found to be stronger than the SNDB geometry.

The stress analysis was done on the SNDB and SCB geometries to predict the extent of the possible plastic zone at the crack tip under a three-point bending loading condition. The extent of the plastic zone of the SNDB specimen with t=60 mm is around 11% lower than SNDB specimen with t=50 mm. The extent of the plastic zone of the SCB specimen is around 29% and 17% higher than the SNDB specimen geometries with 60 mm and 50 mm thicknesses, respectively.

Some recommendations for future work are listed as;

- These results will be useful in minimizing fracture process zone (FPZ) for new testing techniques.
- These results can be used to estimate the tensile stresses and beam action for a proper design of the bolt mechanisms based on fracture mechanics. Beam action is reduced by decreasing tensile stresses in bolting.
- Shotcrete is a major supporting unit for tunnel constructions, underground openings in mining applications and many other areas. Cracking of shotcrete is caused by beam action. Furthermore, shrinkage of the shotcrete results in tensile loading leading to the propagation of cracks. These results will be useful to predict the life expectancy of shotcrete due to the early-age shrinkage cracking. The beam type specimen geometries under three-point bend loading can be used to estimate the fracture behavior of the shotcrete.
- The effects of the different notch lengths on mode I fracture toughness can be investigated.
- Process of the specimen preparation should be done carefully. Especially, flatness and paralleling of the specimen surfaces are very important for accuracy of the results of the fracture tests.
- Specimen diameter (*D*) can be varied to investigate the effect on fracture toughness in mode I.
- The effect of thickness and span length and specimen geometry on the mode I fracture toughness can be investigated for the rock types with different characteristics.

REFERENCES

ABAQUS/CAE User’s Manual, Version 6.12 Documentation

Anderson, T. L. (1991). Fracture mechanics-fundamentals and applications. NASA STI/Recon Technical Report A, 92.

Anderson, T. L. (2017). Fracture mechanics: fundamentals and applications. CRC press.

Atkinson, B. K. (Ed.). (2015). Fracture mechanics of rock. Elsevier.

Backers T., “Fracture Toughness Determination and Micromechanics of Rock Under Mode I and Mode II Loading”, PhD. Doctoral Thesis, University of Potsdam, Germany, 95 p., 2004.

Barenblatt, G.I., ‘‘The Mathematical Theory of Equilibrium Cracks in Brittle Fracture.” Advances in Applied Mechanics, Vol. VII, Academic Press, 1962, pp. 55–129.

Barker, L. M. (1977). A simplified method for measuring plane strain fracture toughness. Engineering Fracture Mechanics, 9(2), 361-369.

Bearman, R. A., Briggs, C. A., & Kojovic, T. (1997). The applications of rock mechanics parameters to the prediction of comminution behaviour. Minerals Engineering, 10(3), 255-264.

Brideau, M. A., Yan, M., & Stead, D. (2009). The role of tectonic damage and brittle rock fracture in the development of large rock slope failures. Geomorphology, 103(1), 30-49.

Broek, D. (2012). Elementary engineering fracture mechanics. Springer Science & Business Media

Chang, K. H. (2013). Product Manufacturing and Cost Estimating Using CAD/CAE: The Computer Aided Engineering Design Series. Academic Press.

Chang, S. H., Lee, C. I., & Jeon, S. (2002). Measurement of rock fracture toughness under modes I and II and mixed-mode conditions by using disc-type specimens. Engineering geology, 66(1-2), 79-97.

Chiaia, B. (2001). Fracture mechanisms induced in a brittle material by a hard cutting indenter. International Journal of Solids and structures, 38(44-45), 7747-7768.

Chong, K. P., Kuruppu, M. D., & Kuszmaul, J. S. (1987). Fracture toughness determination of layered materials. Engineering fracture mechanics, 28(1), 43-54.

Chong, K., & Kuruppu, M. D. (1984). New specimen for fracture toughness determination for rock and other materials. International Journal of Fracture, 26(2), R59-R62.

Cook, R. B. (2005). Non-invasively assessed skeletal bone status and its relationship to the biomechanical properties and condition of cancellous bone.

Donovan, J. G. (2003). Fracture toughness based models for the prediction of power consumption, product size, and capacity of jaw crushers (Doctoral dissertation, Virginia Tech).

Donovan, J. G., & Karfakis, M. G. (2004). Adaptation of a simple wedge test for the rapid determination of mode I fracture toughness and the assessment of relative fracture resistance. International journal of rock mechanics and mining sciences, 4(41), 695-701.

Dugdale, D.S., ‘‘Yielding in Steel Sheets Containing Slits.” Journal of the Mechanics and Physics of Solids, Vol. 8, 1960, pp. 100–104.

Elghazel, A., Taktak, R., & Bouaziz, J. (2016). Investigation of Mechanical Behaviour of a Bioceramic. In Fracture Mechanics-Properties, Patterns and Behaviours. InTech.

Fowell, R. J., Hudson, J. A., Xu, C., & Zhao, X. (1995). Suggested method for determining mode I fracture toughness using cracked chevron notched Brazilian disc (CCNBD) specimens. In International Journal of Rock Mechanics and Mining Sciences and Geomechanics Abstracts (Vol. 7, No. 32, p. 322A).

Franklin, J. A., ZONGQI, S., Atkinson, B. K., Meredith, P. C., Rummel, F., Mueller, W., ... & Bobrov, G. F. (1988). Suggested methods for determining the fracture toughness of rock. International Journal of Rock Mechanics and Mining & Geomechanics Abstracts, 25(2).

Frash, L. P. (2014). Laboratory-scale study of hydraulic fracturing in heterogeneous media for enhanced geothermal systems and general well stimulation (Doctoral dissertation, Colorado School of Mines. Arthur Lakes Library).

Ghamgosar, M., & Erarslan, N. (2015,). A Numerical Study on Oscillating Disc Cutting (ODC) Technology for Hard Rock Cutting. In 13th ISRM International Congress of Rock Mechanics. International Society for Rock Mechanics and Rock Engineering.

Hadei, M. R., Kemeny, J., Ghazvinian, A., Rezaiepoor, A., & Sarfarazi, V. (2017). New Development to Measure Mode I. Fracture Toughness in Rock. Periodica Polytechnica Civil Engineering, 61(1), 51-55.

ISRM (2007) The complete ISRM suggested methods for rock characterization, testing and monitoring: 1974–2006. In: Ulusay R, Hudson JA (eds) Suggested methods prepared by the commission on testing methods. International Society for Rock Mechanics, Compilation Arranged by the ISRM Turkish National Group, Ankara, Turkey

Jones, R., Molent, L., & Pitt, S. (1999). Study of multi-site damage of fuselage lap joints. Theoretical and applied fracture mechanics, 32(2), 81-100.

Khan, K., & Al-Shayea, N. A. (2000). Effect of specimen geometry and testing method on mixed mode I–II fracture toughness of a limestone rock from Saudi Arabia. Rock mechanics and rock engineering, 33(3), 179-206.

Kuruppu MD, Obara Y, Ayatollahi MR, Chong KP, Funatsu T (2014) ISRM-suggested method for determining the mode I static fracture toughness using semi-circular bend specimen. Rock Mech Rock Eng 47(1):267–274

Kuruppu, M. D. (1997). Fracture toughness measurement using chevron notched semi-circular bend specimen. International journal of fracture, 86(4), L33-L38.

Lim, I. L., Johnston, I. W., & Choi, S. K. (1993). Stress intensity factors for semi-circular specimens under three-point bending. Engineering Fracture Mechanics, 44(3), 363-382.

Lim, I. L., Johnston, I. W., & Choi, S. K. (1994, June). Assessment of mixed-mode fracture toughness testing methods for rock. In International journal of rock mechanics and mining sciences & geomechanics abstracts (Vol. 31, No. 3, pp. 265-272). Pergamon.

Marasteanu, M. O., Li, X., Clyne, T. R., Voller, V., Timm, D. H., & Newcomb, D. (2004). Low temperature cracking of asphalt concrete pavement.

Mueller, H. J. (1991). Fracture toughness and fractography of dental ceramics. Cells and Materials, 1(3), 7.

Ouchterlony, F. (1981). Extension of the compliance and stress intensity formulas for the single edge crack round bar in bending. In Fracture Mechanics for Ceramics, Rocks, and Concrete. ASTM International.

Pour, P. H., Aliha, M. R. M., & Keymanesh, M. R. (2018). Evaluating mode I fracture resistance in asphalt mixtures using edge notched disc bend ENDB specimen with different geometrical and environmental conditions. Engineering Fracture Mechanics, 190, 245-258.

Retrieved November 25, 2019, from Metallurgy & Materials Engineering website: metallurgyandmaterials.wordpress.com/2015/12/25 /liberty-ship-failures

Retrieved November 25, 2019, website: www.aerotime.aero/yulius.yoma/18542-history-hour-aloha-airlines-flight-243-incident

Rice, J.R., 1968. A path independent integral and the approximate analysis of strain concentration by notches and cracks. Journal of Applied Mechanics 35, 379e386.

Rossmanith, H. P., Daehnke, A., Nasmillner, R. E. K., Kouzniak, N., Ohtsu, M., & Uenishi, K. (1997). Fracture mechanics applications to drilling and blasting. Fatigue & Fracture of Engineering Materials & Structures, 20(11), 1617-1636.

Roylance, D. (2001). Introduction to fracture mechanics. Massachusetts Institute of Technology, Cambridge, 1.

Rummel, F. (1987). FRACTURE MECHANICS APPROACH TO HYDRAUL| C FRACTURING STRESS MEASUREMENTS. Fracture mechanics of rock, 217.

Singh, R. N., & Sun, G. (1990). A numerical and experimental investigation for determining fracture toughness of Welsh limestone. Mining Science and Technology, 10(1), 61-70.

Singh, R. N., & Sun, G. (1990). Applications of fracture mechanics to some mining engineering problems. Mining Science and Technology, 10(1), 53-60.

Smith, D. J., Ayatollahi, M. R., & Pavier, M. J. (2006). On the consequences of T-stress in elastic brittle fracture. Proceedings of the Royal Society A: Mathematical, Physical and Engineering Sciences, 462(2072), 2415-2437.

Sun, C. T., & Jin, Z. H. (2012). Chapter 4—Energy Release Rate. Fracture Mechanics, 1st ed.; Sun, CT, Jin, ZH, Eds, 77-103.

Szwedzicki, T. (2003). Rock mass behaviour prior to failure. International journal of rock mechanics and mining sciences, 40(4), 573-584.

Tutluoglu, L., & Keles, C. (2011). Mode I fracture toughness determination with straight notched disk bending method. International Journal of Rock Mechanics and Mining Sciences, 48(8), 12481261.

Wang, C. H. (1996). Introduction to fracture mechanics. Melbourne, Australia: DSTO Aeronautical and Maritime Research Laboratory.

Wang, C. H., & Duong, C. N. (2015). Bonded joints and repairs to composite airframe structures. Academic Press.

Wells, A.A., ‘‘The Condition of Fast Fracture in Aluminum Alloys with Particular Reference to Comet Failures.” British Welding Research Association Report, April 1955.

Wells, A.A., “Unstable Crack Propagation in Metals: Cleavage and Fast Fracture”, Proceedings of the Crack Propagation Symposium, Vol 1, Paper 84, Cranfield, UK, 1961

Westergaard. H.M., “Stresses at a crack, size of the crack and the bending of reinforced concrete”, Prov. American Concrete Institute, Vol.30, pp. 93-102, 1934.

Wills, B. A., & Napier-Munn, T. J. (2006). An introduction to the practical aspects of ore treatment and mineral recovery. Wills' Mineral Processing Technology, 267-352.

Withey, P. A. (1997). Fatigue failure of the de Havilland comet I. Engineering failure analysis, 4(2), 147-154.

Wong, L. N. Y., Guo, T. Y., Lam, W. K., & Ng, J. Y. H. (2019). Experimental Study of Cracking Characteristics of Kowloon Granite Based on Three Mode I Fracture Toughness Methods. Rock Mechanics and Rock Engineering, 1-19.

Yarema, S. Y. (1996). On the contribution of GR Irwin to fracture mechanics. Materials Science, 31(5), 617-623.

Zhou YX, Xia K, Li XB, Li HB, Ma GW, Zhao J, Zhou ZL, Dai F (2012) Suggested methods for determining the dynamic strength parameters and Mode-I fracture toughness of rock materials. Int J of Rock Mech Min Sci 49:105–112

APPENDICES

A. STATIC DEFORMABILITY TEST CURVES

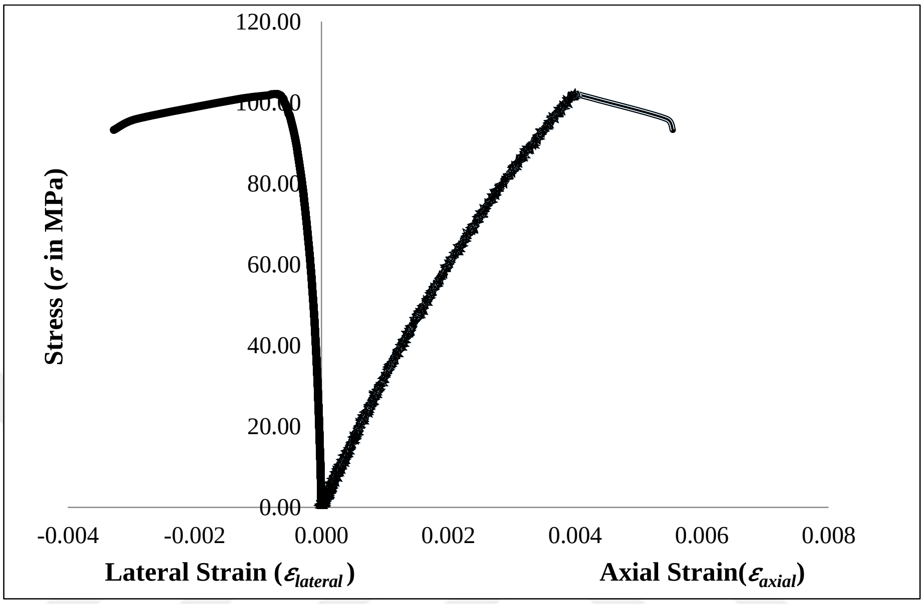

Figure A. 1. Stress-strain curves for SD-1 specimen

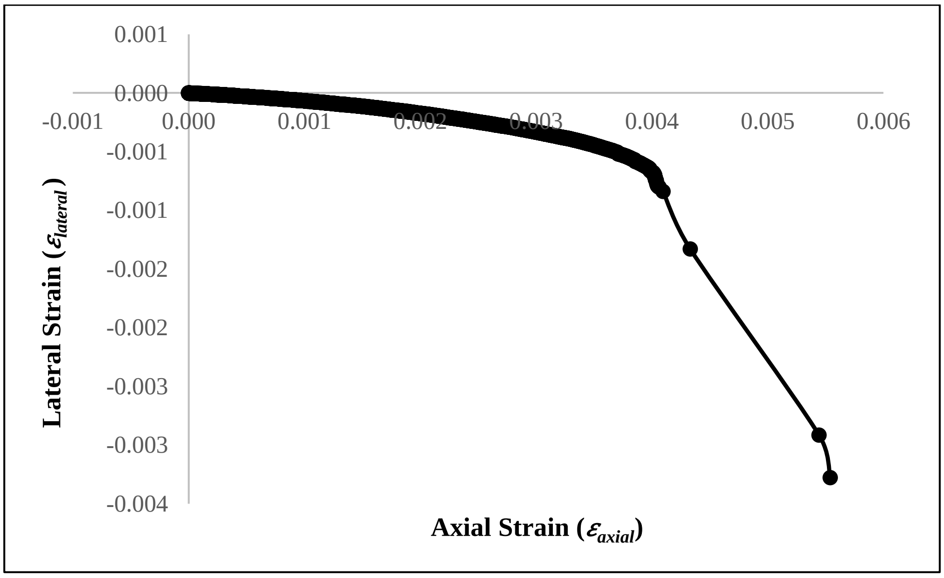

Figure A. 2. Lateral strain-axial strain curve for SD-1 specimen

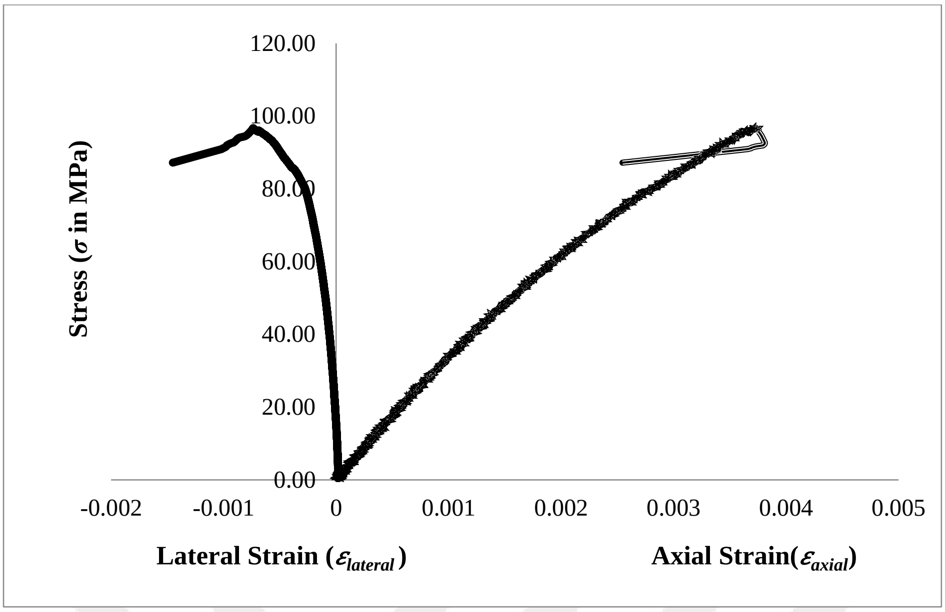

Figure A. 3. Stress-strain curves for SD-2 specimen

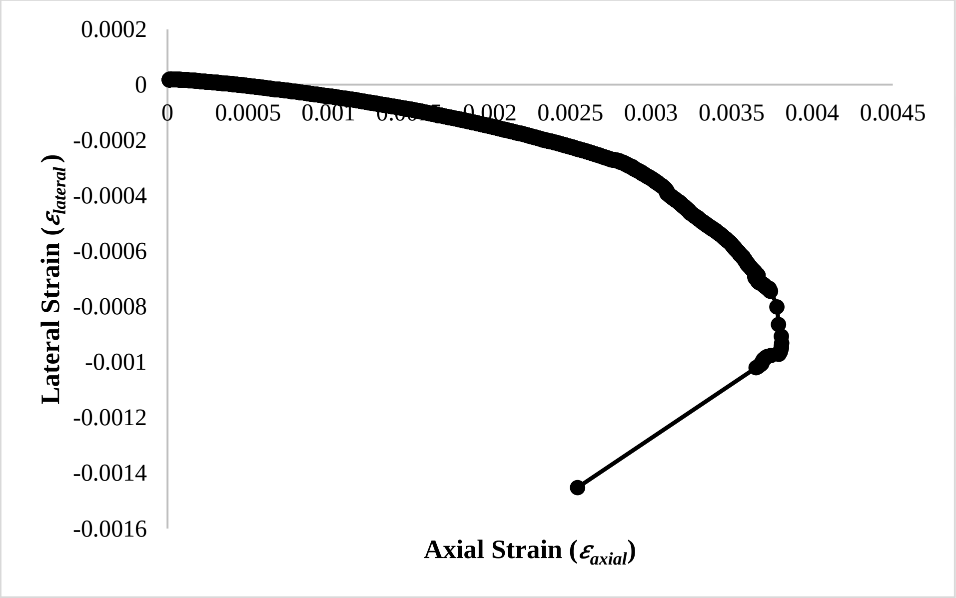

Figure A. 4. Lateral strain-axial strain curve for SD-2 specimen

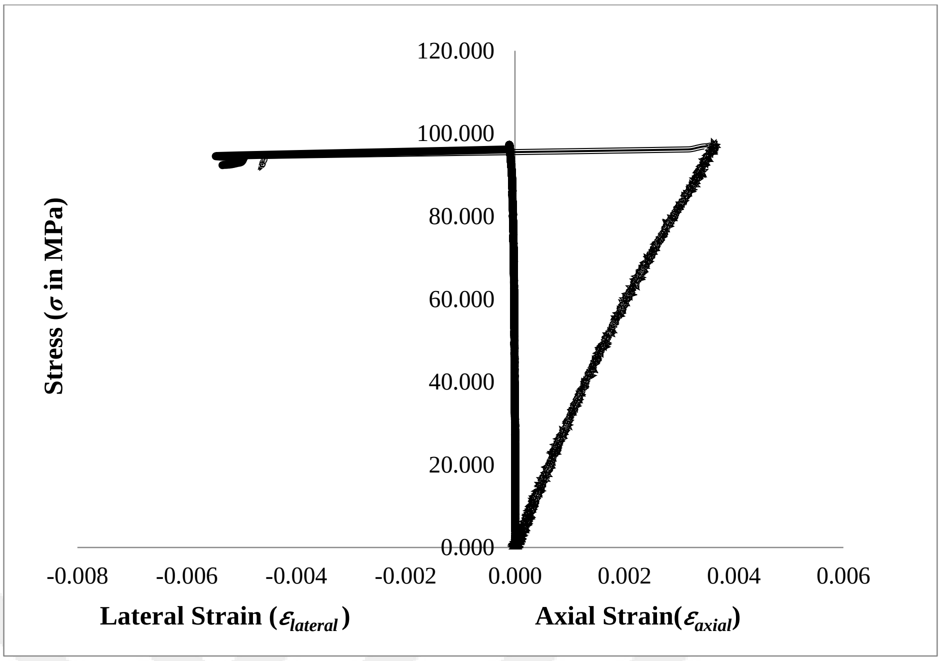

Figure A. 5. Stress-strain curves for SD-3 specimen

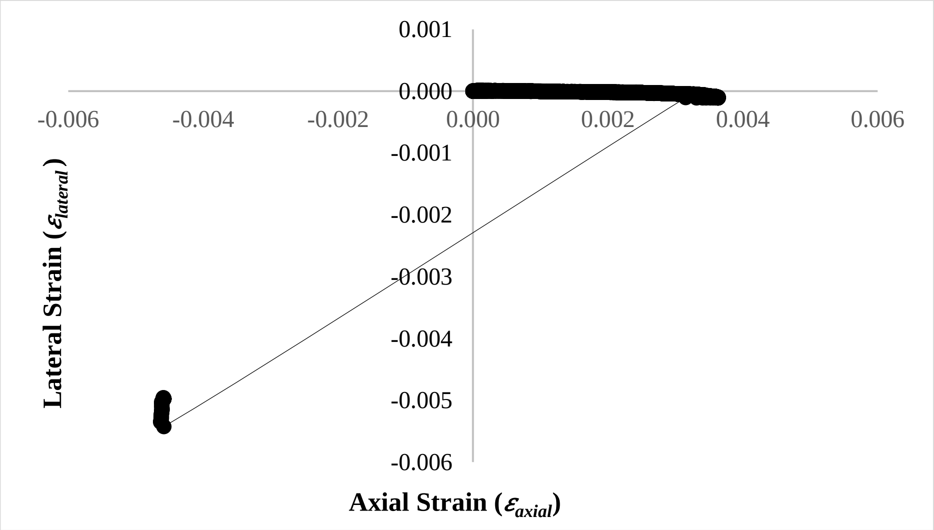

Figure A. 6. Lateral strain-axial strain curve for SD-3 specimen

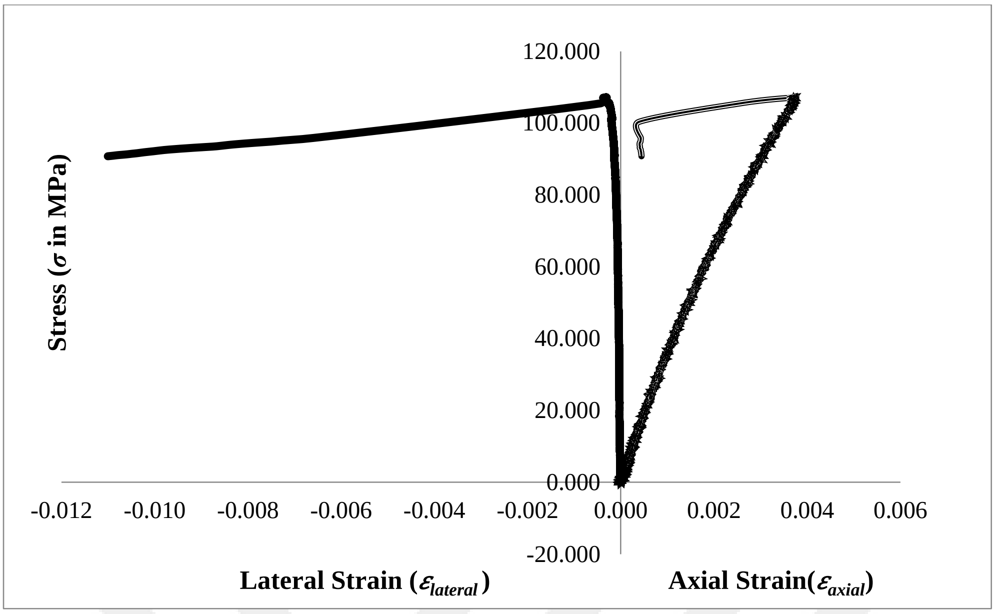

Figure A. 7. Stress-strain curves for SD-4 specimen

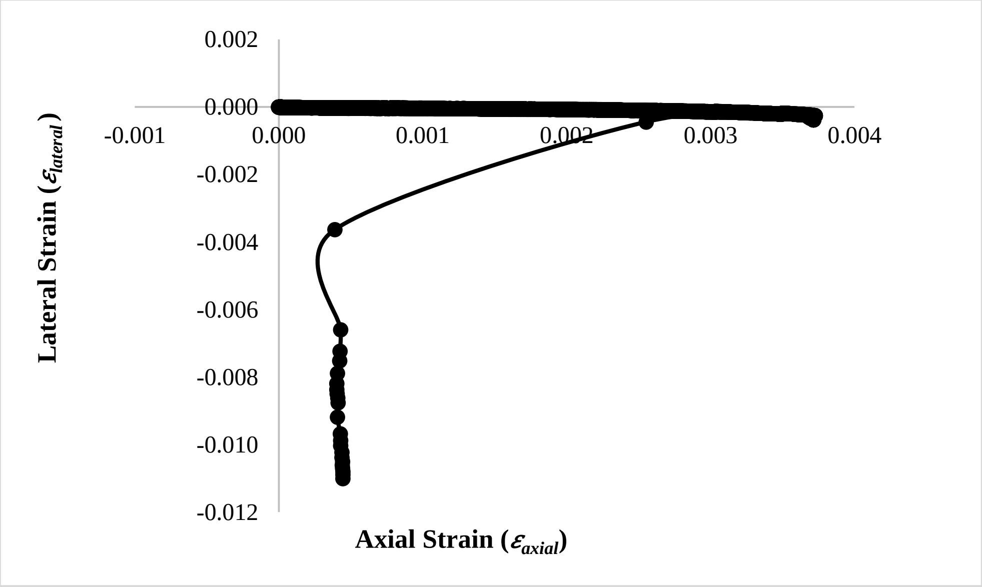

Figure A. 8. Lateral strain-axial strain curve for SD-4 specimen

B. INDIRECT TENSILE (BRAZILIAN) TEST CURVES

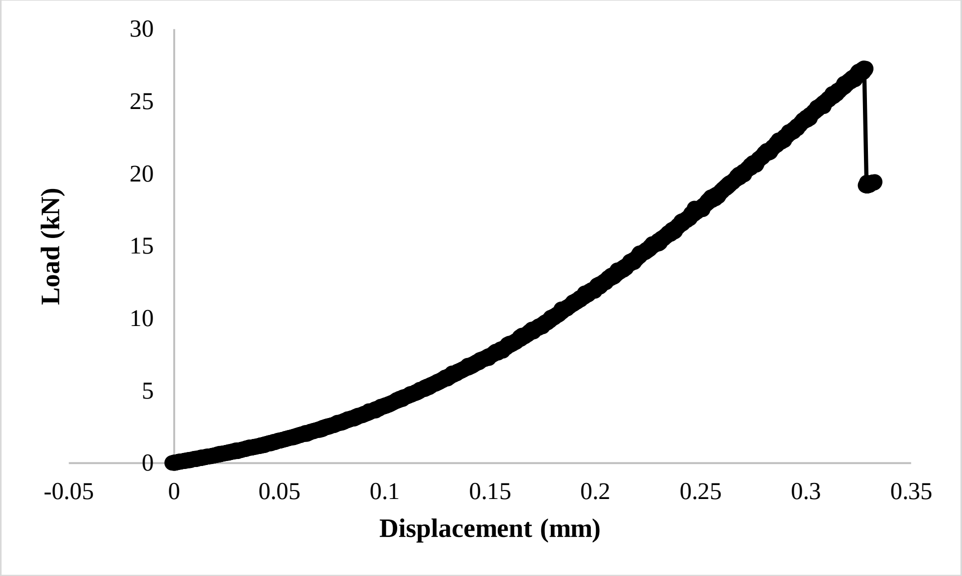

Figure B. 1. Load-displacement curve for BT-1 specimen

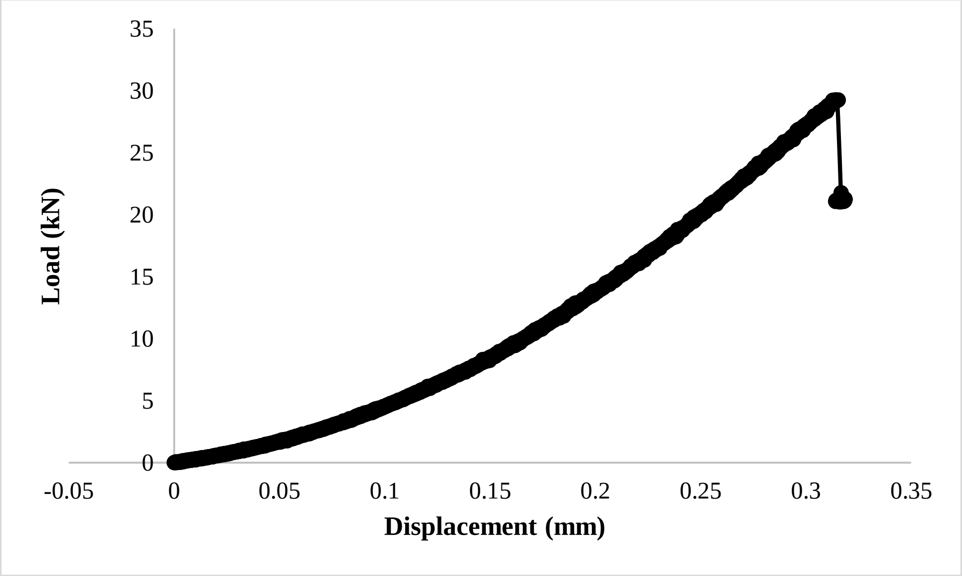

Figure B. 2. Load-displacement curve for BT-2 specimen

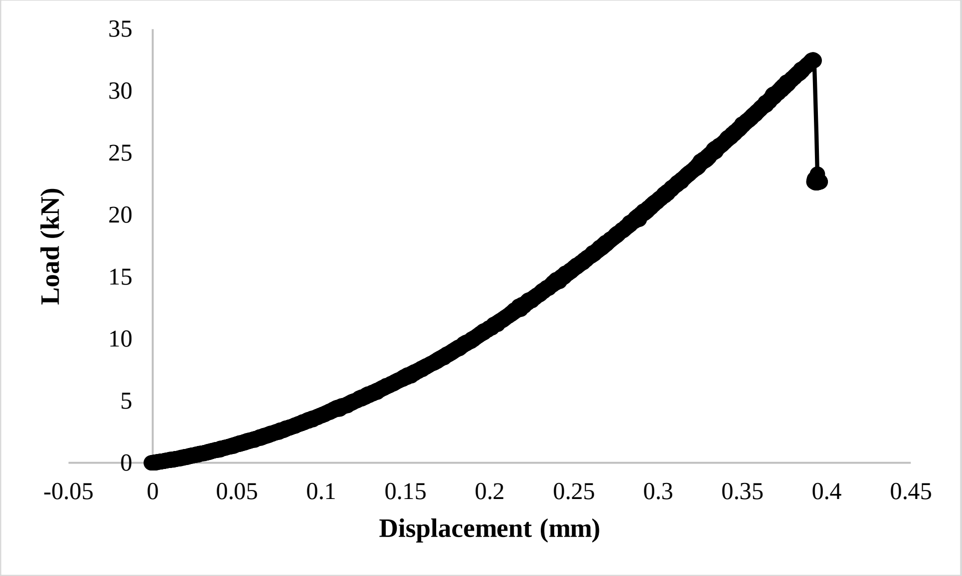

Figure B. 3. Load-displacement curve for BT-3 specimen

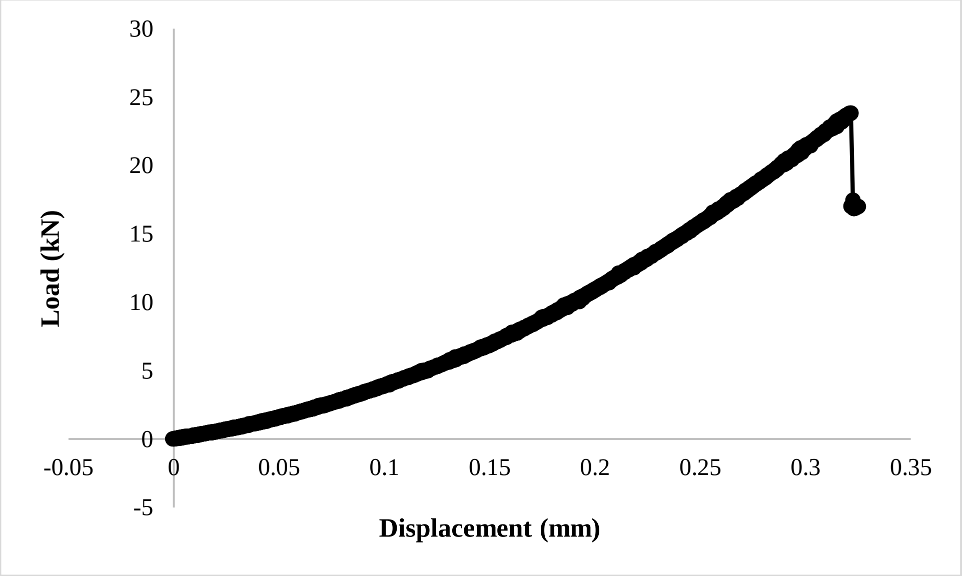

Figure B. 4. Load-displacement curve for BT-4 specimen

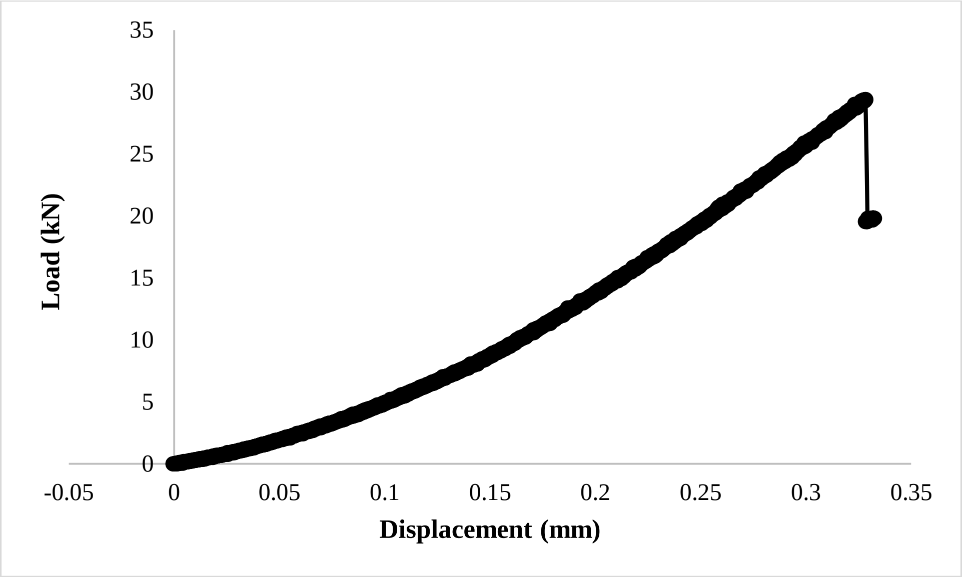

Figure B. 5. Load-displacement curve for BT-5 specimen

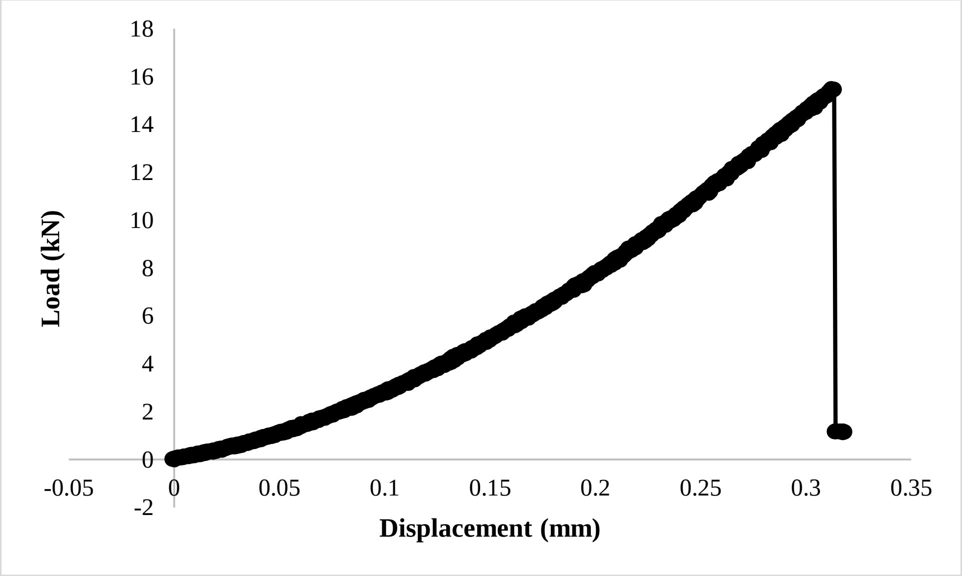

Figure B. 6. Load-displacement curve for BT-6 specimen

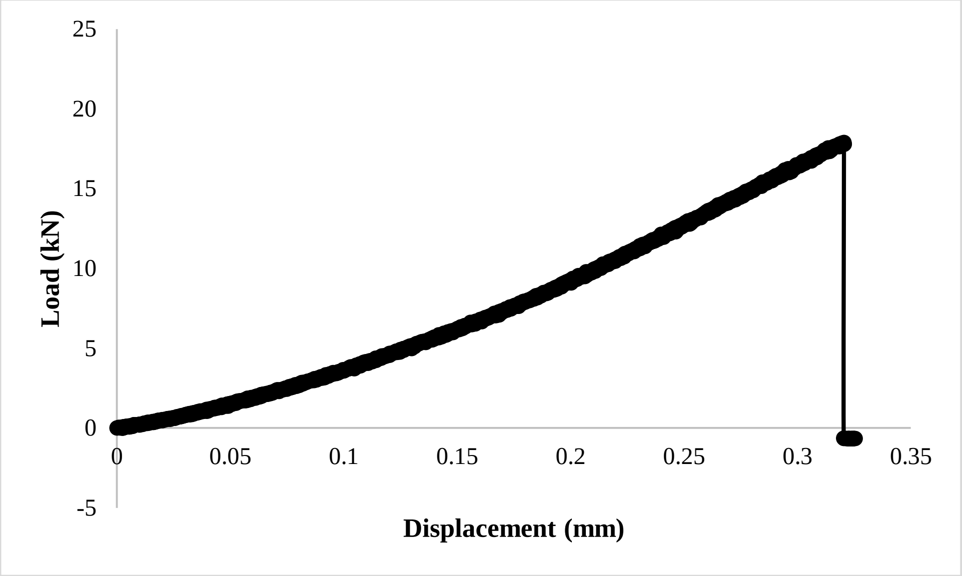

Figure B. 7. Load-displacement curve for BT-7 specimen

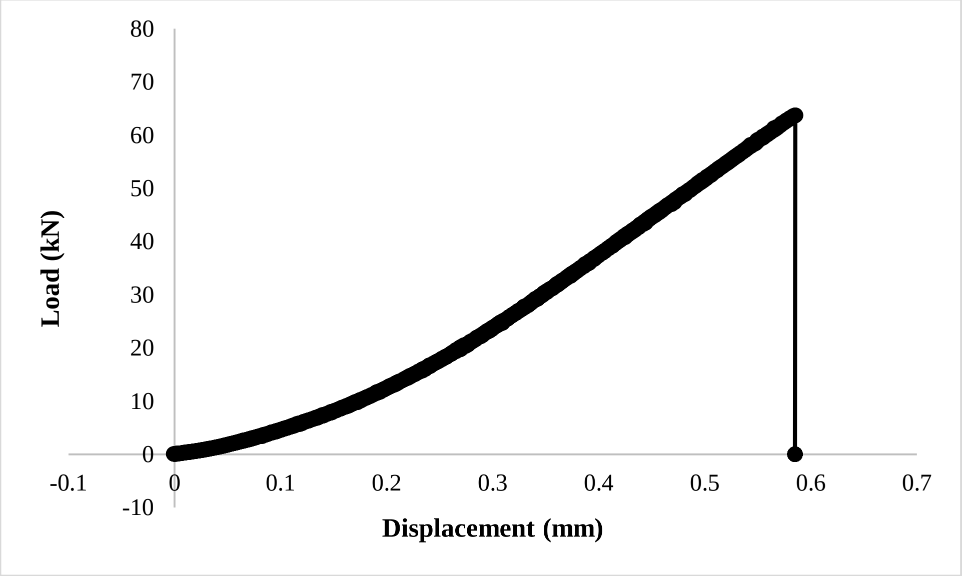

Figure B. 8. Load-displacement curve for BT-8 specimen

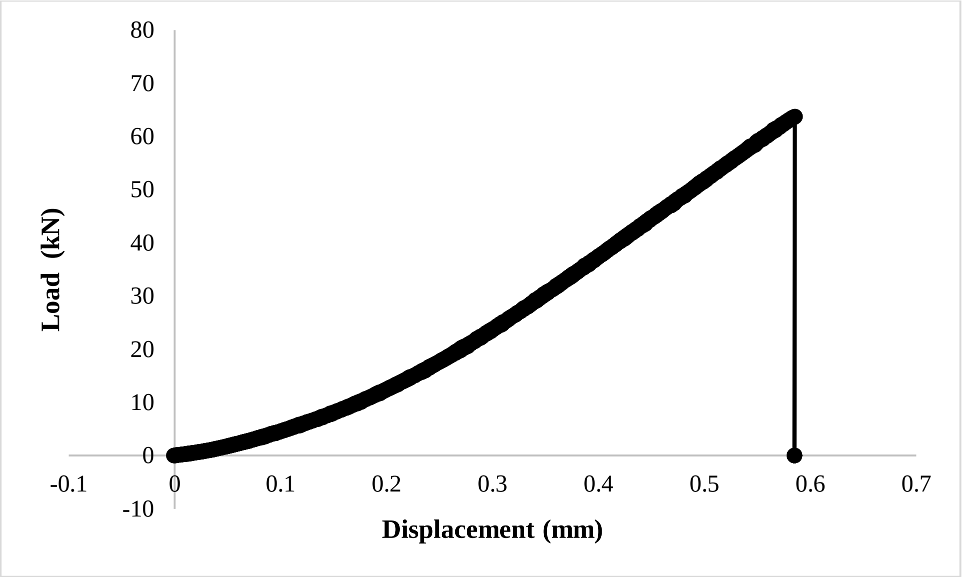

Figure B. 9. Load-displacement curve for BT-9 specimen

C. GEOMETRICAL PROPERTIES OF THE TEST SPECIMENS

Table C. 1. *Geometrical properties of the SNDB specimens with t=50 mm*

Specimen Code	D	t	S/R	P_{cr}	K_{Ic}
	mm	**mm**		**kN**	**MPa$\sqrt{m}$**
SNDB-50-040-1	100.20	50.35	0.40	35.65	1.20
SNDB-50-040-2	100.15	50.30	0.40	35.90	1.21
SNDB-50-040-3	100.20	50.25	0.40	43.63	1.47
SNDB-50-045-1	100.30	50.30	0.45	30.28	1.20
SNDB-50-045-2	100.00	50.15	0.45	26.48	1.06
SNDB-50-045-3	100.10	50.20	0.45	35.42	1.41
SNDB-50-045-4	100.15	50.25	0.45	36.20	1.44
SNDB-50-050-1	100.00	50.45	0.50	27.86	1.26
SNDB-50-050-2	100.05	50.40	0.50	28.93	1.31
SNDB-50-050-3	100.00	50.35	0.50	26.27	1.19
SNDB-50-055-1	100.10	50.00	0.55	20.32	1.04
SNDB-50-055-2	100.25	50.05	0.55	23.57	1.21
SNDB-50-055-3	100.15	50.05	0.55	27.80	1.43
SNDB-50-060-1	100.15	50.20	0.60	20.54	1.14
SNDB-50-060-2	100.15	50.30	0.60	20.93	1.16
SNDB-50-060-3	100.20	50.20	0.60	24.28	1.35
SNDB-50-070-1	100.00	50.00	0.70	19.23	1.30
SNDB-50-070-2	100.05	50.10	0.70	17.50	1.18
SNDB-50-070-3	100.00	50.00	0.70	16.86	1.14
SNDB-50-080-1	100.20	50.30	0.80	15.34	1.19
SNDB-50-080-2	100.05	50.10	0.80	14.32	1.12
SNDB-50-080-3	100.10	50.40	0.80	16.58	1.28
SNDB-50-085-1	100.00	50.35	0.85	14.80	1.23
SNDB-50-085-2	100.10	50.20	0.85	15.33	1.27
SNDB-50-085-3	100.05	50.10	0.85	12.95	1.08
SNDB-50-090-1	100.10	50.35	0.90	14.20	1.25
SNDB-50-090-2	100.00	50.20	0.90	13.69	1.21
SNDB-50-090-3	100.15	50.10	0.90	12.17	1.08

Table C. 2. *Geometrical properties of the SNDB specimens with t=60 mm*

Specimen Code	D	t	S/R	P_{cr}	K_{Ic}
	mm	**mm**		**kN**	$\mathbf{MPa\sqrt{m}}$
SNDB-60-040-1	100.10	60.20	0.40	64.50	1.46
SNDB-60-040-2	100.00	60.15	0.40	63.89	1.45
SNDB-60-040-3	100.15	60.30	0.40	73.46	1.66
SNDB-60-045-1	100.50	60.15	0.45	62.35	1.72
SNDB-60-045-2	100.00	60.25	0.45	59.46	1.64
SNDB-60-045-4	100.00	60.30	0.45	41.19	1.14
SNDB-60-050-1	100.05	60.20	0.50	47.64	1.53
SNDB-60-050-2	100.10	60.05	0.50	45.05	1.45
SNDB-60-050-3	100.05	60.30	0.50	45.93	1.47
SNDB-60-055-1	100.20	60.15	0.55	41.91	1.52
SNDB-60-055-2	100.25	60.40	0.55	38.01	1.37
SNDB-60-055-3	100.25	60.00	0.55	40.49	1.47
SNDB-60-060-1	100.00	60.05	0.60	29.63	1.20
SNDB-60-060-2	100.05	60.35	0.60	39.83	1.60
SNDB-60-060-3	100.00	60.20	0.60	35.69	1.44
SNDB-60-070-1	100.10	60.20	0.70	24.16	1.16
SNDB-60-070-2	100.10	60.15	0.70	30.89	1.49
SNDB-60-070-3	100.05	60.25	0.70	27.39	1.32
SNDB-60-080-1	100.00	60.10	0.80	18.54	1.04
SNDB-60-080-2	100.05	60.30	0.80	28.06	1.56
SNDB-60-080-2	100.00	60.25	0.80	26.94	1.50
SNDB-60-080-3	100.00	60.05	0.80	17.50	0.98
SNDB-60-085-1	100.10	60.35	0.85	21.56	1.28
SNDB-60-085-2	100.15	60.10	0.85	20.72	1.24
SNDB-60-085-3	100.15	60.40	0.85	20.62	1.22
SNDB-60-090-1	100.05	60.15	0.90	19.02	1.21

Table C. 3. *Geometrical properties of the SCB specimens*

Specimen Code	***R***	***t***	***S/R***	P_{cr}	K_{Ic}
	mm	**mm**		**kN**	$\mathrm{MPa}\sqrt{\mathrm{m}}$
SCB-50-040-1	50.10	50.15	0.40	19.34	1.24
SCB-50-040-2	50.05	50.40	0.40	18.53	1.18
SCB-50-040-3	50.15	50.20	0.40	18.31	1.17
SCB-50-045-1	50.20	50.10	0.45	13.34	1.03
SCB-50-045-2	50.25	50.25	0.45	13.20	1.02
SCB-50-045-3	50.00	50.05	0.45	13.90	1.07
SCB-50-050-1	50.05	50.15	0.50	11.19	1.00
SCB-50-050-2	50.10	50.20	0.50	11.01	0.98
SCB-50-050-3	50.10	50.25	0.50	12.54	1.12
SCB-50-055-1	50.00	50.15	0.55	12.24	1.24
SCB-50-055-2	50.05	50.20	0.55	6.52	0.66
SCB-50-055-3	50.05	50.10	0.55	9.73	0.99
SCB-50-060-1	50.00	50.10	0.60	6.86	0.78
SCB-50-060-2	50.00	50.20	0.60	7.10	0.81
SCB-50-060-3	50.00	50.15	0.60	9.65	1.10
SCB-50-070-1	50.05	50.25	0.70	5.09	0.70
SCB-50-070-2	50.05	50.30	0.70	6.84	0.94
SCB-50-070-3	50.00	50.10	0.70	7.18	0.99
SCB-50-080-1	50.10	50.15	0.80	4.29	0.70
SCB-50-080-2	50.05	50.20	0.80	4.57	0.74
SCB-50-080-3	50.10	50.30	0.80	5.98	0.97
SCB-50-085-1	50.00	50.25	0.85	4.90	0.86
SCB-50-085-2	50.05	50.15	0.85	3.92	0.69
SCB-50-085-3	50.00	50.30	0.85	4.64	0.81
SCB-50-090-1	50.05	50.20	0.90	2.91	0.55
SCB-50-090-2	50.05	50.10	0.90	4.14	0.78
SCB-50-090-3	50.05	50.25	0.90	4.62	0.87

D. FRACTURE TOUGHNESS TEST PHOTOS

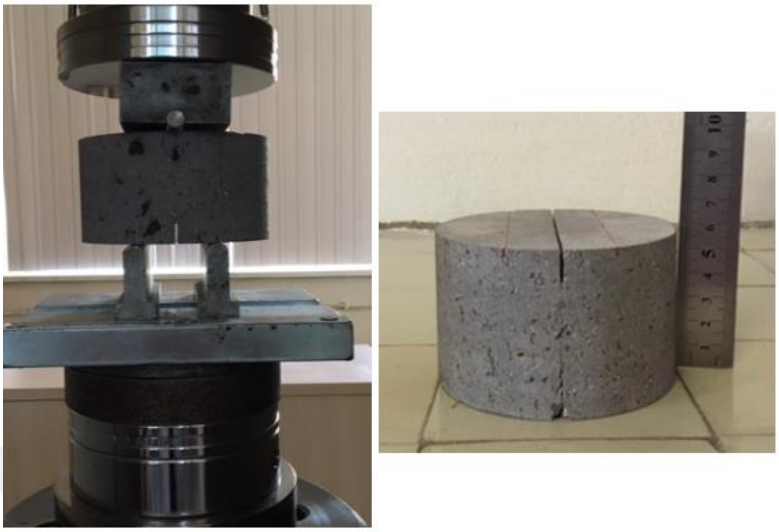

Figure D. 1. SNDB-60-040-1 specimen during and after test

Figure D. 2. 60 mm thick SNDB test specimens with 40 mm span length

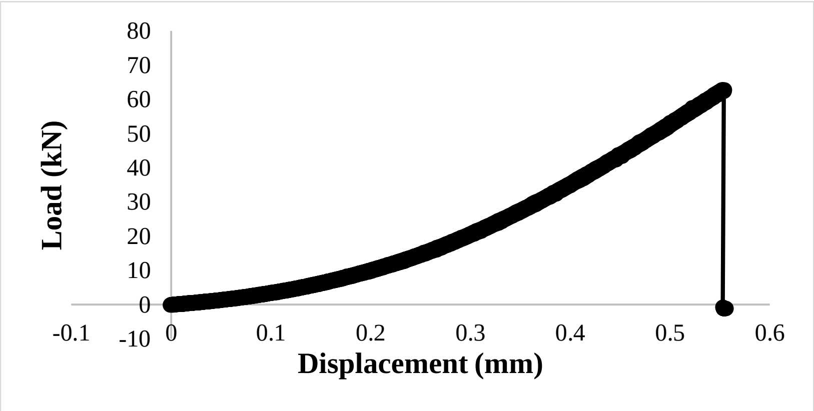

Figure D. 3. Load versus displacement curve of SNDB-60-040-1

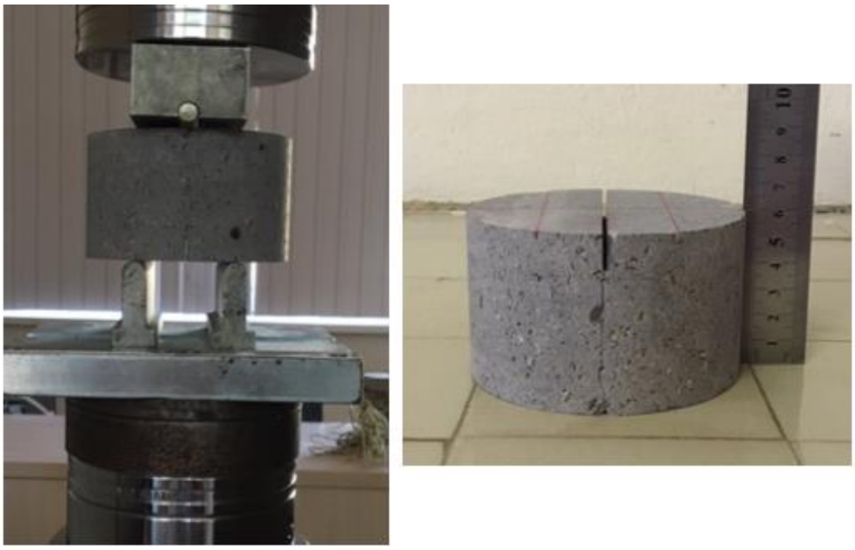

Figure D. 4. SNDB-60-045-2 specimen during and after test

Figure D. 5. 60 mm thick SNDB test specimens with 45 mm span length

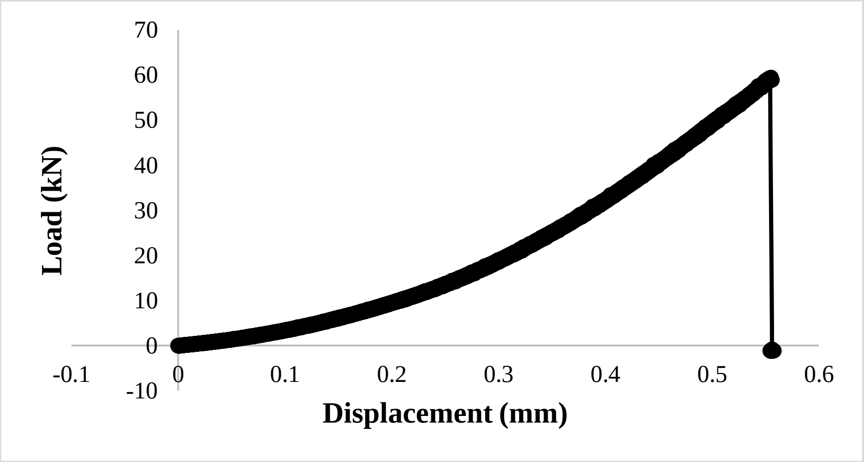

Figure D. 6. Load versus displacement curve of SNDB-60-045-2

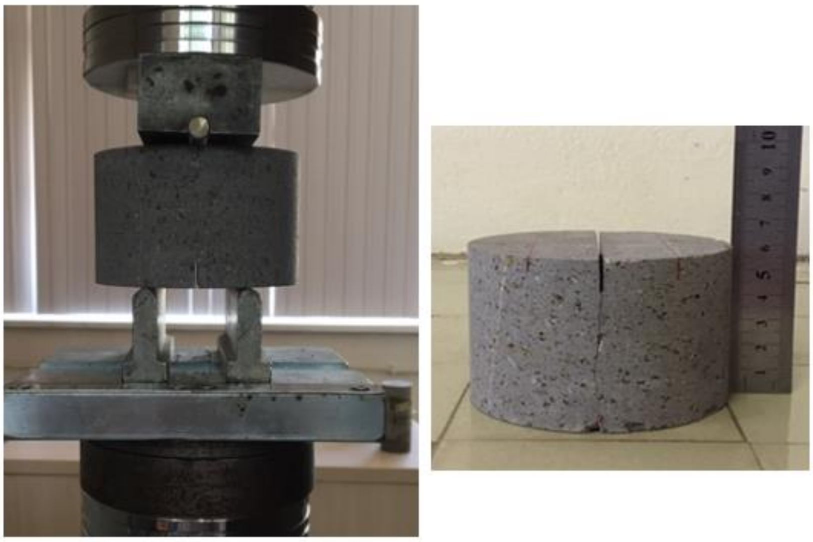

Figure D. 7. SNDB-60-050-3 specimen during and after test

Figure D. 8. 60 mm thick SNDB test specimens with 50 mm span length

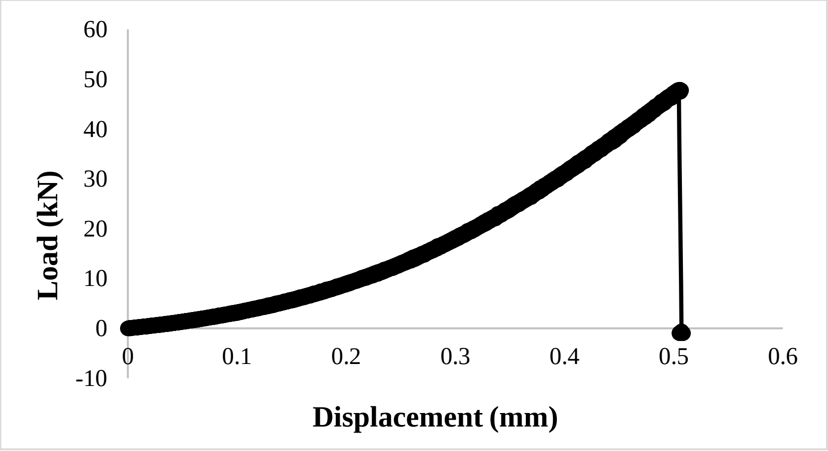

Figure D. 9. Load versus displacement curve of SNDB-60-050-3

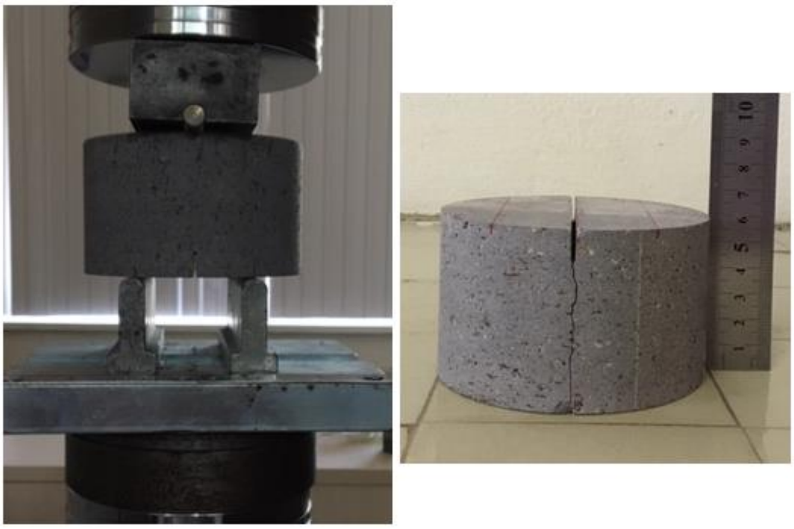

Figure D. 10. SNDB-60-055-3 specimen during and after test

Figure D. 11. 60 mm thick SNDB test specimens with 55 mm span length

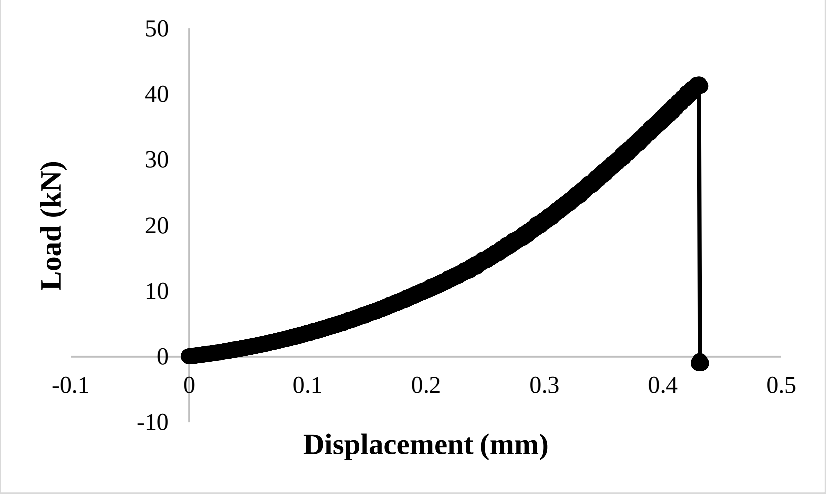

Figure D. 12. Load versus displacement curve of SNDB-60-055-3

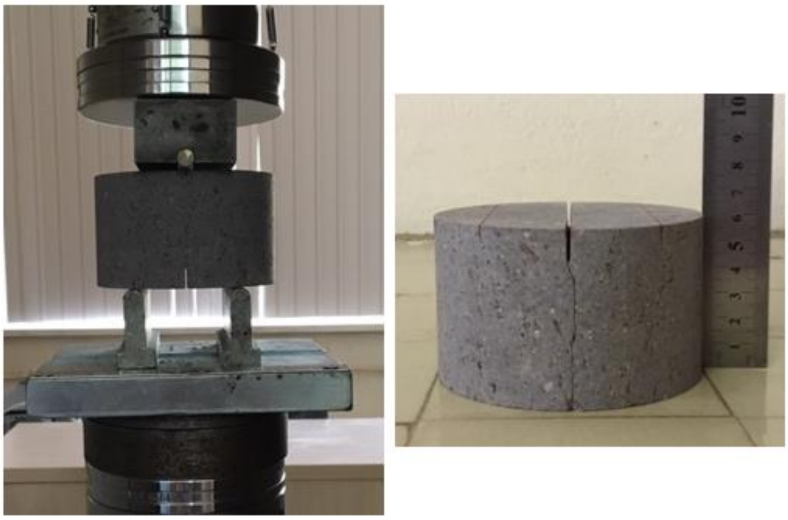

Figure D. 13. SNDB-60-060-3 specimen during and after test

Figure D. 14. 60 mm thick SNDB test specimens with 60 mm span length

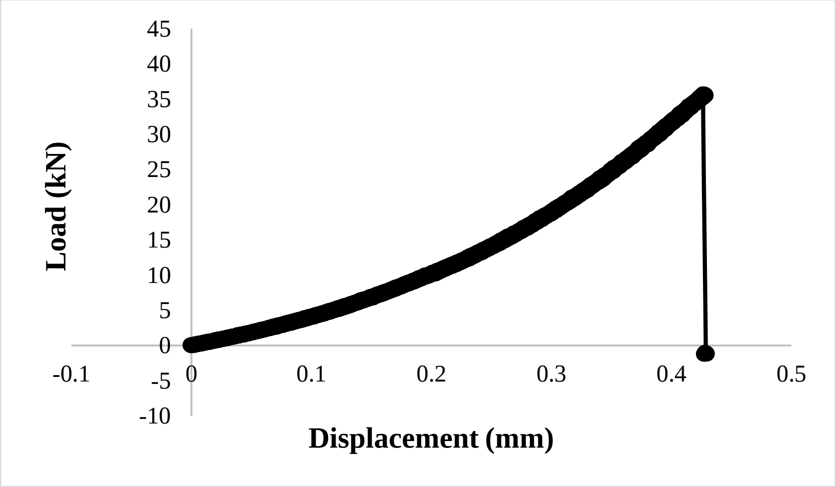

Figure D. 15. Load versus displacement curve of SNDB-60-060-3

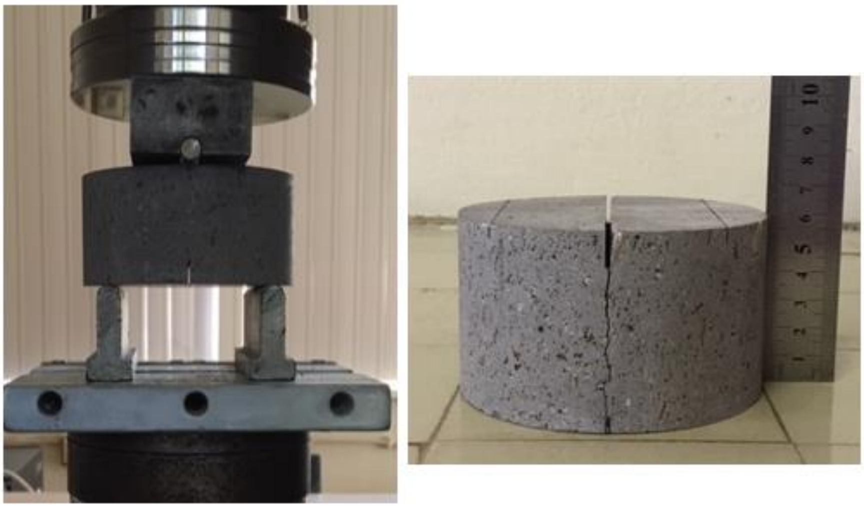

Figure D. 16. SNDB-60-070-3 specimen during and after test

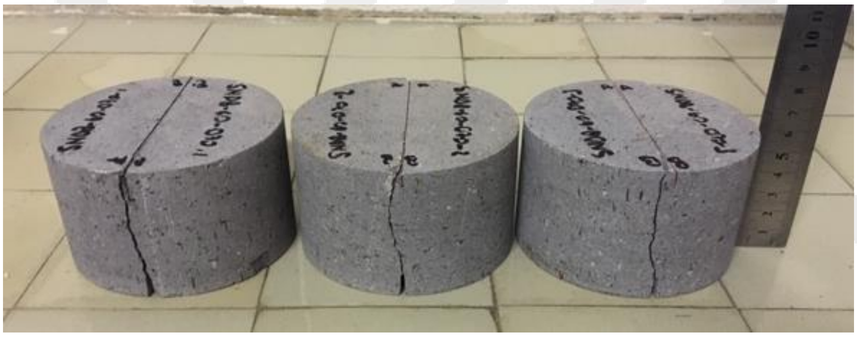

Figure D. 17. 60 mm thick SNDB test specimens with 70 mm span length

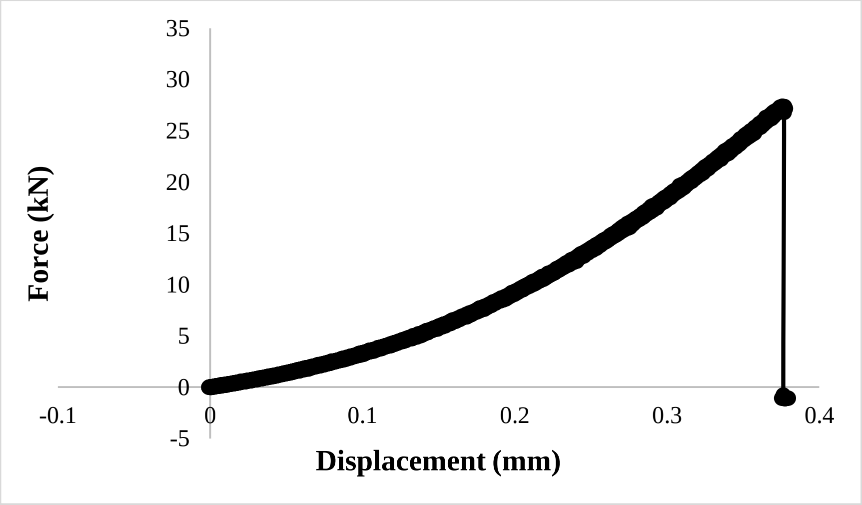

Figure D. 18. Load versus displacement curve of SNDB-60-070-3

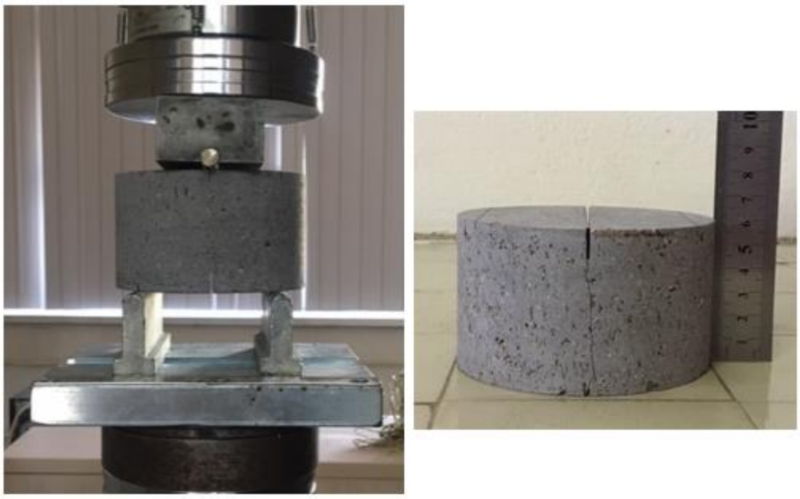

Figure D. 19. SNDB-60-080-1 specimen during and after test

Figure D. 20. 60 mm thick SNDB test specimens with 80 mm span length

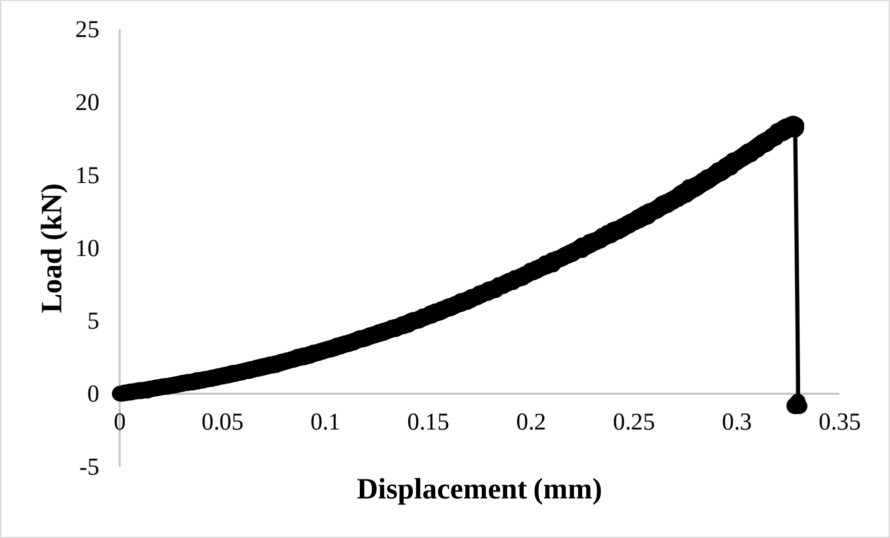

Figure D. 21. Load versus displacement curve of SNDB-60-080-1

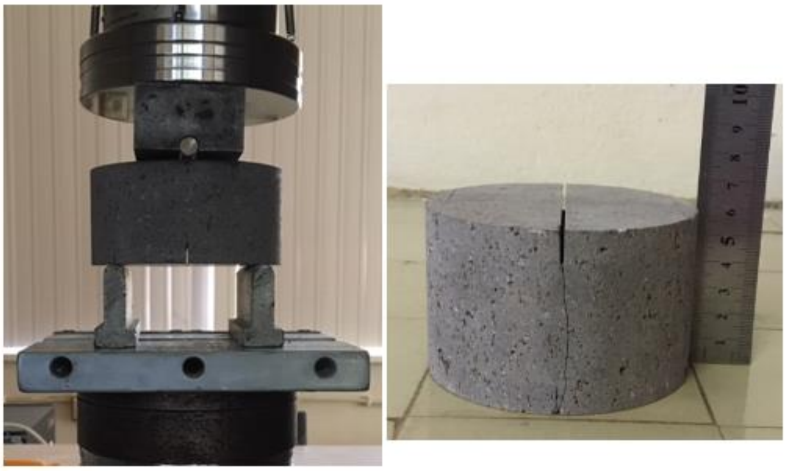

Figure D. 22. SNDB-60-085-2 specimen during and after test

Figure D. 23. 60 mm thick SNDB test specimens with 85 mm span length

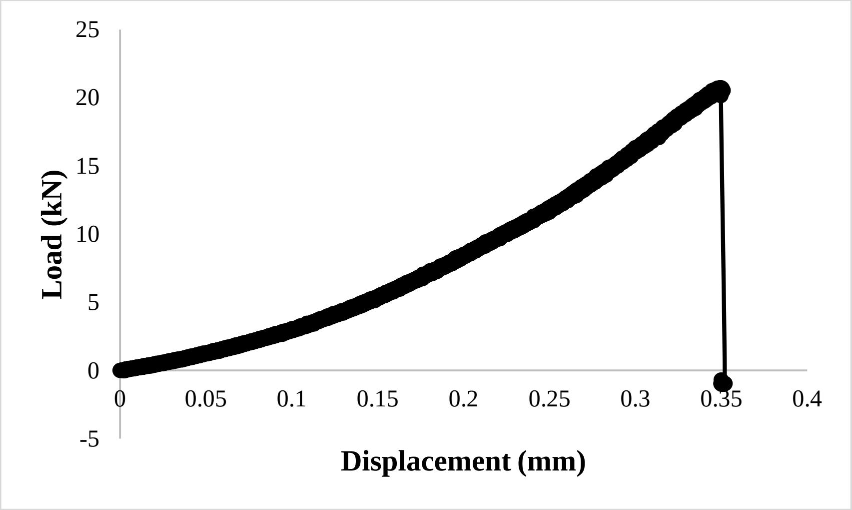

Figure D. 24. Load versus displacement curve of SNDB-60-085-2

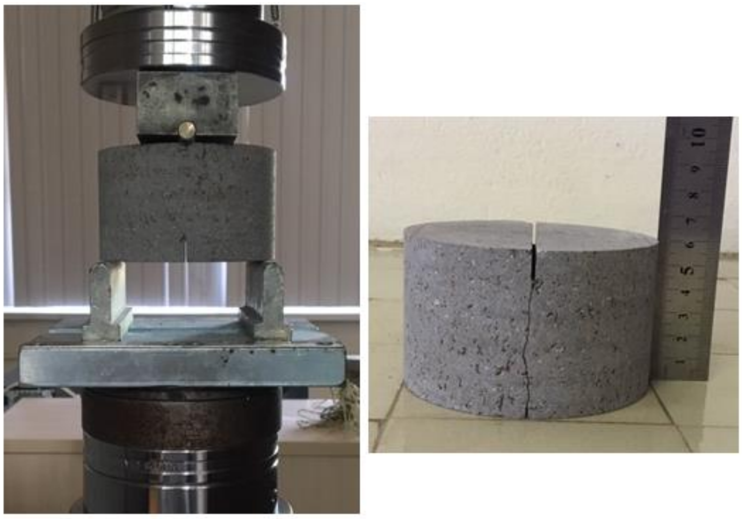

Figure D. 25. SNDB-60-090-1 specimen during and after test

Figure D. 26. 60 mm thick SNDB test specimens with 90 mm span length

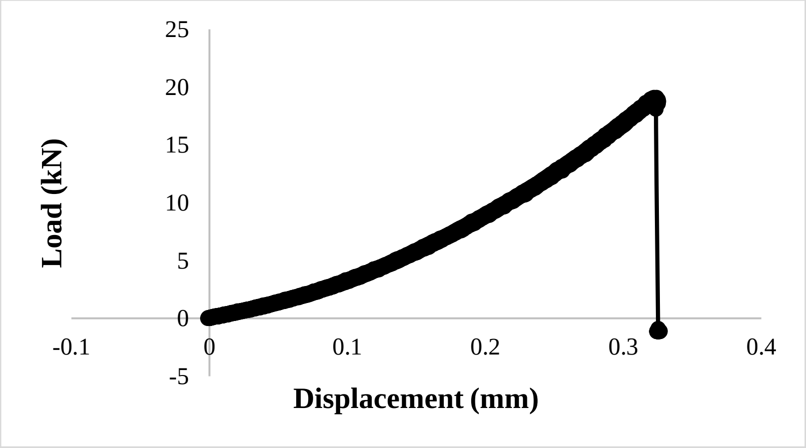

Figure D. 27. Load versus displacement curve of SNDB-60-090-1

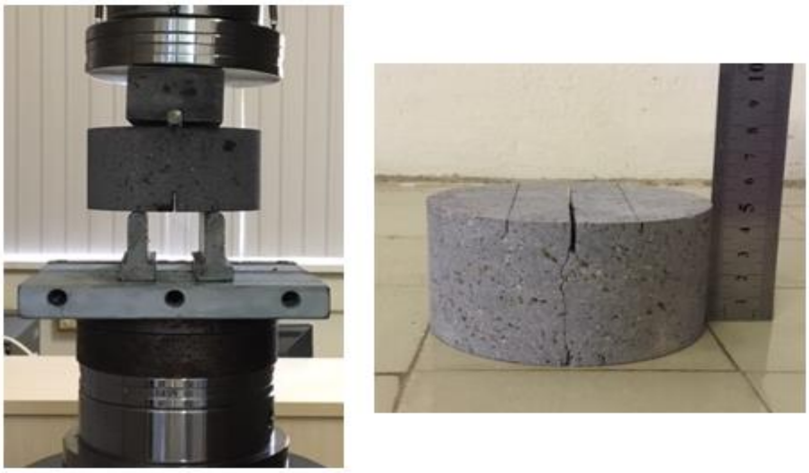

Figure D. 28. SNDB-50-040-2 specimen during and after test

Figure D. 29. 50 mm thick SNDB test specimens with 40 mm span length

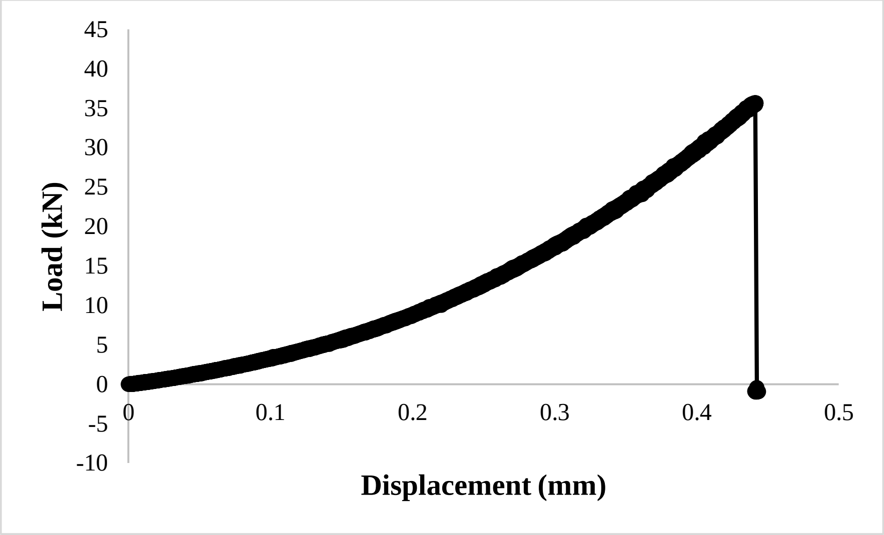

Figure D. 30. Load versus displacement curve of SNDB-50-040-2

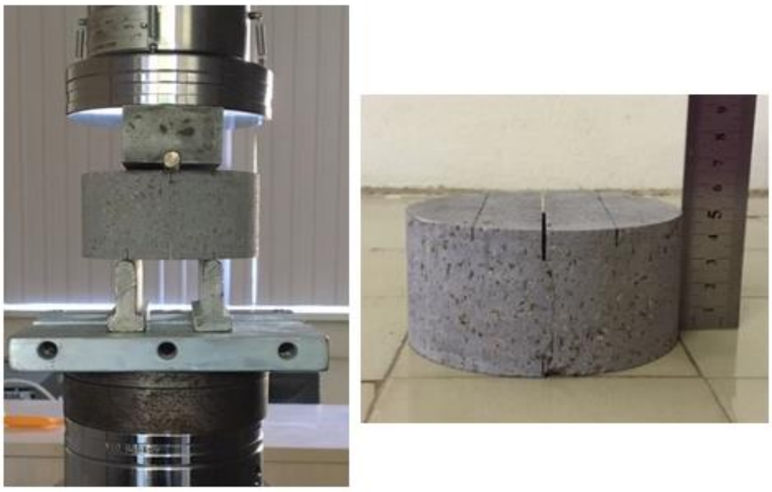

Figure D. 31. SNDB-50-045-2 specimen during and after test

Figure D. 32. 50 mm thick SNDB test specimens with 45 mm span length

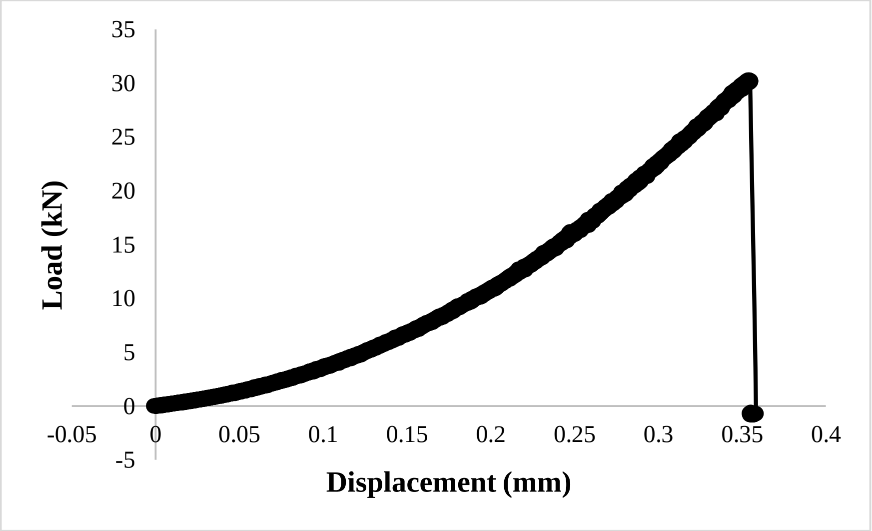

Figure D. 33. Load versus displacement curve of SNDB-50-045-2

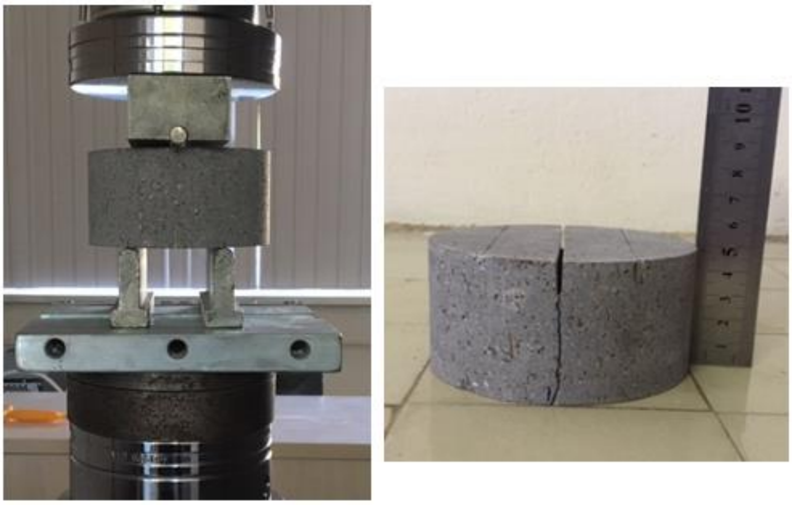

Figure D. 34. SNDB-50-050-1 specimen during and after test

Figure D. 35. 50 mm thick SNDB test specimens with 50 mm span length

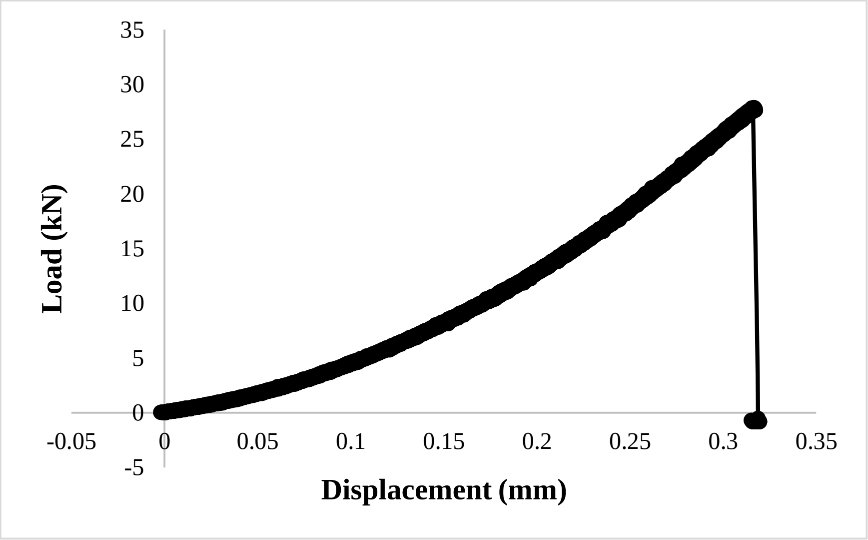

Figure D. 36. Load versus displacement curve of SNDB-50-050-1

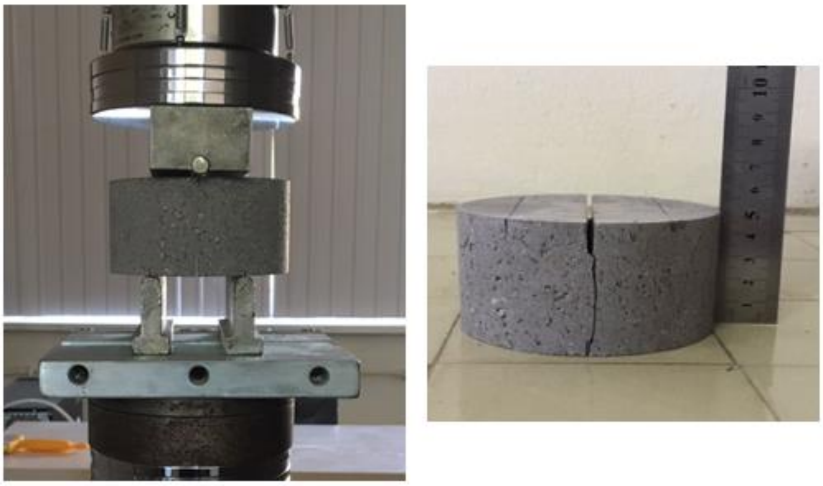

Figure D. 37. SNDB-50-055-2 specimen during and after test

Figure D. 38. 50 mm thick SNDB test specimens with 55 mm span length

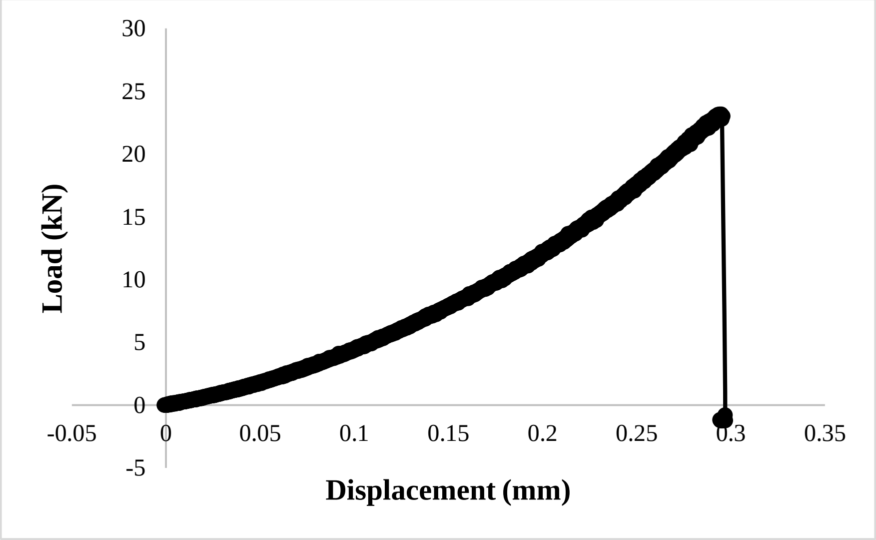

Figure D. 39. Load versus displacement curve of SNDB-50-055-2

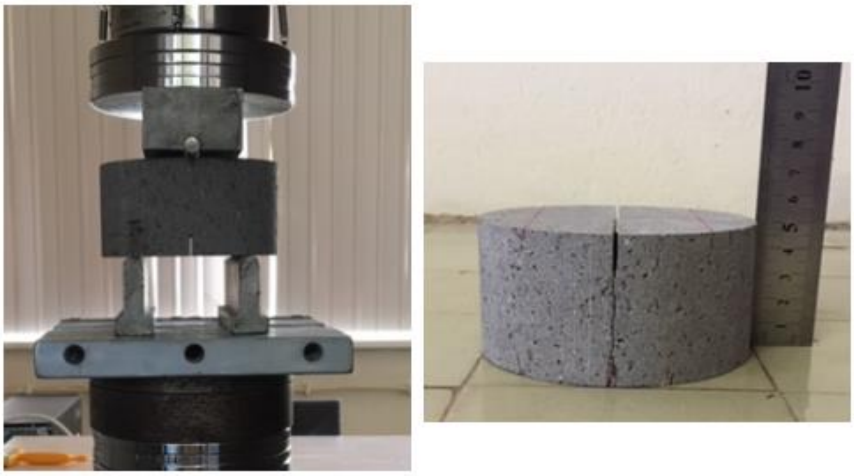

Figure D. 40. SNDB-50-060-2 specimen during and after test

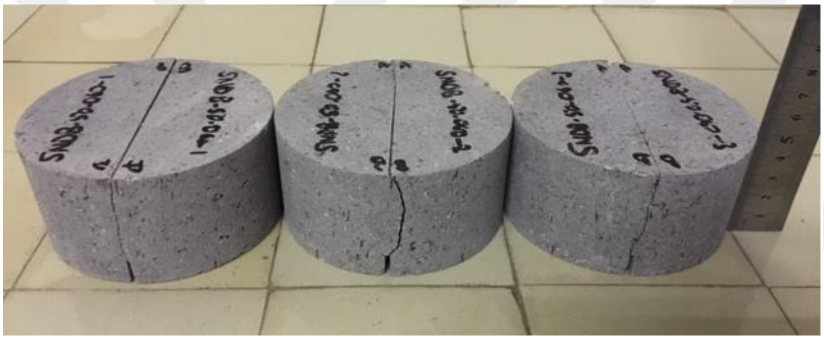

Figure D. 41. 50 mm thick SNDB test specimens with 60 mm span length

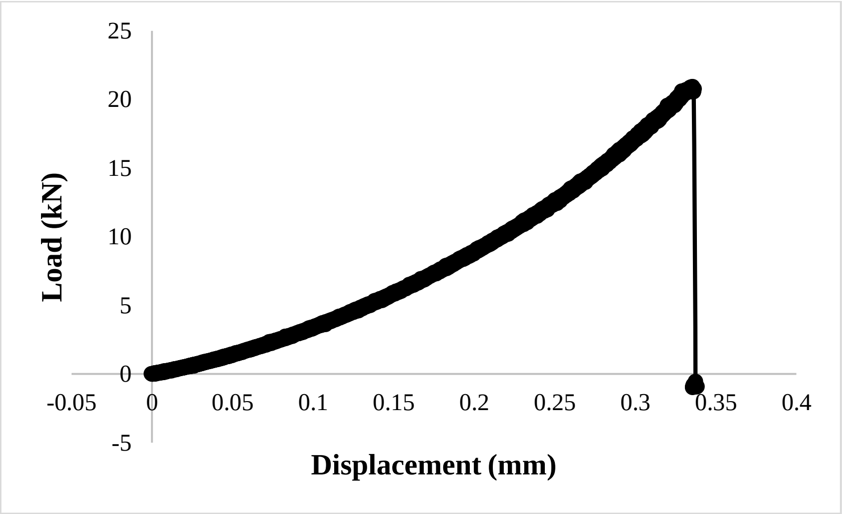

Figure D. 42. Load versus displacement curve of SNDB-50-060-2

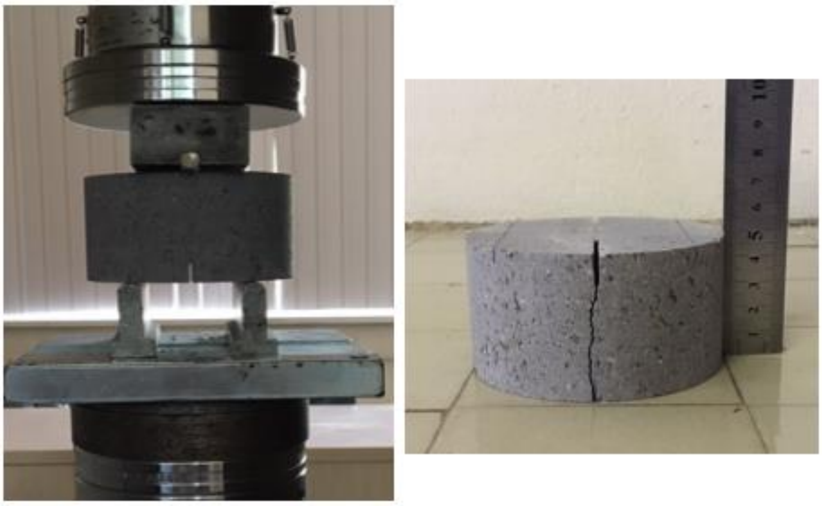

Figure D. 43. SNDB-50-070-2 specimen during and after test

Figure D. 44. 50 mm thick SNDB test specimens with 70 mm span length

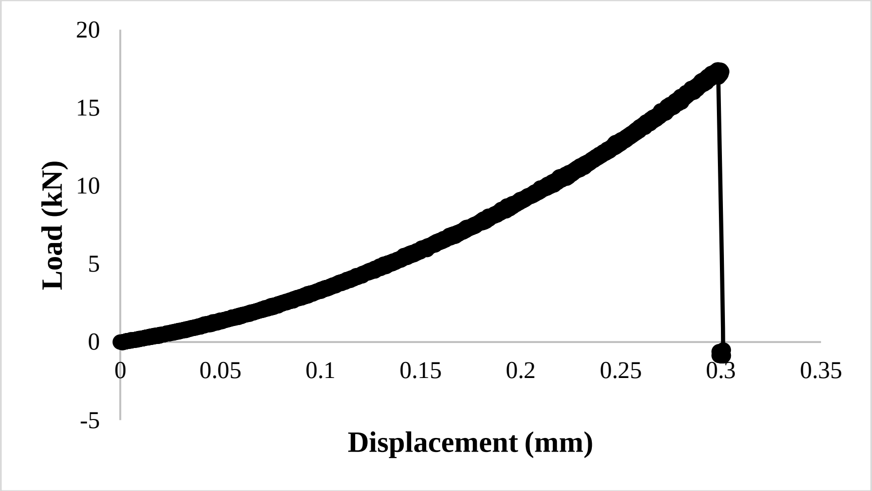

Figure D. 45. Load versus displacement curve of SNDB-50-070-2

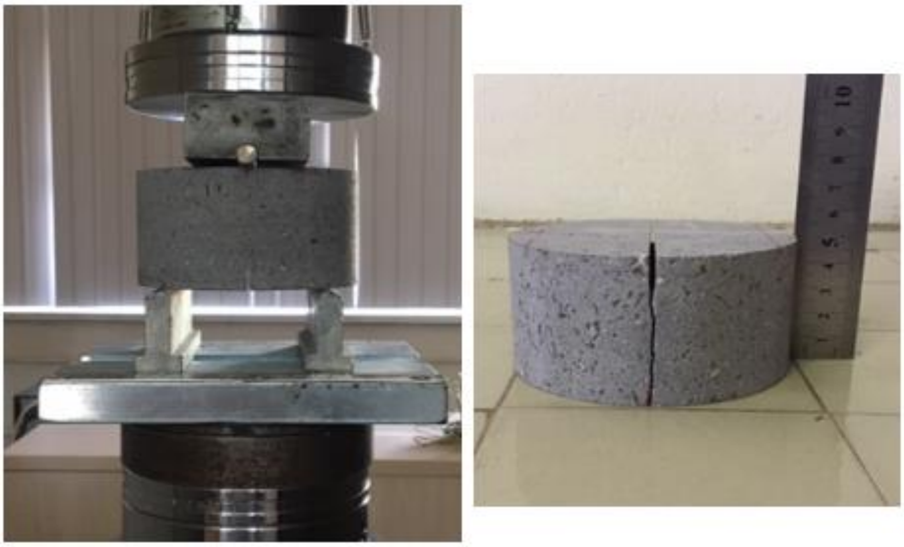

Figure D. 46. SNDB-50-080-1 specimen during and after test

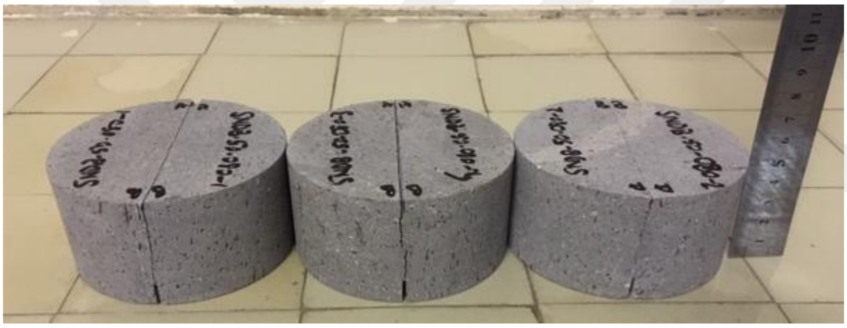

Figure D. 47. 50 mm thick SNDB test specimens with 80 mm span length

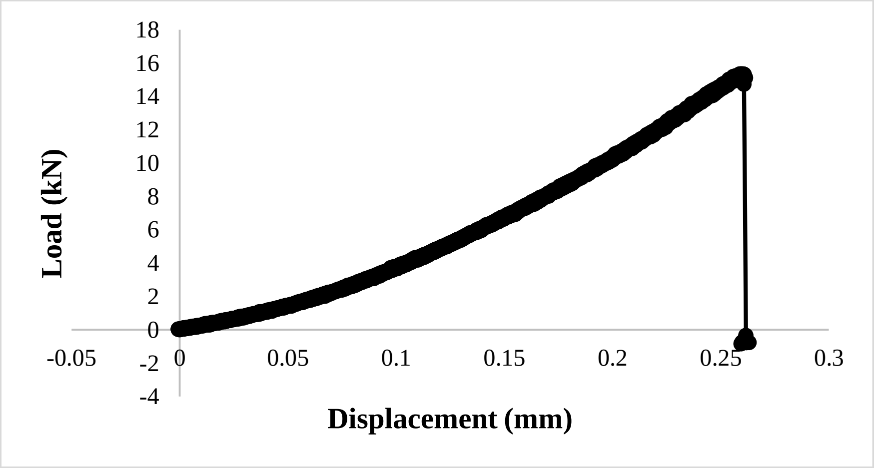

Figure D. 48. Load versus displacement curve of SNDB-50-080

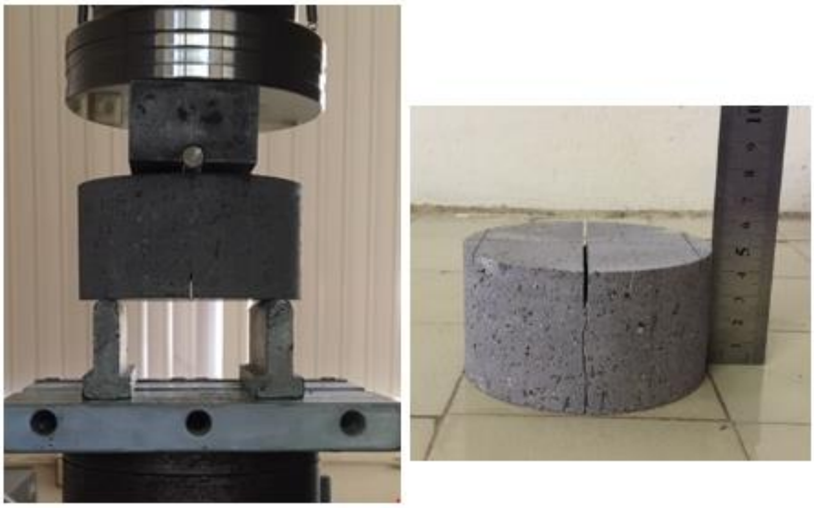

Figure D. 49. SNDB-50-085-1 specimen during and after test

Figure D. 50. 50 mm thick SNDB test specimens with 85 mm span length

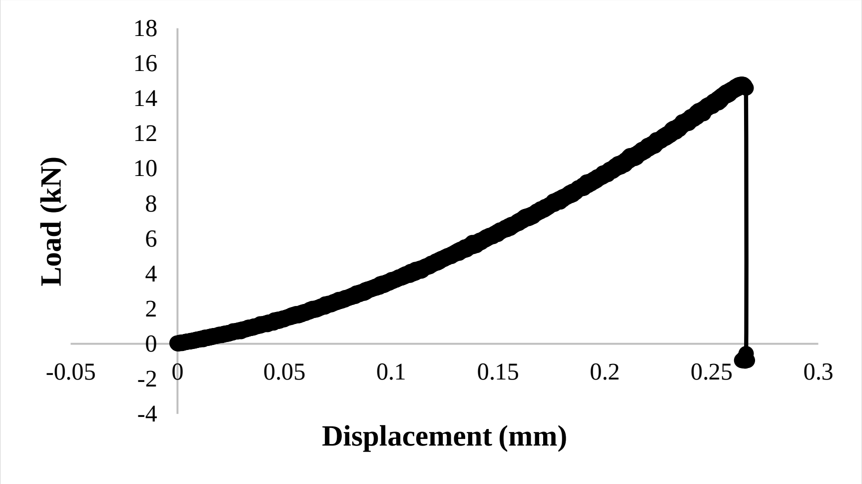

Figure D. 51. Load versus displacement curve of SNDB-50-085-1

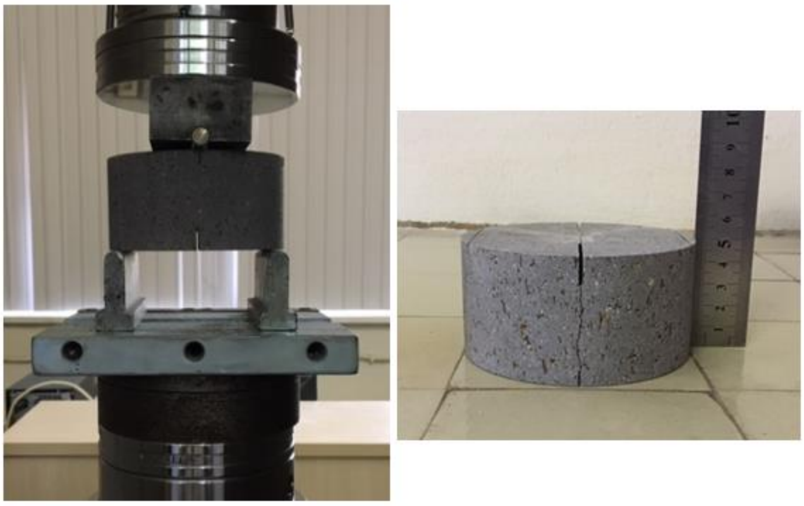

Figure D. 52. SNDB-50-090-2 specimen during and after test

Figure D. 53. 50 mm thick SNDB test specimens with 90 mm span length

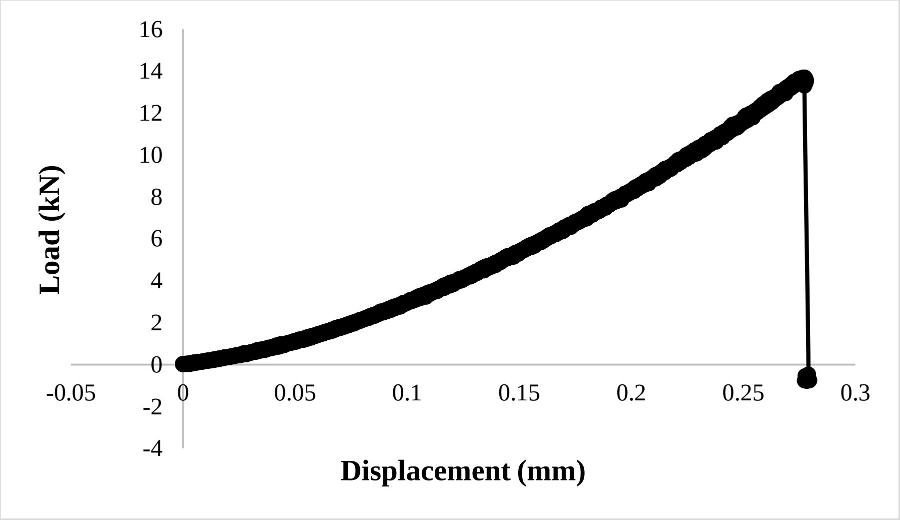

Figure D. 54. Load versus displacement curve of SNDB-50-090-2

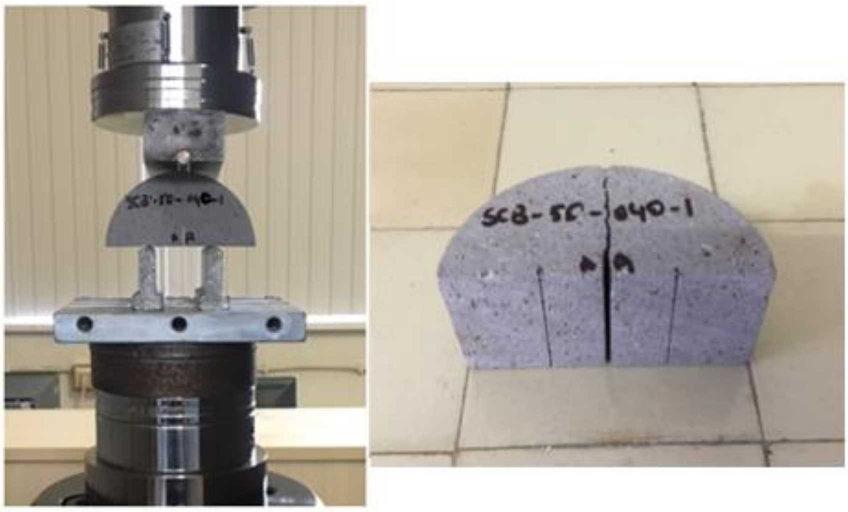

Figure D. 55. SCB-50-040-1 specimen during and after test

Figure D. 56. SCB test specimens with 40 mm span length

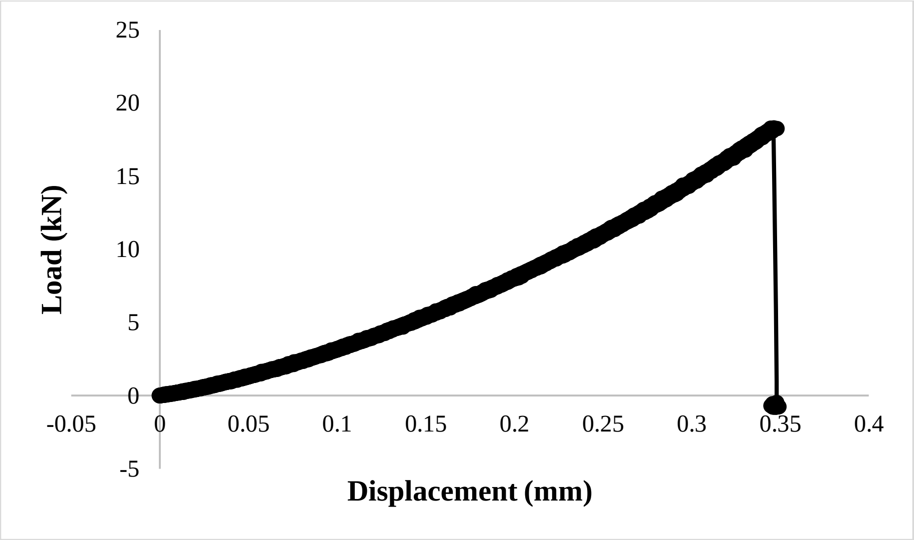

Figure D. 57. Load versus displacement curve of SCB-50-040-3

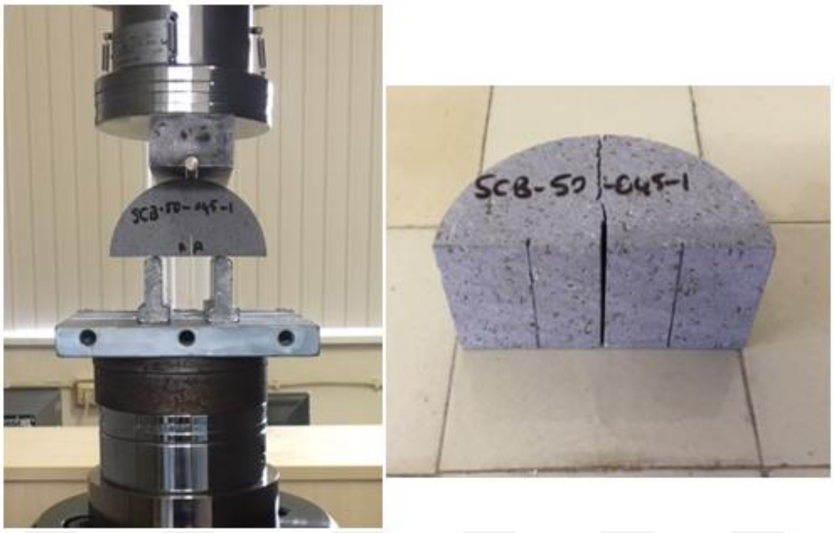

Figure D. 58. SCB-50-045-1 specimen during and after test

Figure D. 59. SCB test specimens with 45 mm span length

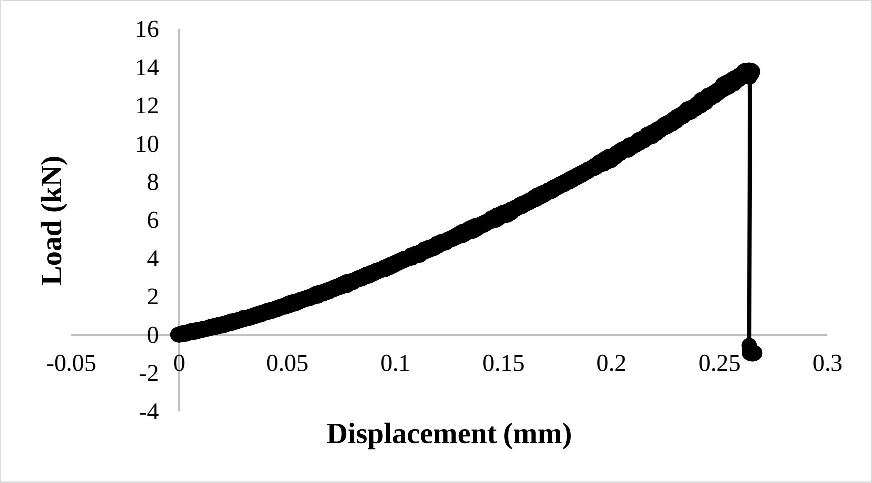

Figure D. 60. Load versus displacement curve of SCB-50-045-3

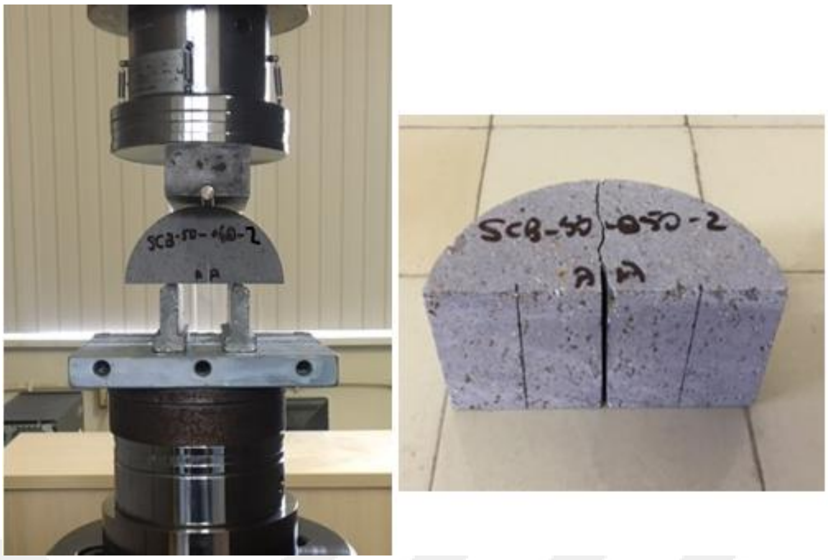

Figure D. 61. SCB-50-050-2 specimen during and after test

Figure D. 62. SCB test specimens with 50 mm span length

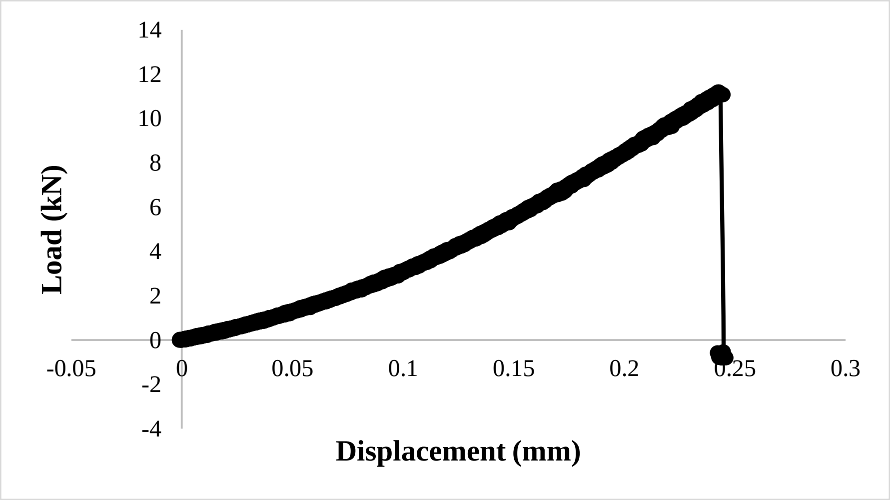

Figure D. 63. Load versus displacement curve of SCB-50-050-1

Figure D. 64. SCB-50-055-1 specimen during and after test

Figure D. 65. SCB test specimens with 55 mm span length

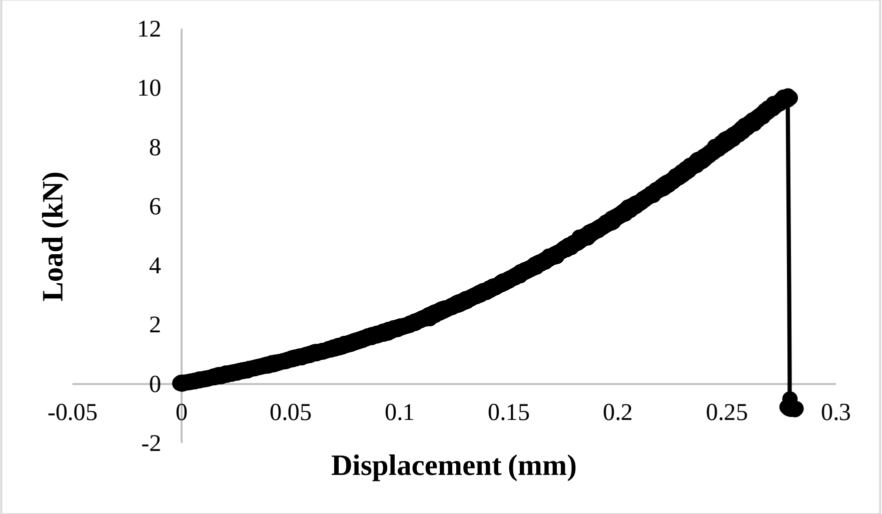

Figure D. 66. Load versus displacement curve of SCB-50-055-3

Figure D. 67. SCB-50-060-1 specimen during and after test

Figure D. 68. SCB test specimens with 60 mm span length

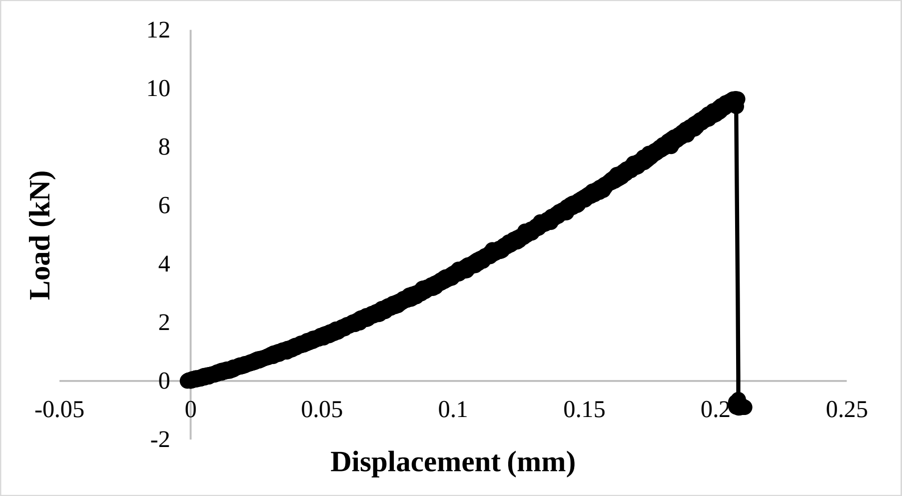

Figure D. 69. Load versus displacement curve of SCB-50-060-3

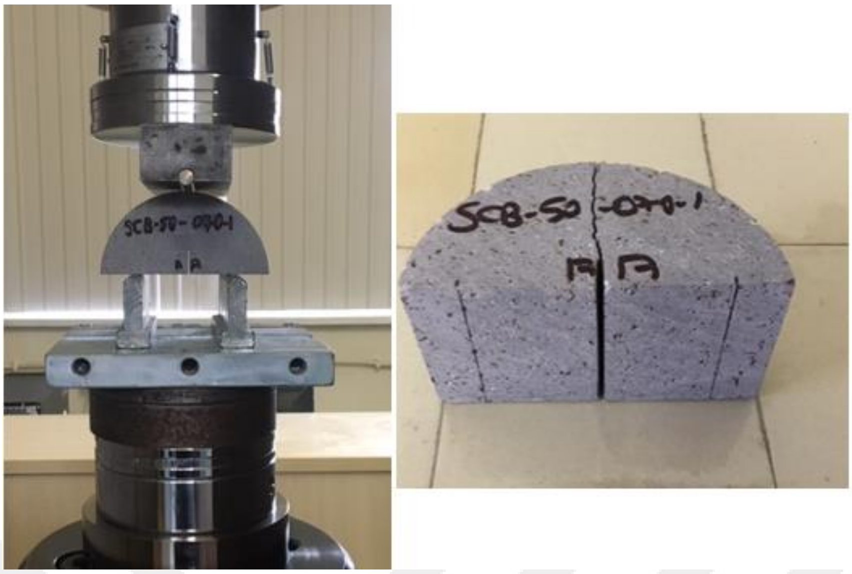

Figure D. 70. SCB-50-070-1 specimen during and after test

Figure D. 71. SCB test specimens with 70 mm span length

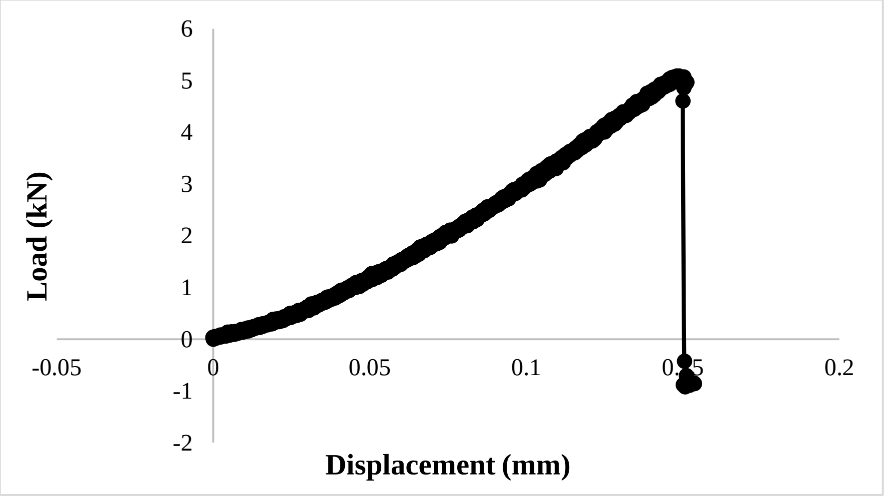

Figure D. 72. Load versus displacement curve of SCB-50-070-1

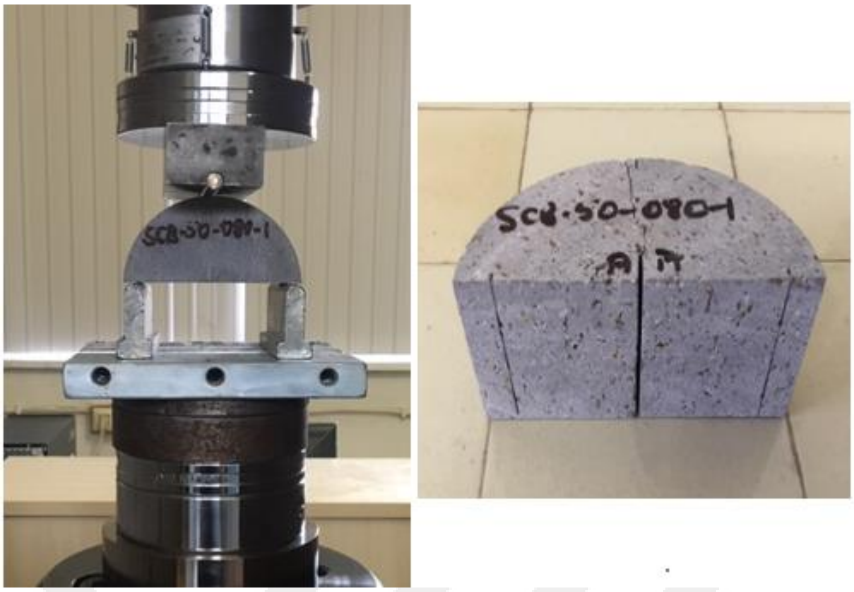

Figure D. 73. SCB-50-080-1 specimen during and after test

Figure D. 74. SCB test specimens with 80 mm span length

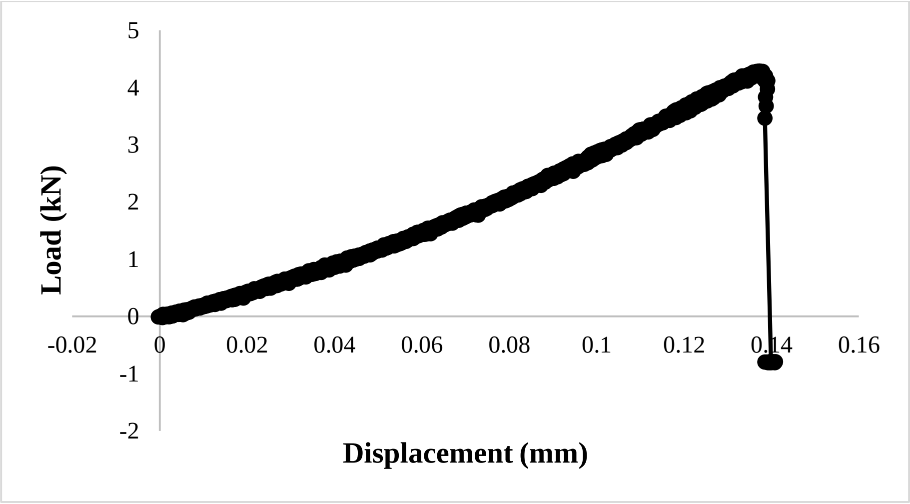

Figure D. 75. Load versus displacement curve of SCB-50-080-1

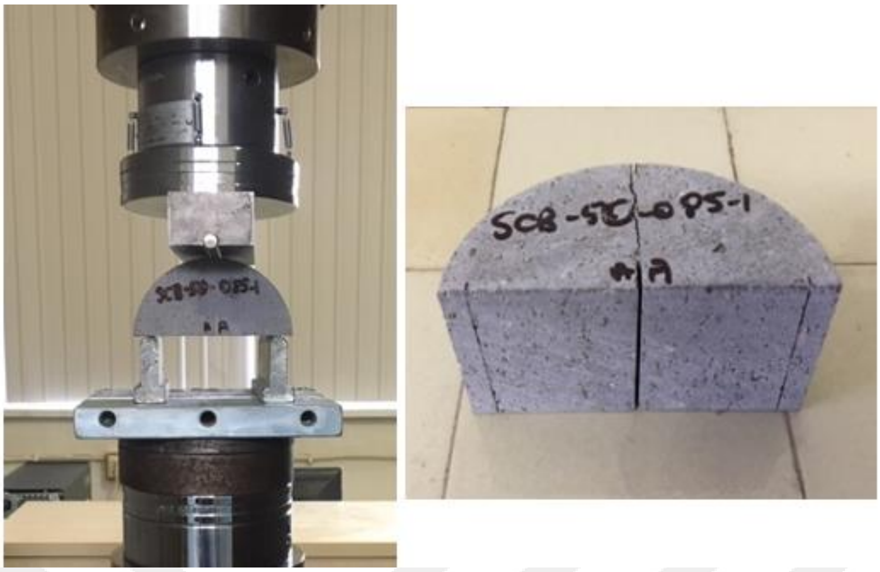

Figure D. 76. SCB-50-085-1 specimen during and after test

Figure D. 77. SCB test specimens with 85 mm span length

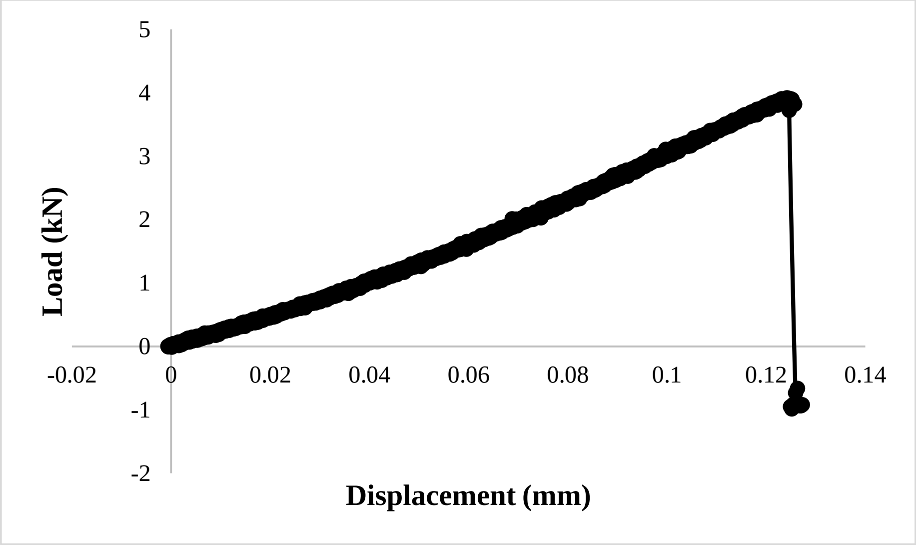

Figure D. 78. Load versus displacement curve of SCB-50-085-2

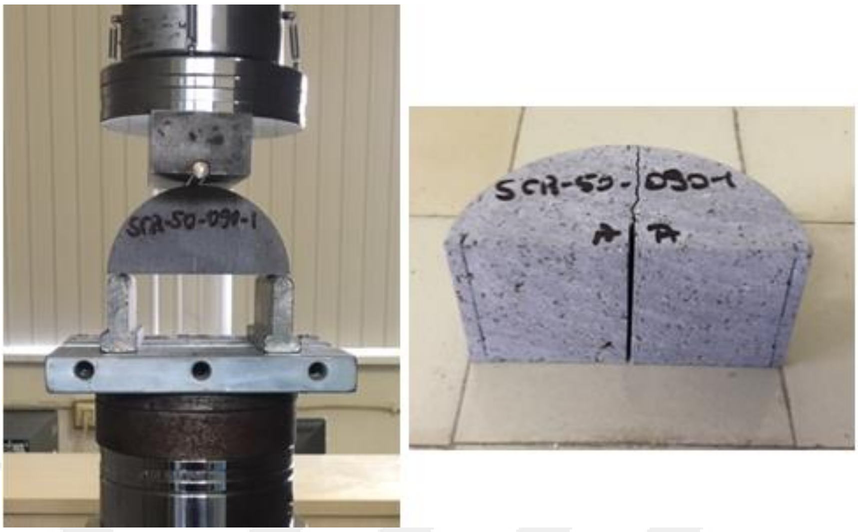

Figure D. 79. SCB-50-090-1 specimen during and after test

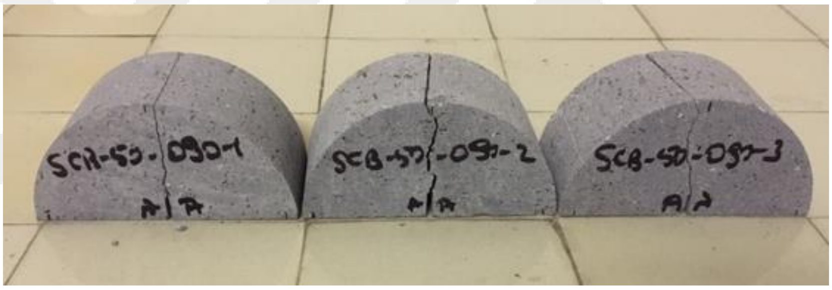

Figure D. 80. SCB test specimens with 90 mm span length

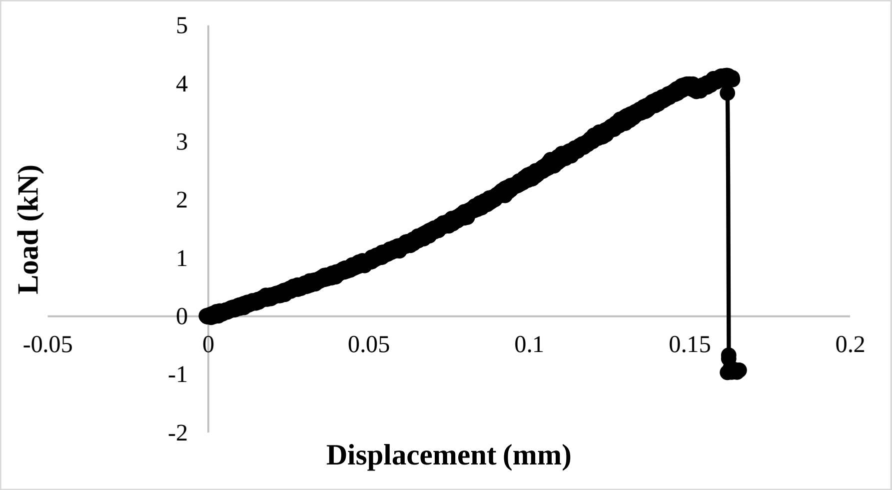

Figure D. 81. Load versus displacement curve of SCB-50-90-2